

Transilvania University of Brasov

INTERDISCIPLINARY DOCTORAL SCHOOL

Faculty of Electrical Engineering and Computer Science

**Eng. Cristian Leonard MUȘUROI**

# **Magneto-resistive Microsensors for Non-Contacting Current Measurement and Magnetic Nanoparticles Detection**

DOCTORAL THESIS SUMMARY

Scientific supervisor

**Prof.Dr. Eng. Elena HELEREA**

**BRAȘOV, 2024**

## Acknowledgements

Firstly, I would like to thank my Ph.D. adviser, Prof. Dr. Eng. Elena Helerea, for her patience and guidance throughout the research period, publishing endeavors and the writing of this thesis. The thorough approach to scientific work studies, coupled with extensive knowledge, wisdom and experience, provided steady progress for my scientific pursuits. I am appreciative of the support for attempting a complex interdisciplinary work requiring knowledge from multiple fields.

I would like to extend my appreciation to the members of my Ph.D. guidance committee Prof. Dr.Eng. Paul Borza, Dr.Phys. Marius Volmer, Dr.Eng. Marius Daniel Călin, Dr. Phys. Marioara Avram, and any other members of the Faculty of Electrical Engineering and Computer Science, from Transilvania University of Brasov, who helped refine the quality of this thesis by providing valuable feedback.

In particular I would like to thank Dr. Phys. Marius Volmer, for his invaluable scientific knowledge, material, logistical and moral support regarding the scientific field and subject of the thesis. This support was essential for the development of this thesis.

I would also like to express my gratitude towards senior researcher Dr. Marioara Avram from the National Institute for Research and Development in Microtechnologies (IMT-Bucharest) and her colleagues for any associated support during my Ph.D thesis and associated research projects.

Moreover, I would like to thank senior researcher Dr. Jenica Neamtu from ICPE-CA Bucharest and associated colleagues for assistance in depositing magnetic sensor structures.

Furthermore, I would like to thank my colleague Eng. Mihai Oproiu, for his efforts in assisting me with experimental setups, measurements, friendship and moral support.

Last but not least, I would like to thank all my coauthors from published papers during my Ph.D. My publishing efforts would not have gone so far without great team work and motivation.

Lastly, I would like to thank my family for their unceasing loving support and encouragements despite occasional setbacks in my research. As with all things, difficulties and setbacks sometimes happen, but their encouragement helped in overcoming every obstacle.

The Ph.D. research turned out to be a challenging but exciting process. I thoroughly enjoyed the associated challenges, knowledge developed and connections developed. I sincerely thank all collaborators for the opportunity of taking part in my scientific and career maturing process.

**Cristian Leonard Muşuroi**

# CONTENTS

<b>1. Introduction .....</b>	<b>6</b>
1.1. Necessity and Justification of the Thesis .....	6
1.2. Purpose and Objectives of the Research .....	6
1.3. Research Methodology and Bibliometric Analysis.....	7
1.4. Structure and Content of the Thesis.....	7
<b>2. Magnetoresistive Effects in the Microfabrication of Magnetic Sensors .....</b>	<b>10</b>
2.1. Magnetic Field Sensors — Applications and Active materials.....	10
2.1.1. Applications of Magnetic Field Sensors .....	10
2.2. Magnetoresistive Effects.....	11
2.2.1. Magnetoresistance as Material Parameter .....	11
2.2.2. Anisotropic Magnetoresistance (AMR) effect and Planar Hall effect (PHE).....	12
2.2.3. Giant Magnetoresistance (GMR) Effect .....	14
2.2.4. Tunnel Magnetoresistance (TMR) Effect.....	17
2.3. Characteristics and Performance of Magnetoresistive Sensors .....	18
2.3.2. Characteristic Parameters of Magnetoresistive Sensors.....	18
2.3.4. Applications of Magnetoresistive Sensors .....	19
2.3.5. Current Measurement with Magnetoresistive Sensors.....	20
2.4. Conclusions .....	21
<b>3. Micromagnetic Simulations of Magnetoresistive Sensors Behaviour .....</b>	<b>23</b>
3.1. Applying Micromagnetic Theory in Magnetoresistive Sensors Designs.....	23
3.1.2. Micromagnetic Simulations of AMR and PHE Sensors Behaviour.....	23
3.1.3. Micromagnetic Simulations of GMR Sensors Behaviour .....	26
3.2. Simulated Behaviour of Magnetoresistive Sensors Under the Influence of Magnetic Nanoparticles.....	27

3.2.2. Micromagnetic Simulation of the GMR Spin Valve Structure for Magnetic Nanoparticles Detection .....	27
3.3. Conclusions .....	29
<b>4. Macroscopic Analytical Methods and Electromagnetic Simulations for Different Conductor Types .....</b>	<b>30</b>
4.1. Magnetic Field Created by Current Flowing in Different Conductors .....	30
4.1.2. Case of Rectilinear Circular-Cross Section Conductor .....	30
4.2. Magnetic Field Created by Current Flowing through Rectilinear Single and Multiple Traces.....	31
4.2.1. Analytical Method .....	31
4.2.2. U-shaped Trace and Planar Coil Simulations and Experimental Validation .....	34
4.3. Conclusions .....	39
<b>5. Magnetic Nanoparticles Detection with Magnetoresistive Sensors.....</b>	<b>40</b>
5.1. Magnetic Method Applied for Magnetic Nanoparticles Detection .....	40
5.2. Experimental Studies for Magnetic Nanoparticles Detection with GMR sensors .....	40
5.2.1. Detection with Analysis of the Derivative of the Output Signal.....	40
5.3. Conclusions .....	44
<b>6. Development of Non-Contacting Current Measurement Devices based on Magnetoresistive Sensors.....</b>	<b>45</b>
6.1. Design, Construction and Characterization of an AMR Bridge Sensor .....	45
6.1.1. Design and Operation of the AMR Bridge Sensor .....	45
6.1.2. Fabrication of AMR bridge Sensor Demonstrator.....	46
6.1.3. Characterization of the AMR Bridge Sensor .....	47
6.2.4. Experimental Results for the Current Measurement Demonstrator Chip .....	49
6.2. Development of a Single Trace GMR Based Device for Non-Contacting DC/AC Current Measurement .....	50
6.2.1. Characterization of the GMR-based Current Sensor .....	50
6.2.2 Design, Construction and Characterization of the Single Trace GMR-based Device .....	51
6.3. Development of a Multi-Trace GMR Based Device for Non-Contacting DC/AC Current Measurement .....	54
6.3.1. Multi-Trace GMR Based Device Development and Mode of Operation .....	54
6.3.2. Experimental Results for Non-Contacting DC/AC Current Measurement.....	54
6.5. Conclusions .....	56

**7. Final Conclusions, Original Contributions, Valorisation of Research Results and New Research Directions ..... 59**

7.1. Final Conclusions ..... 59

7.2. Original Contributions ..... 63

7.3. Valorisation of Research Results ..... 65

7.4. New Research Directions ..... 69

**Bibliography (Selective) ..... 70**

# 1. Introduction

## 1.1. Necessity and Justification of the Thesis

With the current rate of accelerated scientific and technological development there is an ever-increasing demand for improving the performance of sensing technologies and developing new solutions for issues that were not present before. In this regard, developing magnetic sensor technologies is significant due to their wide range of applications and their unique capabilities.

Magnetic sensor technologies are crucial for progress in many industries, improving performance of sensing and control systems, enable non-destructive testing, implementing biomedical applications, IoT and wearable devices and for energy and environment monitoring.

Optimizing magnetic sensors in general and magnetoresistive sensors specifically is of paramount importance to improve their performance and enable them to be used effectively in a variety of applications. Optimization means improving important parameters such as sensitivity, resolution, linearity, stability and power consumption. These optimizations enable magnetoresistive sensors to provide more accurate and reliable measurements of magnetic fields, resulting in better overall system performance.

The intrinsic characteristics of magnetoresistive (MR) sensors (high scalability, sensitivity and integrability with semiconductor integrated circuits) make them a great choice for a wide range of applications, however, especially for high-sensitivity applications, specific design and implementation considerations must be considered, especially for detecting very low intensity magnetic fields.

Thus, the challenge consists in developing best practices for obtaining maximum sensor performance with high adaptability, minimum complexity, low cost, low power consumption. This goal can be achieved through optimization of the design and material choice, experimental setup, and minimizing magnetoresistive sensors disadvantages: such as hysteresis, non-linearity, offset, temperature drift, susceptibility to interference electromagnetic fields.

In terms of European research priorities, the research topic regarding the implementation and performance improvement of magnetoresistive sensors falls under the Horizon Europe 2021-2027 initiative under Pillar II, on the research direction – Cluster 4: Digital, Industry, Space. This direction supports new technologies and manufacturing innovation including advanced materials and quantum technologies [1].

In terms of national research priorities, according to the document regarding the National Research Plan for Research Development Innovation 2022-2027, the research topic falls on the research direction Program 5.7 "Partnerships for Innovation", through PNCDI IV [2].

Thus, the research subject of the thesis is aligned with current trends and deals with the overall development of magnetoresistive sensors from theoretical approach, design, simulation and experimental setup to improve sensor characteristics for specific applications.

## 1.2. Purpose and Objectives of the Research

The purpose of the research is the identification and development of the appropriate solutions for optimizing magnetoresistive sensors performance for two specific applications:

magnetic nanoparticles detection, and non-contacting current measurement. Thus, the aim of the thesis is to conceptualize and implement measurements methods for non-contacting low current measurement and for magnetic nanoparticles detection through utilizing sensors and devices based on magnetoresistive effects.

### **Specific objectives**

- 01.** Development of a knowledge base through documentation and comparative analysis of the magnetoresistive effects to be applied in the design and conceptualization of magnetic field sensor applications.
- 02.** Modeling, simulations and experimental validation for the processes that take place in magnetoresistive sensors and electrical current measurement structures.
- 03.** Development of methods and experimental setups for magnetic nanoparticles detection with magnetoresistive sensors.
- 04.** Development of non-contacting current measurement devices based on magnetoresistive sensors.

### **1.3. Research Methodology and Bibliometric Analysis**

The research followed the specific steps of scientific research methodology: Identifying the research issue; Defining the scope and clear focus of the research direction; Documentation and critical analysis; Establishing the solution and concretization through modeling, simulation, design; Practical realization and validation of the proposed solution; Establishing new research directions.

In order to establish the interest for the research subject and for the state-of-the-art analysis of magnetoresistive sensors, a bibliometric analysis was performed. The bibliometric analysis includes the search and retrieval of information and systemic analysis to establish the trends for the research subject and for establishing the state-of-the-art analysis on magnetoresistive sensors [3, 4, 5].

The result of the bibliometric analysis served as a starting point in identifying the research subject, defining the scope and issue of the research, in documentation and critical analysis of specialty literature. The establishment of the knowledge base allowed development of models, simulations and experimental setups regarding the behavior of magnetoresistive sensors. The next research phase consisted of designing, building and validation of experimental setups with magnetoresistive sensors. This research phasis will be continuous due to new challenges of proposed systems and magnetoresistive sensors technologies.

### **1.4. Structure and Content of the Thesis**

The doctoral thesis is structured in 7 chapters, contains a number of 144 figures, 19 tables, 250 references, 3 annexes, totalling 218 pages.

In this thesis, magnetoresistive sensor technologies based on anisotropic magnetoresistive effect (AMR), giant magnetoresistive effect (GMR), and tunneling magnetoresistive effect (TMR) effects are implemented. Two application domains are developed: detection of magnetic

nanoparticles, and non-contacting current measurement, especially low currents of the order of mA and  $\mu\text{A}$ .

Chapter 1, *Introduction*, deals with argumentation of necessity of approaching the magnetoresistive sensors subject and justifies the thematic of the research thesis. Magnetoresistive sensors and their application are priority subjects nowadays in the frame of continuous development and wide-scale implementation of Industry 4.0 and 5.0 technologies and the Internet of Things (IoT). The purpose of the thesis and research methodology is described.

In chapter 2, *Magnetoresistive Effects in the Microfabrication of Magnetic Sensors*, the knowledge regarding the magnetoresistive effects which serve as the basis for microfabrication of magnetoresistive sensors is systematized. The AMR effect is analysed in comparison with the Hall planar effect (PHE). The peculiarities of GMR effect and the TMR effect are highlighted. A critical analysis is carried out regarding the need to improve operation, the choice of materials and development of specific applications with magnetoresistive sensors.

In chapter 3, *Micromagnetic Simulations of Magnetoresistive Sensors Behaviour*, simulations are carried out using the micromagnetic theory methodology. Simulations are performed utilizing SimulMag, LLG Micromagnetics, and Object Oriented Micromagnetic Framework (OOMMF) software solutions to highlight the behavior of sensors based on AMR, PHE and GMR effects for magnetic field measurement. Single domain simulations are conducted for AMR and PHE sensors on permalloy structures. Multi-domain simulation is performed for PHE sensors to study the influence of geometry and magnetic anisotropy for cross, square and ring-shaped structures. Simulating the presence of maghemite magnetic nanoparticles on the surface of three PHE sensor structures (cross-shaped, disk-shaped and ring-shaped) is done to illustrate magnetic nanoparticles localization effects. Also, for a simulated GMR spin valve structure, the field characteristics are obtained. The simulated magnetization behaviour of the GMR spin valve structure is obtained under the presence and absence of magnetic nanoparticles on the surface of the sensor. The advantages of the micromagnetic approach method as well as the inaccuracies that may occur are discussed, highlighting that experimental research is necessary to validate the results.

In chapter 4, *Macroscopic Analytical Methods and Electromagnetic Simulations for Different Conductors Geometries*, the author applies analytical modeling to highlight the magnetic field created by the electric current passing through conductors with different geometries: rectilinear conductor, rectangular current loop, toroidal coil with circular and rectangular sections. These elements serve as a basis for the development of an analytical method for evaluation of the magnetic field created by a single and multiple rectilinear current traces, which make it possible to concentrate the magnetic field at the location of the magnetoresistive sensor. For a U-shaped trace and planar coil, COMSOL Multiphysics simulations and experimental measurements are performed, and results are validated with the proposed analytical method. Furthermore, the length, width and geometry shape influence on the magnetic field generated by the trace is performed in COMSOL. These results are useful for designing the current traces for low field and non-contacting current measurement applications.

In chapter 5, *Magnetic Nanoparticles Detection with Magnetoresistive Sensors*, the author systematizes the data on the properties and behavior of magnetic nanoparticles. The requirements of magnetic immunoassay complexes are discussed. The experimental study with the vibrating sample magnetometer (VSM) method on maghemite nanoparticles determined the magnetization

characteristics of maghemite nanoparticles at different temperatures as well as the blocking temperature and the procedure of characterizing polyethylene glycol functionalized magnetic nanoparticles. Experimental studies for MNPs detection have been performed with GMR sensors using different methods: analysis of the derivative of the output signal, DC detection, and AC magnetorelaxometry.

In chapter 6, *Development of Non-Contacting Current Measurement Devices based on Magnetoresistive Sensors*, the experimental setups conceived and realized by the author for contactless measuring of electric current with magnetoresistive sensors are described. Depending on the sensor manufacturing technology, experimental determinations are carried out with transducers based on AMR, GMR and TMR sensors. Four setups are developed for testing the measurement sensors and transducers. Firstly, a demonstrator setup based on AMR bridge sensors, designed by the author and microfabricated at ICPE-CA Bucharest, is described. The demonstrator includes two AMR bridge sensors that can be used independently or in differential configuration. The U-shaped current measurement trace, magnetic annealing and experimental setup were performed at the Electrical Engineering and Applied Physics Research Laboratory from Transilvania University of Brasov. The output characteristics obtained for different biasing magnetic fields in both DC and AC, and for different measurement configurations, are presented and analysed. Secondly, another setup with commercial GMR sensors in a double differential configuration with a single U-shaped current trace is implemented. The setup showed improved sensitivity compared to a single sensor measurement and demonstrates the importance of adjusting the biasing field during operation. The third setup, implemented with the same GMR commercial sensors as the second setup, includes a multi-trace current measurement device built as a planar coil to amplify the magnetic field in the sensor area. The setup showed significantly increased low magnetic field performance. For non-contacting measurement of currents through printed circuit boards, an adjustable current demonstrator probe with a commercial type TMR sensor developed by the author is described. The experimental setup is designed with 3-axis and rotation movement capabilities to allow precise positioning on the sample printed circuit board. The TMR sensor was evaluated for non-contacting DC and AC current measurements. The current probing TMR-based setup, although provides very good sensitivity, shows nonlinearity effects especially at low field values. The results are promising to serve as the basis for an automated non-contacting current probing application or for 2D/3D magnetic mapping applications.

Chapter 7, *Final Conclusions, Original contributions, Valorisation of research results and New Directions of Research*, summarize the results obtained by the author. The original contributions of the author are highlighted, and the methods of dissemination and use of the research results are presented.

## 2. Magnetoresistive Effects in the Microfabrication of Magnetic Sensors

### 2.1. Magnetic Field Sensors — Applications and Active materials

#### 2.1.1. Applications of Magnetic Field Sensors

Magnetic field sensors are required in an increasing variety of applications which demand improved performance: high sensitivity, low hysteresis, low noise and low thermal drift becoming crucial characteristics. Moreover, it is paramount that the specific characteristics of the sensors are tuned to specific applications. For example, applications such as wearable sensors for remote health monitoring, or lab-on-a-chip biosensors require development of new implementation technologies such as flexible substrates [6].

Multiple phenomena are used for magnetic field sensors: search-coil, micro(fluxgate) sensors [8], magnetoresistive (MR) and Hall effect sensors, which are based on galvanomagnetic effects in semiconductors and magnetic thin films [9]. The MR and Hall effect sensors are highly desirable for several applications due to their ease of interface and compatibility with integrated circuit (IC) technology, which combines digital and analogue electrical circuitry onto a single chip. Their specific and well-established application areas are closely linked to the performance of these sensors. Magnetic layer MR sensors are thought to be extremely sensitive and suitable for low magnetic fields between  $10^{-9}$  to  $10^{-2}$  T, whereas Hall sensors, made from semiconductors, are less sensitive and good for magnetic fields higher than  $10^6$  T [10]. As opposed to MR sensors, Hall sensors do not exhibit saturation at high magnetic fields. It should be mentioned that the arrangement of the microfabricated sensors and the magnetic characteristics of the materials used to deposit the stack structure have a significant impact on these limits for MR sensors.

The overall distribution of the magnetic field sensors in terms of the useful magnetic field is represented in Figure 2.1.

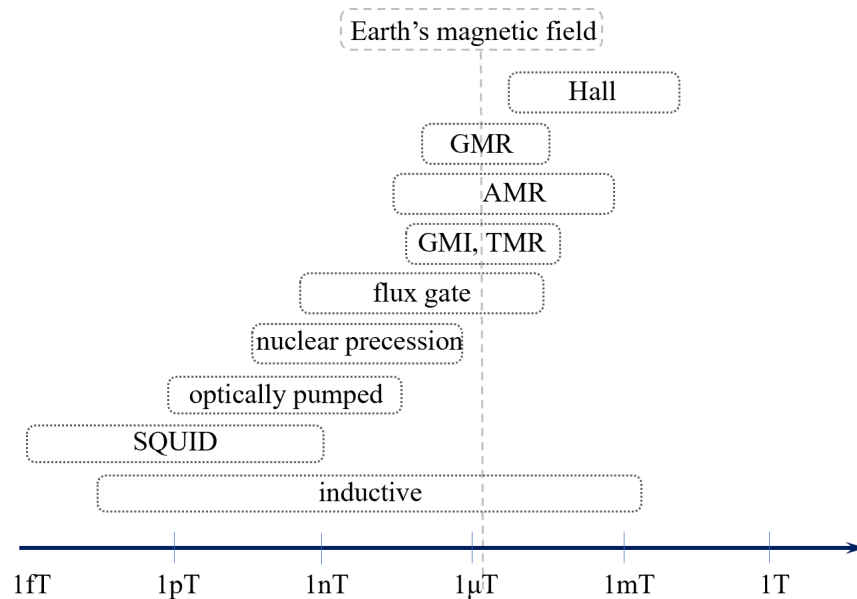


Figure 2.1. Distribution of magnetic field sensors in terms of useful magnetic field (original data from [25, 26]).

Magnetoresistive sensors are used to construct magnetic sensors for devices like high sensitivity magnetometers [12], rotation encoders, and micro compasses, as well as for basic research, i.e., study of magnetization processes and other related phenomena in nanostructured thin films [13], current sensors [18-20], magnetic nanoparticles detection for biosensing [21-24] in Lab-on-a-Chip (LOC) devices.

## 2.2. Magnetoresistive Effects

### 2.2.1. Magnetoresistance as Material Parameter

The magnetoresistive (MR) effect represents a change in the electrical resistivity of a material placed in a magnetic field [29, 30]. A homogeneous metal or semiconductor will generate a current under a variety of conditions if an electric field  $\mathbf{E}$  is applied. Ohm's law, which describes a microscopic linear relationship between the local current density  $\mathbf{J}$  and the electric field intensity  $\mathbf{E}$ , asserts this relationship:

$$\mathbf{J} = \sigma \mathbf{E} \quad (2.1)$$

where  $\sigma$  is the electrical conductivity.

For nonmagnetic materials, the MR effect can be expressed with [31]:

$$MR(H)\% = \frac{R(H) - R(H=0)}{R(H=0)} \times 100 \quad (\%) \quad (2.2)$$

where  $R(H)$  and  $R(H = 0)$  represent the resistance of the material for an applied magnetic field of intensity  $H$  and for  $H = 0$ .

For nonmagnetic metals, placed in magnetic fields up to 1 T, the amplitude of the MR effect is greater than zero but is less than 1%. In the case of semiconductors, the amplitude of the MR effect is greater but is significantly affected by the temperature dependency of resistivity. The MR effect, in this case, is due to the Lorentz force which curves the trajectories of conduction electrons and thus shortens their average travelled distance along the applied field.

Due to this effect, the MR effect is maximum when  $H$  is perpendicular on the plane of the probe, and thus on the current. Longitudinal effects can manifest only at high magnetic fields (usually greater than 5 T). For magnetic materials, the MR effect can be described with:

$$MR(H) = \frac{R(H) - R(H_{sat})}{R(H_{sat})} \quad (2.3)$$

where  $R(H)$  is the resistance in function of the applied field and  $R(H_{sat})$  is the resistance corresponding to the magnetic saturation state.

MR ratio has different values in function of the type of magnetoresistive effects and microfabrication technology. There are various types of MR sensors:

**Anisotropic magnetoresistance sensors** (AMR; MR ratio 2-4%) are sensors where the resistance depends on the angle between the magnetization and direction of current flow. AMR sensors use an open loop readout electronics with a dynamic range from DC to 1 GHz, and a sensitivity range of  $10^{-2}$  to 50 Gs or  $10^3$  to  $5 \times 10^6$  nT. With closed loop feedback, the minimum detectable field can be reduced to 0.1 nT for limited bandwidths. These sensors are light, compact, easy to fabricate and require between 0.1 and 0.5 mW of power.

**Giant magnetoresistance sensors** (GMR; MR ratio ~8-20 %). The GMR effect often manifests in multilayered magnetic structures of the FM/NM/FM type related by exchange interaction, wherein

NM refers to a nanometer-thick conductive nonmagnetic layer such as Cu, Cr, and FM designates magnetic layers such as  $\text{Ni}_{80}\text{Fe}_{20}$ , Co, CoFeB, etc. A TMR structure is obtained if the NM is a dielectric of the type  $\text{MgO}_2$  or  $\text{Al}_2\text{O}_3$ . GMR sensors can be employed in fields with a resolution between  $10\text{-}10^8$  nT. Compared to AMR sensors, they often have higher  $1/f$  noise.

**Magnetic tunnel junction sensors** (TMR; MR ratio  $\sim 200\%$  or higher). TMR sensors, in term of magnetic structure are very similar to GMR sensors, the difference constituting in the fact that the current flows through and insulating barrier and perpendicular to the film surface, while it flows horizontally to the film surface in a GMR element. Despite the numerous benefits of TMR sensors (average magnetoresistance of about 200%, low noise), they have a quadratic response with the injected current. These sensors can be used to construct non-volatile random-access memory (MRAM).

**Extraordinary magnetoresistance sensors** (EMR; MR ratio  $\sim 10^5\%$ ). Using semiconductors with a narrow bandgap and specific geometries has enables very large values of magnetoresistance at room temperature. A symmetric van der Pauw disk made of indium antimonide with embedded gold inhomogeneity is used in the sensor. Since the sensor does not contain any magnetic material, the current's field-dependent deflection around the inhomogeneity produces the magnetoresistance. Magnetic storage density could be increased to  $1\text{ Tbit/in}^2$  with the usage of extraordinary magnetoresistance read heads.

**Ballistic magnetoresistance sensors** (BMR; MR ratio,  $\times 100\text{-}1000\%$ ). Two ferromagnets must make a very small metallic contact for ballistic magnetoresistance to occur. Electrons can pass ballistically between the two ferromagnets if the contact is tiny enough and does not contain a domain wall. Nonadiabatic spin scattering across atomic-scale magnetic domain walls trapped at the constriction is responsible for the effect.

**Colossal magnetoresistance sensors.** Certain materials, primarily manganese-based perovskite oxides, have a feature called colossal magnetoresistance (CMR) that allows them to drastically alter their electrical resistance when exposed to a magnetic field. Although this phenomenon is not yet fully understood, these sensors exhibit very low anisotropy effects and are able to record only the magnitude of the magnetic field with high accuracy independently on the field orientation with respect to the sensor's plane. Other advantages include large (up to several hundred kHz) operation frequency range and the possibility to measure high-pulsed magnetic fields with pulse durations in the order of microseconds.

### 2.2.2. Anisotropic Magnetoresistance (AMR) effect and Planar Hall effect (PHE)

The anisotropic magnetoresistance effect was discovered by William Thompson (Lord Kelvin) in 1856 and appears in 3d ferromagnetic bulk materials or thin films from Ni, Co, Fe and their alloys [32, 33]. The AMR effect consists in a variation of material's electrical resistivity, depending on the angle  $\theta$  formed by the direction of the material's internal magnetization  $M$  and electric current  $I$  flow. The anisotropic s-d scattering of electrons caused by spin-orbit coupling on ferromagnetic materials' third-dimensional orbitals is the physical source of AMR. This effect causes the electrical resistivity many magnetic materials to be highest when the current is flowing parallel to the applied magnetic

field and least when it is flowing perpendicular to it. Thus, the amplitude of the AMR effect can be expressed by:

$$\frac{\Delta\rho}{\rho_{\perp}} = \left( \frac{\rho_{\parallel} - \rho_{\perp}}{\rho_{\perp}} \right) \times 100 \% \quad (2.4)$$

where resistivities  $\rho_{\parallel}$  and  $\rho_{\perp}$  are expressed at saturation field, when the current  $I$  is parallel and perpendicular to the magnetization,  $M$  direction respectively.

The AMR value ratio for ferromagnetic NiFe films is typically in the range of 2-2.2% for fields in the mT range, although for most magnetic materials, this ratio is rarely greater than 5%. Permalloy ( $\text{Ni}_{80}\text{Fe}_{20}$ ) having nearly zero magnetostriction constants in all directions, it is commonly used for this effect. For polycrystalline magnetic materials (including 3d type alloys), the dependence is expressed by [34]:

$$\rho_{xx} = \rho_{\perp} + (\rho_{\parallel} - \rho_{\perp}) \cos^2 \theta \quad (2.5)$$

$$\rho_{xy} = \frac{1}{2}(\rho_{\parallel} - \rho_{\perp}) \sin 2\theta \quad (2.6)$$

where  $\rho_{xx}$  is the parallel resistivity and  $\rho_{xy}$  is the perpendicular resistivity while  $\theta$  is the contained angle between the current density  $\mathbf{J}$  and magnetization  $\mathbf{M}$ .

The AMR effect may be visualized schematically by consider a thin film of ferromagnetic material (Figure 2.3).

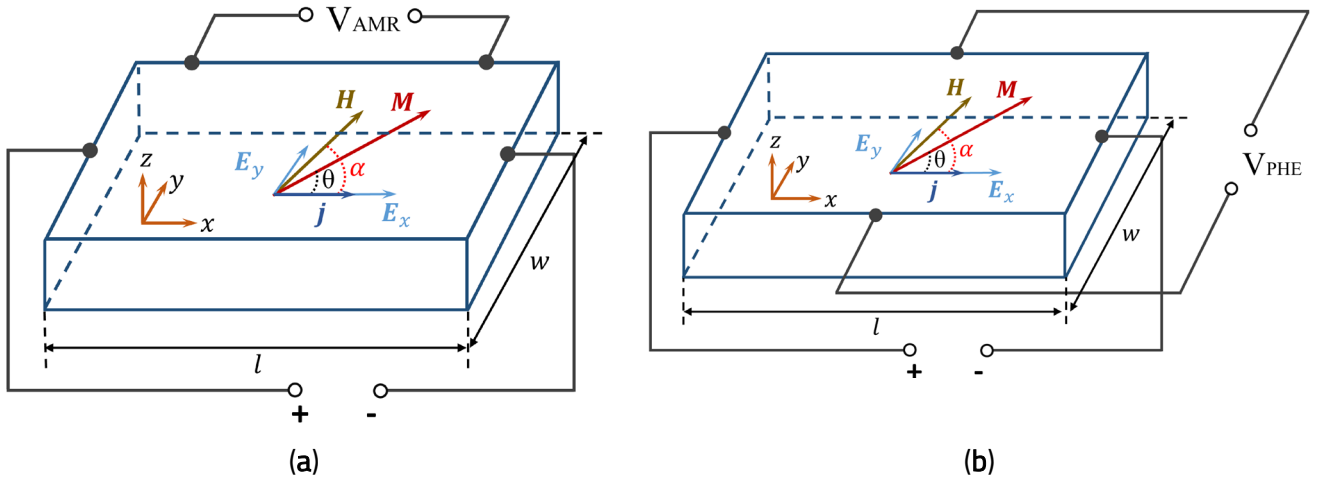


Figure 2.3. Schematic diagram showing the AMR (a) and PHE (b) effects on a Permalloy thin film with current flowing down the  $x$  axis. All vector components are in the film plane.

The difference in longitudinal resistivity describes the AMR effect, while the variation in transverse resistivity corresponds to the Planar Hall effect (PHE), Figure 2.3.

For real devices, the shape anisotropy ( $l > w$ ) and the uniaxial anisotropy field  $H_k$  defines the easy axis of magnetization. The angular dependence of the resistivity tensor components  $\rho_{xx}$  and  $\rho_{xy}$  can be used to determine the longitudinal  $E_x$  and the transverse  $E_y$  electric fields, when an electrical current flows through the film along  $x$  direction and the magnetization  $\mathbf{M}$  forms an angle  $\theta$  with the current direction [36]:

$$\begin{cases} E_x = J_x \cdot \rho_{xx} = J_x \rho_{\perp} + J_x (\rho_{\parallel} - \rho_{\perp}) \cos^2 \theta \\ E_y = J_x \rho_{xy} = J_x (\rho_{\parallel} - \rho_{\perp}) \sin \theta \cos \theta \end{cases} \quad (2.7)$$

with  $|j| = J_x$  and  $\rho_{\parallel}$ ,  $\rho_{\perp}$  as defined above and  $\rho_{xx}$ ,  $\rho_{xy}$  being the components of the electric resistivity tensor:

$$\mathbf{E} = \rho \mathbf{J}; \begin{bmatrix} E_x \\ E_y \end{bmatrix} = \begin{bmatrix} \rho_{xx} & \rho_{xy} \\ \rho_{yx} & \rho_{yy} \end{bmatrix} \cdot \begin{bmatrix} J_x \\ 0 \end{bmatrix} \quad (2.8)$$

The AMR effect is characterized by the fluctuation of the longitudinal resistance, which is given by  $\rho_{xx}$  and measured through:

$$V_{AMR} = E_x \cdot l \quad (2.9)$$

In a geometry common to the Hall effect, the second term,  $E_y$ , depicts the generation of a signal perpendicular to the current direction, but with the applied field contained in the film plane. This PHE signal, also designated as  $V_{PHE}$  is:

$$V_{PHE} = I \frac{(\rho_{\parallel} - \rho_{\perp})}{t} \sin \theta \cos \theta \quad (2.10)$$

where  $t$  is the thickness of the ferromagnetic (FM) layer, and  $I$  is the electric current applied along the  $x$ -axis of the FM layer.

In structures of AFM/FM type AFM (antiferromagnetic – IrMn, FeMn) or AFM/NM/FM an exchange interaction between the antiferromagnetic and the ferromagnetic layers can be established. The ferromagnetic layer is also responsible for orienting the magnetization from the adjacent ferromagnetic layer in the absence of an external magnetic field. This is called polarization through exchange interaction (exchange bias),  $H_{ex}$ .

In comparison with AMR, PHE sensors have specific advantages. Firstly, the largest slope, Figure 2.3, is achieved at  $\frac{\pi}{4} + \frac{n\pi}{2}$  while for PHE is  $\frac{n\pi}{2}$ . This allows the PHE sensor to be made using low-cost fabrication procedures with the angle  $\theta$  being equal to  $\frac{n\pi}{2}$  away from the applied magnetic field [35].

Also, given the relatively weak signal of the AMR sensor (a few percent) and considering it is usually measured over a DC element connected to a resistance, this causes aging and temperature drifts which affect this component that also influence the AMR sensor. To circumvent this issue, usually four AMR elements are connected in a Wheatstone bridge configuration to eliminate the need for the DC component. For PHE sensors, such arrangement is necessary since the DC component is no longer present at zero.

### 2.2.3. Giant Magnetoresistance (GMR) Effect

In 1988, the giant magnetoresistance (GMR) effect was discovered in a  $[\text{Fe}/\text{Cr}]_n$  magnetic multilayer. The GMR effect is an observed decrease in electrical resistance of ultrathin magnetic film multilayers when a large enough external magnetic field is applied. It was discovered that a considerable change in resistance is caused by a shift in the relative magnetic moment orientation between neighbouring magnetic layers.

The resistance  $R_p$  is at its lowest value when the layers are magnetized in parallel. At the greatest value of  $R_{AP}$ , the resistance occurs when the magnetizations of the adjacent magnetic layers are antiparallel to one another [20]. The spin-dependent scattering of spin-up (spin parallel to layer magnetization) and spin-down (spin antiparallel to layer magnetization) electrons at interfaces and in FM layers is the physical process underlying the GMR phenomenon. The 2007 Nobel Prize in Physics was given in recognition of the significance of this discovery [42].

The GMR effect can manifest in different structures: multilayer; pseudo spin valve, spin valve and granular thin film (Figure 2.5).

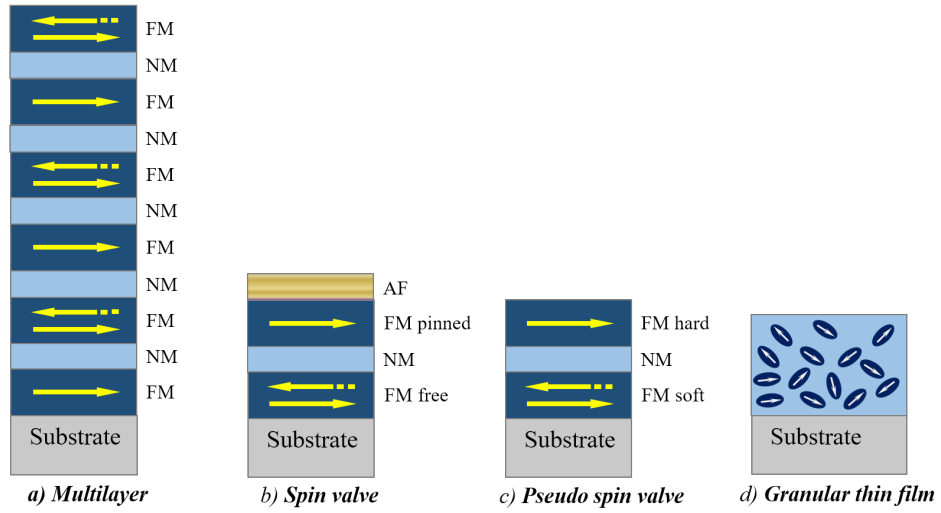


Figure 2.5. Different GMR structures: (a) multilayer, (b) pseudo spin valve, (c) spin valve, (d) granular thin film. Ferromagnetic layers (FM) are separated by nonmagnetic (NM) spacer layers. At zero field, ferromagnets are aligned antiparallel while at saturation field, the magnetic moments are aligned in parallel.

Each of these structures has different modes of operation and characteristics considering that there is a resistivity increase of the thin film as their thickness decreases to a few atomic layers. It can be denoted that the magnetic layers act like filters for spin with opposite orientation. Basically, the resulting resistance  $R$  can be written according to the angle  $\theta$  between the magnetizations ( $R_{AP}$  – antiparallel resistance;  $R_P$  – parallel resistance):

$$R = \frac{R_{AP} + R_P}{2} + \frac{R_P - R_{AP}}{2} \cdot \cos\theta \quad (2.12)$$

Thus, for antiparallel configuration:

$$\theta = 180^\circ \rightarrow \cos\theta = -1 \rightarrow R = R_{AP} = R_{High} \quad (2.13)$$

While, for parallel configuration:

$$\theta = 0^\circ \rightarrow \cos\theta = 1 \rightarrow R = R_P = R_{Low} \quad (2.14)$$

The GMR ratio is defined by:

$$GMR = \frac{R_{AP} - R_P}{R_{AP}} \cdot 100 \text{ [%]} \quad (2.15)$$

A high GMR ratio is preferred for sensors with high sensitivity. The GMR has a typical value of 4% to over 20%.

The GMR effect is based on the experimentally demonstrated fact that electron spin conservation extends over distances up to many tens of nanometers, longer than a typical multilayer's thickness. As a result, there are two ways that the electric current in the trilayer flows: one for matching electrons that have spin up and another for electrons that have spin projection down. The GMR sensor model may be reduced to two channel Mott resistor model since the spin channels are independent and can be thought of as two resistive elements connected in parallel (Figure 2.6).

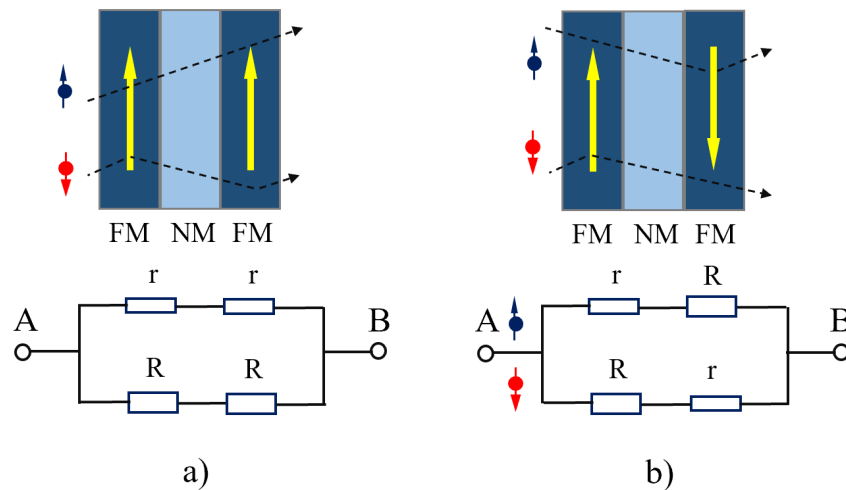


Figure 2.6. Resistor model of GMR with equivalent circuit model. The electron scattering in the trilayer system in case of (a) parallel, and (b) antiparallel magnetic configurations (reworked from [43]).

There are two configurations in which the GMR effect can occur: current-in-the-plane (CIP) and current-perpendicular-to-the-plane (CPP) (Figure 2.7). Given that the current flows in the plane of a thin, multilayered film, CIP devices are simpler to manufacture and CIP-GMR is simpler to identify. Controlling the orientation of the magnetic moments in the ferromagnetic layers and making the layers thin enough in relation to the electrons' mean free path are the biggest challenges [44].

However, because the CPP arrangement calls for measuring a film's resistance perpendicular to the layers, it is more difficult to implement. It is important to take careful considerations, such as ensuring that the resistance of the stack can be measured in relation to the resistance of the leads and other circuit components. Many techniques have been attempted to achieve successful CPP GMR measurements. These include decreasing the layers' cross section to the nanometer range, stacking a lot of layers in the sample, increasing the sample's overall thickness (though this may cause non-uniformities in the spacer layer), and even using superconducting leads to reduce resistance in relation to the GMR portion of the circuit [44].

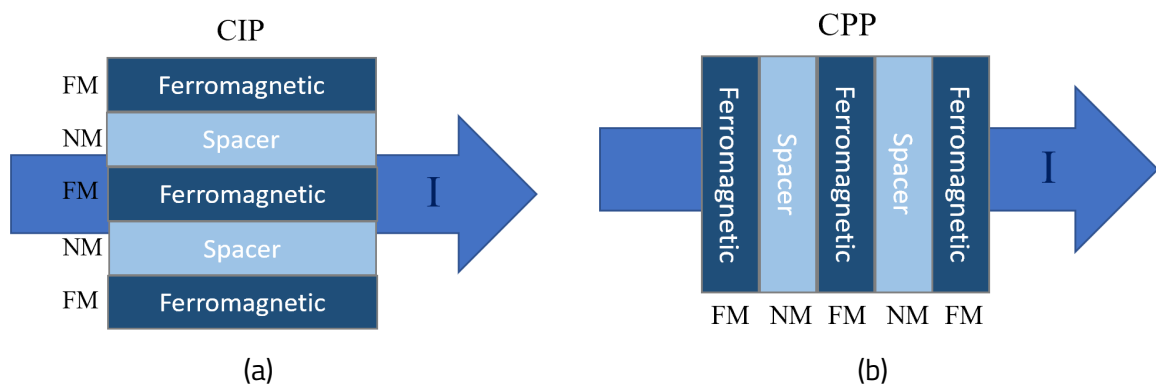


Figure 2.7. GMR Multilayer stacks configurations: (a) current-in-the-plane (CIP), (b) current-perpendicular-to-the-plane (CPP) (reworked from [44]).

## 2.2.4. Tunnel Magnetoresistance (TMR) Effect

Magnetic tunnel junctions (MTJ), also called tunnel magnetoresistance (TMR) structures, rely on the principle of spin-dependent tunnelling. If, for GMR the measuring current usually flows in plane, in TMR sensors the current tunnels through the nonconducting separation layer while flowing perpendicular to the layer plane [48]. The magnetic layers are separated by a conductive layer but by a very thin (usually 1-2 nm) insulating layer.

Considering the CIP and CPP structures (Figure 2.7), TMR occurs only in the current-perpendicular-to-plane geometry (Figure 2.9) and the magnitude of the current is lower than that of metallic spin valves, however, the magnitude of this effect is much more pronounced, with MR ratio on the order of hundreds of percent.

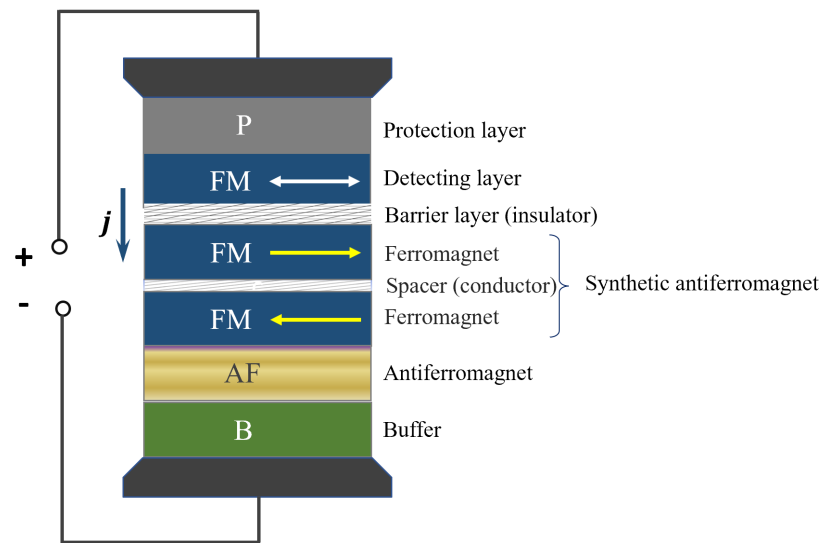


Figure 2.9. Schematic of a TMR spinvalve structure.  $P$  denotes the protection layer (capping layer),  $B$  is the buffer layer (usually Si),  $FM$  stands for ferromagnet,  $AF$  for antiferromagnet and the synthetic antiferromagnet is formed by a traditional spinvalve FM/spacer/FM structure, while  $\mathbf{j}$  is the density of current through the junction.

The TMR effect results from the ability of a quantum particle to traverse the potential barrier at an atomic scale, which is impossible to be described with classical physics: the wave function associated to a particle does not cancel in the barrier zone, but it is attenuated in an exponential way in this zone. If the wave function does not become mathematically zero at the exit from the barrier, there is a probability that the particle will cross the potential barrier. Utilizing this principle, Gamow [49] was able to justify nuclear disintegration with  $\alpha$  particle emissions. Also, based on this principle, devices such as tunnel diodes, metal-oxide-metal junctions (MOM, superconductive Josephson junctions and recently, tunnel junctions with magnetic components) have been developed.

Conduction electrons in ferromagnetic metals exhibit spin polarization, and the spin is preserved throughout the tunneling process, according to tunneling experiments. Jullière (1975) presented the first model used for spin-dependent tunneling [50]. The polarization,  $P$ , of electrons "tunneling from ferromagnetic metals" is used in this concept to explain the spin-dependent tunneling conductance:

$$P = \frac{n^\uparrow - n^\downarrow}{n^\uparrow + n^\downarrow} \quad (2.29)$$

Consequently,

$$\frac{n^\uparrow}{n^\downarrow} = \frac{1+P}{1-P} \quad (2.30)$$

$$G = G^\uparrow + G^\downarrow \quad (2.31)$$

where  $G$  is the conductance of the tunnel barrier and  $n^\uparrow$  and  $n^\downarrow$  denote the spin-polarized electron "density of states". The relations for the TMR effect based on the Jullière model are:

$$TMR = \frac{G_P - G_{AP}}{G_P} = \frac{\Delta R}{R} = \frac{R_{AP} - R_P}{R_{AP}} = \frac{2P_1 P_2}{1 + P_1 P_2} \quad (2.32)$$

where  $G_P$  and  $G_{AP}$  are the parallel and antiparallel conductances,  $P_1$  and  $P_2$  are the spin polarizations of two ferromagnetic layers,  $R_{AP}$  is the magnetization between the two layers when they are orientated antiparallel, while  $R_P$  is the same for parallel orientation.

For more precise spin-dependent tunnelling approximations, the layer-wise free-electron model are tight-binding model are more suitable for calculating the tunnelling magnetoresistance for a precise electronic structure. Specifically, the energy bands at the Fermi surface of several metals (Na, K, Cu, Ag, Au) and some semiconductors can be reasonably represented by the free electron model. With rare exceptions, the electrical structure of transition metals cannot be adequately described by the free electron model.

In summary, the phenomenon of spin-dependent electron transport is essential for describing the behaviour of GMR and TMR devices.

## 2.3. Characteristics and Performance of Magnetoresistive Sensors

### 2.3.2. Characteristic Parameters of Magnetoresistive Sensors

The best approach in selecting a specific sensor is to define the general and specific requirements for a particular application. In this regard, careful considerations must be taken into account regarding the specific parameters for the sensor (e.g. sensitivity, accuracy, error, dynamic characteristics) as well as the environmental operating conditions (temperature, electromagnetic interference fields, chemical, mechanical stress etc.).

The most important general magnetoresistive sensor characteristics are: span (Full-scale) input, full-scale output, accuracy, calibration error, hysteresis, nonlinearity, saturation, repeatability, resolution, output impedance, dynamic characteristics (electrical, thermal), reliability. These parameters classification is based on the one performed in [57].

Other important characteristics of magnetic sensors are: magnetic field resolution, signal-to-noise ratio: accuracy (absolute) and precision (relative), linearity of magnetic response, power consumption, size, weight, cost and availability, application environment (humidity, chemical, mechanical stress), electrical input and output impedance, stability, reliability, lifetime.

The limitations of magnetoresistive sensors are related, reproducibility, voltage offset, temperature drifts and bandwidth restrictions.

Figure 2.12 shows the range of applications for magnetic field sensors in terms of the useful magnetic field. GMR/TMR can be used from the pT to close to kT range while AMR can be used from nT to mT range.

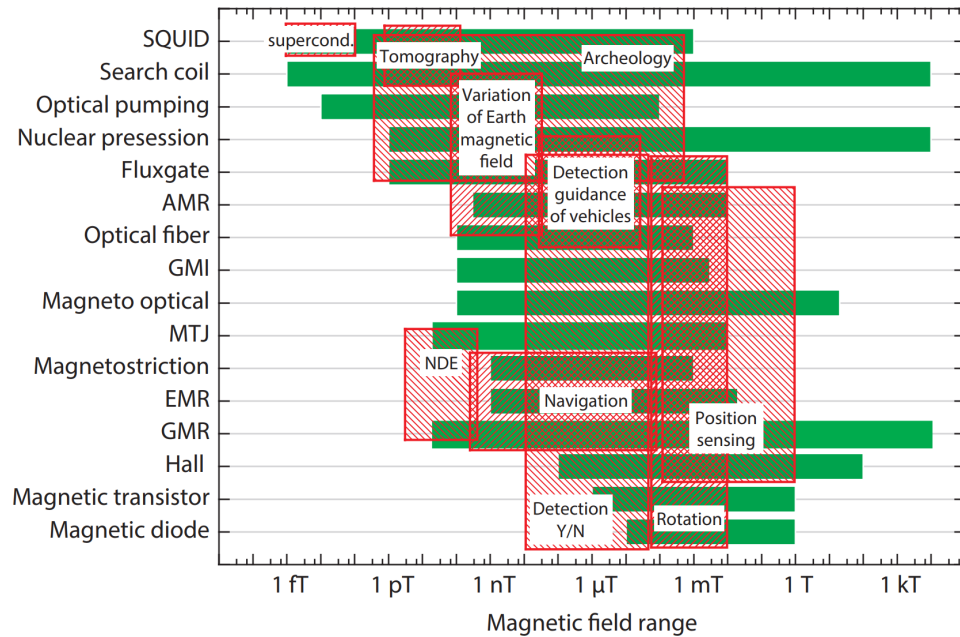


Figure 2.12. Range of applications of magnetic field sensors (reproduced after [57], original data from [77]).

### 2.3.4. Applications of Magnetoresistive Sensors

Magnetoresistive sensors can detect magnetic fields usually ranging from  $10^{-9}$  to  $10^{-1}$  T with a linear scale up to  $\sim 10^{-2}$  T. Magnetoresistive sensors built from thin magnetic layers have much higher sensitivities compared with semiconductor-based Hall Sensors. On the other hand, the limitations of MR sensors are related to the nonlinear magnetic characteristics of the utilized materials, the structure of the multilayered system and layout of the sensor.

Table 2.6 shows a summary of the application domains for AMR, GMR, TMR sensors, as well as the suitability of the MR sensor for that application domain.

Table 2.6. Suitability of application domain with magnetoresistive sensor technology.

Application domain	Sensor Technology		
	AMR	GMR	TMR
Current sensors	✓	✓	✓
Low field magnetometer	✓	✓✓✓	✓✓
Positioning (linear/angular)	✓	✓	✓
Tactile sensors	✓✓	✓✓✓	✓
Strain sensors	✓✓	✓	✓✓
Magnetic compass	✓✓	✓	✓
Nuclear magnetic resonance (NMR)/MRI	✓	✓✓	✓✓
Non-destructing testing	✓	✓	✓

Flexible magnetic sensors	✓✓	✓	✓✓
Microfluidics	✓	✓	✓
MRAM	✗	✓	✓✓
Hard disk read heads	✗	✓	✓✓
Neuron culture	✗	✓	✓
Brain/Cardiac mapping	✗	✓	✓✓
Scanning microscope	✗	✓	✓✓
Biosensors	✓	✓✓✓	✓✓

<sup>1</sup> The number of checks for an application marks the theoretical suitability of the sensor technology for that application domain.

### 2.3.5. Current Measurement with Magnetoresistive Sensors

Electrical systems require accurate current measurement, and various current sensing techniques have been created and modified to meet varying requirements. These applications require precise DC/AC measurements in order to control devices such as electric motors, electrical contacts and to measure the quantity and quality of electrical energy. There is a continuous interest in enhanced performance and function for current sensing methods, especially with the onset of Industry 4.0 and 5.0 technologies in an Internet of things era. A general classification of current measurement methods is shown in Figure 2.14.

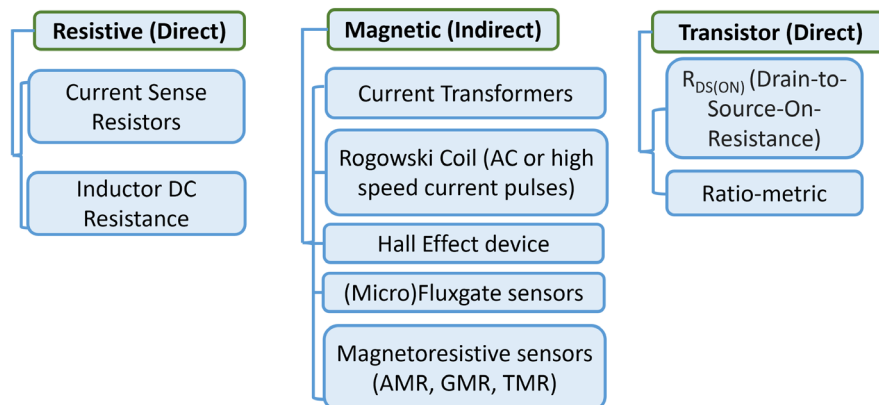


Figure 2.14. Schematic diagram of the classification of current measurement methods.

There are three general methods of measuring electric current: resistive, magnetic and transistor based. Resistive and transistor-based methods measure electric current directly while magnetic methods can be applied for non-contacting current measurement.

While beneficial in certain situations, resistive-based current-sensing methods have several shortcomings, including poor precision, power loss, low bandwidth, lack of galvanic isolation, and noise. Conversely, most of these disadvantages are countered by non-contacting (electromagnetic based) current sensing systems, although they do have certain unique challenges in terms of operation and implementation.

Non-contacting measurement systems, which include current transformers, Rogowski type coils, (micro)fluxgate sensors, Hall sensors, MR sensors also have certain advantages such as galvanic isolation, thermal stability and increased resistance to interference magnetic fields.

Typical non-contacting current sensor technologies are AC/DC current transformers [143, 144, 145], fluxgate magnetometers [146], Hall effect sensors [149], anisotropic magnetoresistive (AMR) [150], PHE sensors [151], giant magnetoresistive (GMR) [10, 143, 152, 153] and tunnelling magneto-resistance (TMR) sensors [154, 155].

The most popular instruments for measuring just the AC current component are Rogowski coils and current transformers, however, sensors that can accurately detect DC magnetic fields must be utilized to measure DC/AC currents.

Current sensors based on magnetoresistive effects offer high accuracy, endurance, low temperature drift, low offset, and are suitable for low volume production together with tight integration capabilities with integrated circuits (ICs). Based on the properties of AMR, PHE GMR and TMR sensors, many applications have been developed for current measurement.

## **2.4. Conclusions**

1. The theoretical basis for research and development of magnetoresistive sensors was established for a general positioning and applications of magnetoresistive sensors compared with other magnetic sensor technologies.
2. Focus was placed on the physical explanation of the magnetoresistive effects: anisotropic magnetoresistance (AMR), planar Hall effect (PHE) – which is a consequence of AMR, giant magnetoresistance (GMR) and tunneling magnetoresistance (TMR or MTJ) sensors.
3. The AMR effect is the dependency of a material's electrical resistivity, or resistance, on the angle formed by the direction of the material's internal magnetization and electric current flow.
4. Accurate description of GMR and TMR effects requires the combined theoretical methods combining first-principles quantum mechanical treatment and semi-classical Boltzmann transport theory.
5. In designing of magnetoresistive sensors, all general parameters should be considered. The specific characteristic parameters for magnetoresistive sensors should also be taken in account.
6. Determining the general and specific characteristics for MR sensors may not be sufficient for evaluating sensor performance especially when introducing other disturbing elements within the sensor system (such as magnetic nanoparticles) and increasing the complexity of the sensor setup by introducing an array of sensors, other electronics, or introduce environment-sensitive components, such as bio-analytes, for biosensing applications for both in vitro or in vivo use.
7. There are specific advantages for different types of magnetoresistive sensors:
  - The typical magnetoresistance ratio increases in the following order for these sensors: AMR (2-4%), GMR (8-20%), TMR (greater than 100-200% or even thousands of percent).
  - AMR sensors are simple and cost effective, with good low field performance but limited at high fields, low thermal drift (for PHE sensors in bridge configuration) compared with GMR and TMR sensors.
  - GMR performance depends largely on the configuration of the sensor: CPP GMR tends to be higher than CIP GMR in most cases, while granular GMR can be compared with CPP in terms of behaviour.

- The field behaviour of the GMR effect is quadratic, very similar with the AMR effect but the amplitude of the GMR effect is larger, up to 15-20 % at room temperature.
  - TMR sensors have higher sensitivity and lower power consumption compared with GMR sensors, but they also have higher noise levels, which limits their usefulness for low field applications. Also, because of more complex manufacturing, TMR sensors are the most expensive compared with GMR and AMR.
8. The comparative analysis of the applications and performance of MR sensors demonstrates the wide application range for MR sensors: contactless current sensors, precision magnetometers, position sensors (velocity, compass etc.), non-destructive testing sensors, temperature sensors, mechanical stress sensors, smart sensors, flexible sensors, biosensors etc. Some MR effects can be more suitable for an application.
9. Magnetoresistive sensors offer high accuracy, endurance, low temperature drift, low offset, tight IC integration, which makes them suitable for non-contacting current measurement.

The main challenges identified by the limitations of MR sensors in terms of applications implementation are related to the resolution, accuracy, and repeatability error of the sensor. For biosensing applications, this holds true especially in the low field part of the Full-Scale. Thus, it is necessary to establish new methods for modeling, design and fabrication for magnetoresistive sensors, which will have purpose-built characteristics and performance for each application domain.

### 3. Micromagnetic Simulations of Magnetoresistive Sensors Behaviour

#### 3.1. Applying Micromagnetic Theory in Magnetoresistive Sensors Designs

##### 3.1.2. Micromagnetic Simulations of AMR and PHE Sensors Behaviour

To illustrate the behaviour of AMR and PHE sensors, a study with micromagnetic simulations was performed. Part of this study was published in the authored work [172].

The two primary uses of PHE sensors are field detection and rotation encoder. It should be noted that magnetization rotation can be caused by a rotating magnetic field or by a magnetic field,  $H$ , applied along the  $y$  axis. Based on these assumptions several simulation studies are proposed, going from a single magnetic domain simulation method to a multi-domain one. Moreover, the effects of the geometry of the structure are highlighted through simulations.

##### a. Multi-domain modelling of AMR and PHE effects

In real structures, AMR and PHE effects can be affected by hysteresis since permalloy layers are not single domain even with the hypothesis of a high uniaxial anisotropy. Figure 3.4 presents the results of micromagnetic simulations using LLG Micromagnetics simulator [163]. The parameters used for the simulation are: a Permalloy strip  $800 \times 400 \times 10 \text{ nm}^3$  with a cell dimensions  $5 \times 5 \times 5 \text{ nm}^3$ ,  $M_S = 710 \text{ kA/m}$ , exchange constant  $A = 1.3 \times 10^{-11} \text{ J/m}$ , the anisotropy constant  $K_u = 500 \text{ J/m}^3$  along  $x$  axis at a temperature  $T = 0 \text{ K}$ .

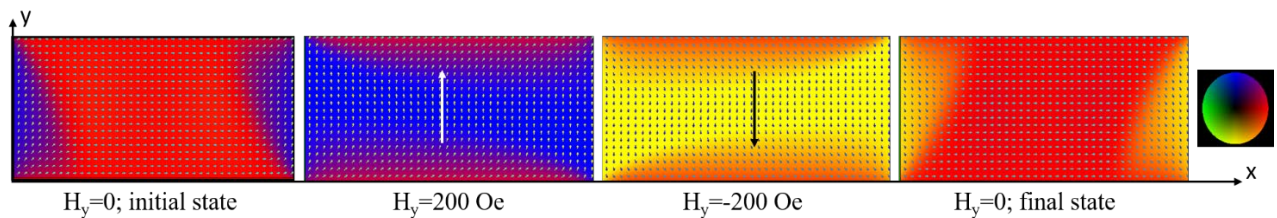


Figure 3.4. Multi-domain representation of magnetic moments orientation in a thin film of Permalloy  $800 \times 400 \times 10 \text{ nm}^3$ . The colour legend illustrates the magnetic moments orientation.

The internal magnetization has no preferred direction along the longitudinal axis and a flipping of  $180^\circ$  can occur due to spikes or exposure to some external magnetic fields. This flipping of the magnetization results in different sensitivity of the system. To overcome this problem an internal coil or external controlled magnetic field should be used to reset and set the magnetization to the initial orientation. Other methods to keep the initial magnetization state, for  $H = 0$ , is to use exchange-biased structures like bilayers FM/AF, trilayer FM/NM/AF or spin valves of the type FM/NM/FM/AF where FM is ferromagnetic layer like NiFe, NiFeCo, etc., NM is a nonmagnetic layer like Cu, Ag, Pt, and AF is an antiferromagnetic layer like FeMn or IrMn [39].

Figure 3.5 shows the simulated dependencies of the PHE signal for three permalloy exchange biased structures. The simulations were performed under the same conditions as in Figure 3.4.

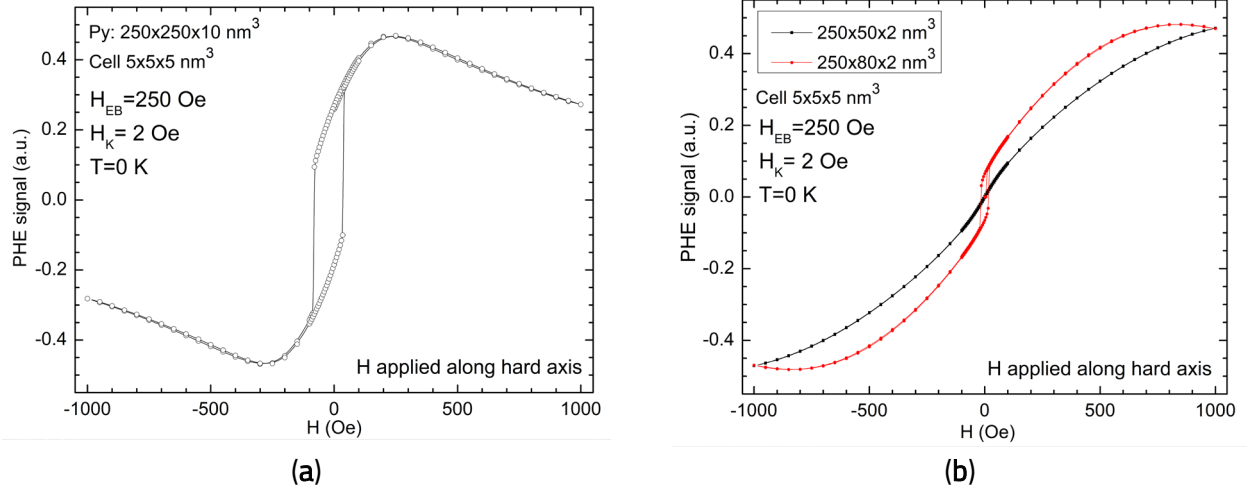


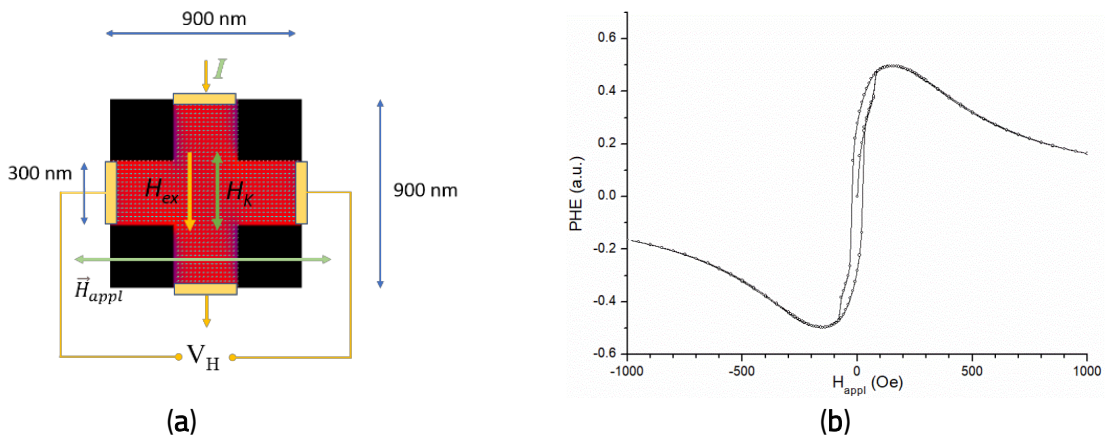
Figure 3.5. Multi-domain micromagnetic simulation of a PHE signal for three Permalloy structures: (a)  $250 \times 250 \times 10 \text{ nm}^3$ , (b)  $250 \times 80 \times 10 \text{ nm}^3$  and  $250 \times 50 \times 10 \text{ nm}^3$ .

The simulation shows the significance of the shape anisotropy for reducing magnetic hysteresis effects.

### b. Influence of the geometry of the structure

To illustrate the effects of the sensor geometry on the PHE signal, micromagnetic simulation analysis were performed with LLG Micromagnetics simulator v4 between cross-shaped (Figure 3.6), square-shaped (Figure 3.7 and Figure 3.8) and ring with inner disk (Figure 3.9) permalloy structures under the following parameters:  $M_S = 710 \text{ kA/m}$ , exchange constant  $A = 1.3 \times 10^{-11} \text{ J/m}$ , and the anisotropy constant  $K_u = 500 \text{ J/m}^3$  along  $x$  axis at a temperature  $T = 0 \text{ K}$ ,  $H_{EB} = 150 \text{ Oe}$  with a  $10 \times 10 \times 10 \text{ nm}^3$  discretization cell. Between  $K_u$  and  $H_k$  the following statement is true:  $H_k = 2K_u/M_S$ . In all simulations, the magnetic layer has a thickness of  $10 \text{ nm}$ .

The geometric dimensions of each permalloy structure are: for cross-shaped  $900 \times 900 \times 10 \text{ nm}^3$  ( $300 \text{ nm}$  arm, Figure 3.6a),  $500 \times 500 \times 10 \text{ nm}^3$  for square-shaped. Some of the simulation results for the different geometries of the PHE structures are summarized in Figure 3.6 (cross-shaped), Figure 3.8 (square shaped) and Figure 3.9 (ring with inner disk).



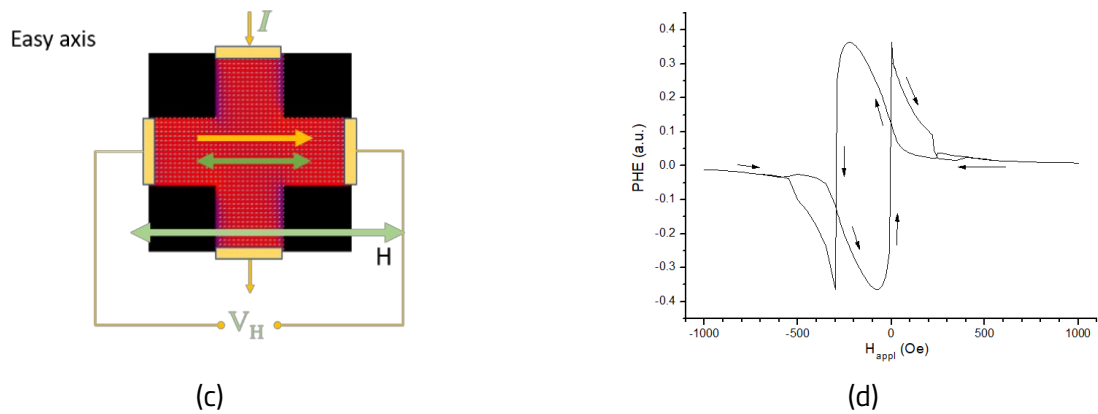


Figure 3.6. Multidomain micromagnetic simulation of a cross-shaped permalloy structures where  $H$  is applied over easy and hard axis: (a) geometry and hard axis representation, (b) PHE signal over hard axis, (c) easy axis representation, (d) PHE signal over easy axis.

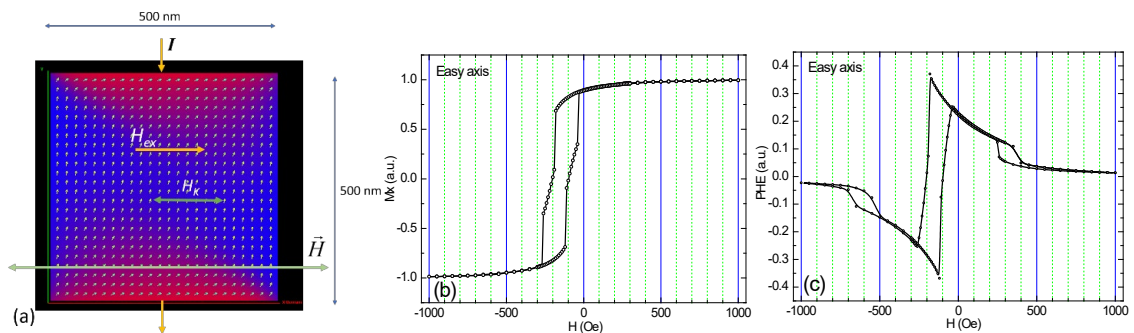


Figure 3.8. Multidomain micromagnetic simulation of a square-shaped permalloy structure where  $H$  is applied over the easy axis: (a) Simulated structure, (b) magnetization curve, (c) calculated PHE signal.

In Figure 3.8 it can remark the abrupt magnetization commutation process which is a consequence to the movement of domain walls, more than an irreversible rotation of magnetic moments.

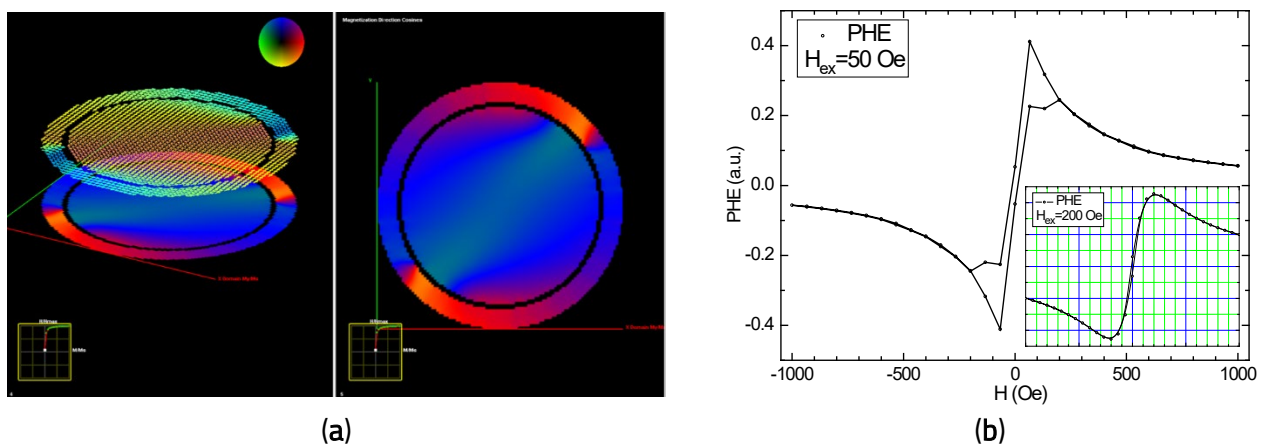


Figure 3.9. Multidomain micromagnetic simulation of a ring with inner disk permalloy structure: (a) Simulated structure snapshot for coercive field ( $H_c$ ), (b) calculated PHE signal for  $H_{ex} = 50$  Oe; the inset shows the PHE response for  $H_{ex} = 200$  Oe.

The different magnetization states in the ring with inner disk structure (according to the colour code), Figure 3.9a show the possibility of creating a Wheatstone bridge from resistive AMR elements where the arms of the bridge will have different variations in magnetic field. In the centre of the disk, a magnetic domain is magnetostatically linked (diagonally) with the ring magnetic spins.

### 3.1.3. Micromagnetic Simulations of GMR Sensors Behaviour

Some of the results presented in this section are published in the authored work [20].

To have a qualitative understanding of the operation process of GMR effect, micromagnetic simulation were performed on a conventional spin valve structure. These sensors are of AFM/FM/NM/FM type where FM are layers of  $\text{Ni}_{80}\text{Fe}_{20}$ , the AFM layer is usually IrMn and the NM is Cu (usually 0.1-2 nm thickness). The AFM layer acts as a pinning layer for the adjacent FM layer. Since AFM behaviour is difficult to simulate, the pinning of the FM layer magnetization (which can be assumed for low fields) can be simulated by applying a coupling field to the pinned layer.

Thus, calculating the behaviour of the magnetization from the free layer is a straightforward method of simulating the field dependency of the GMR sensor signal. The OOMMF (Object Oriented MicroMagnetic Framework) micromagnetic simulator was employed for this reason [183]. The simulated layer is made of Permalloy and is  $1000 \times 500 \times 10 \text{ nm}^3$ . Each cell in the layer is  $5 \times 5 \times 5 \text{ nm}^3$ . Through the NM layer, the FL and PL are antiferromagnetically connected with a coupling field of 200 Oe along the  $x$  axis. The field,  $H_{appl}$  is applied on the hard axis of magnetization ( $y$ -axis), Figure 3.14a. The material parameters are:  $M_S = 710 \text{ kA/m}$ , exchange constant,  $A = 1.3 \times 10^{-11} \text{ J/m}$ , and the uniaxial anisotropy constant  $K_u = 804 \text{ J/m}^3$  [20, 184].

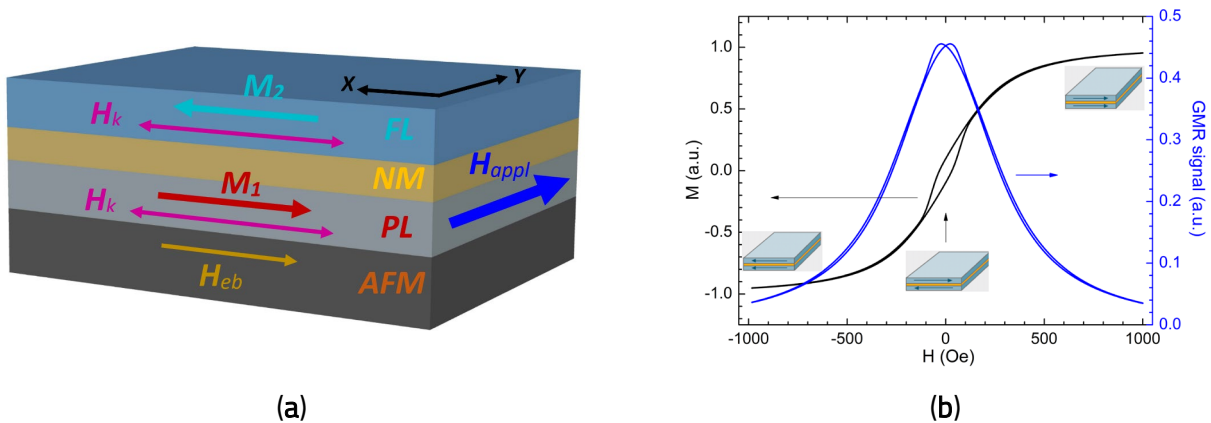


Figure 3.14. Simulated GMR spin valve structure: (a) Typical structure of spin-valve GMR sensors; (b) simulated dependence of the magnetization  $M_y$  and the calculated GMR effect when the field is applied on the hard axis of magnetization ( $y$ -axis).

The simulated GMR response can be represented as a function of the relative magnetization angle  $\theta$  between the free and pinned layer using a relation of the form  $a + b(1 - \cos \theta)$  [188]. Here,  $a$  specifies the structural resistance at saturation whereas  $b$  denotes the amplitude of the GMR effect. The estimated GMR response and the simulated field dependency of the magnetization along the  $y$ -axis,  $M_y$  are shown in Figure 3.14b. Even when the field is supplied over the hard axis, the small hysteretic behavior observed for the field dependency of  $M_y$  and GMR is caused by the magnetic

domain structure of the simulated layer. With a single-domain simulation method, there is no hysteresis for  $M_y$  and GMR, while hysteresis is present with a multi-domain approach.

### 3.2. Simulated Behaviour of Magnetoresistive Sensors Under the Influence of Magnetic Nanoparticles

#### 3.2.2. Micromagnetic Simulation of the GMR Spin Valve Structure for Magnetic Nanoparticles Detection

Simulating a more complex micromagnetic structure (such as the spin-valve multilayer in Figure 3.14a) is a task that cannot be handled by 2D micromagnetic solvers as it involves creating more than one layer. Moreover, if the interaction of such structures with other micromagnetic objects is of interest (for example interaction with magnetic nanoparticles), the complexity of the simulation increases significantly. Also, for these simulations, free, open-source software solutions are preferable. The Object Oriented Micromagnetic Framework (OOMMF) is a popular software solution that meets the necessary requirements. OOMMF uses the finite difference method (FDM) method for discretization [183, 189].

By utilizing code sources such as the one shown in Code A1.1 (Annex 1), several spin-valve simulations with both ferromagnetic and antiferromagnetic exchange coupling between the layers were performed for a square geometry structure. The parameters for the performed simulations can be seen in Table 3.3.

Table 3.3. Micromagnetic simulations parameters used for the OOMMF multidomain GMR spin-valve sensor structure.

Spin valve sensor structure parameters		Magnetic nanoparticle parameters	
Saturation Magnetization, $M_s$	800 kA/m	Saturation magnetization $M_s$	450 kA/m
In-plane dimensions ( $x, y$ )	200x200, 400x400, 600x600, 1000x1000 nm <sup>2</sup>	Dimensions $h_x \times h_y \times h_z$	40 x 40 x39 nm <sup>3</sup>
Exchange Constant $A_{ex}$	$1.3 \times 10^{-11}$ J/m	Sensor-particle distance (nm)	21 nm
Damping parameter $\alpha$	0.5	Particle to particle distance (nm)	40 nm
Bias field to the bottom layer	40 kA/m	Position of the particle ( $P_x, P_y$ ) 1 particle: $x_{range}, y_{range}$ : 80-120 nm, 2 particles: $x_{range}, y_{range}$ particle 1: 40-80 nm, 80-120 nm $x_{range}, y_{range}$ , particle 2: 120-160 nm, 80-120 nm; 4 particles: equidistant to each other	
Thickness of bottom/top layers	3 nm		
Mesh size	5 x 5 x 3 nm <sup>3</sup>		
Temperature	0 K		

Remark that a spacer between the ferromagnetic layers is placed as opposed to the nonmagnetic (NM) layer – this would not affect results. Due to the fact OOMMF uses the FDM method, and the cell size for the simulation is  $5 \times 5 \times 3 \text{ nm}^3$ , the resulting geometry of the particle is  $40 \times 40 \times 39 \text{ nm}^3$  which is close to the intended  $40 \text{ nm}$  spherical size. Moreover, due to better scaling between actual sensing elements and the magnetic nanoparticle size and also due to the significant computing time requirements for the simulations with magnetic nanoparticles (180-240 hours of simulation time), a  $200 \times 200 \text{ nm}^2$  spin-valve structure was chosen for the simulations with magnetic nanoparticles (MNPs). The particles were placed equidistant to one another and since the superparamagnetic behaviour cannot be reproduced by the simulator, a saturation magnetization of  $450 \text{ kA/m}$  was chosen for the MNPs.

Figure 3.22a shows the simulation results for the spin-valve structure with antiferromagnetic exchange between the top-bottom layers and 0, 1, 2, and 4 magnetic nanoparticles above the surface of the sensor. Figure 3.22b shows the simulated magnetization curve obtained for a single MNP.

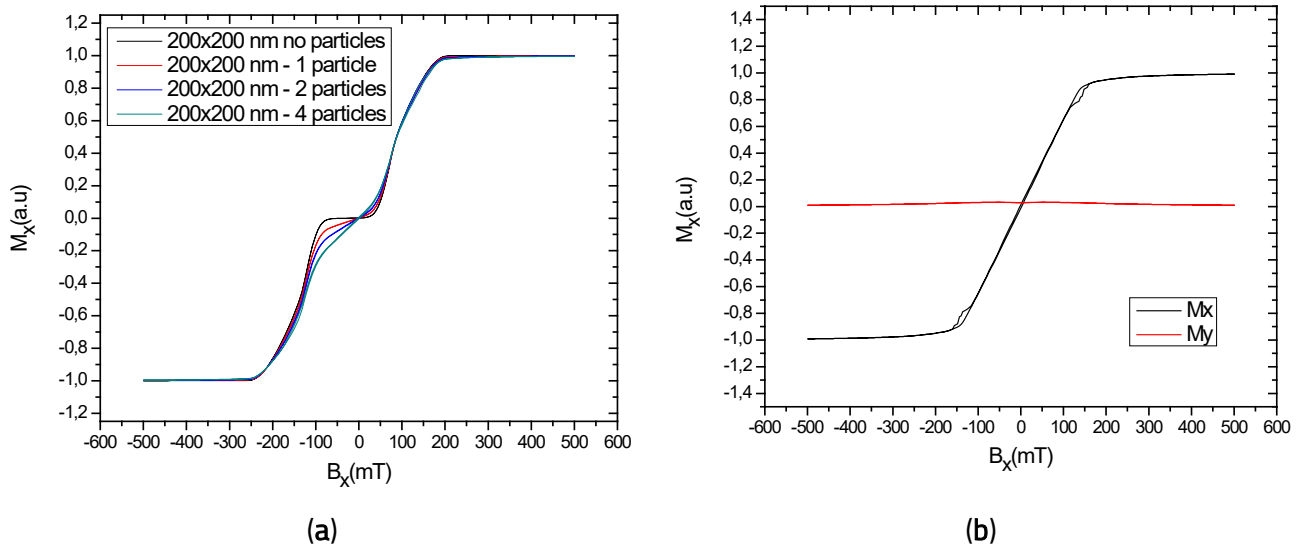


Figure 3.22. (a) Simulated dependence of the magnetization along the  $x$ -axis of a spin-valve structure for a GMR sensor with antiferromagnetic (AF) exchange coupling between the top and bottom layers and 0, 1, 2, 4 magnetic nanoparticles; (b) simulated field dependence of the magnetization along the  $x$ -axis of a  $40 \times 40 \times 39 \text{ nm}^3$  magnetic nanoparticle.

It can be concluded that, in terms of behavior of the simulated spin-valve structure, as the in-plane dimensions of the structure decreases, the obtained magnetization curve is similar, thus, smaller spin-valve structures can be used for simulations for significant simulation time savings. Also, simulating without the exchange coupling parameter, makes the magnetization curve switching more abrupt, unlike an actual GMR sensor response like in [20]. From Figure 3.22, it results that as the number of magnetic nanoparticles on the sensor surface increases, the obtained dependence of the magnetization more closely resembles that of a single magnetic particle.

### 3.3. Conclusions

1. The micromagnetic theory is an essential tool for determining the behaviour of magnetic sensors structures. When performing micromagnetic simulations, there are certain considerations that have to be considered:
  - The geometry discretization method is usually based FDM or FEM. Each software uses a different discretization method. Even though FEM is preferred compared to FDM since it leads to enhanced precision and reduced aliasing of irregular surfaces, FDM discretization can provide significant simulation time savings and still provide reliable results for specific geometries.
  - The single domain micromagnetic model (e.g. Stoner-Wohlfarth) can be sufficient for quick evaluation of specific magnetoresistive structures where some hysteresis effects can be neglected. More complex structures (e.g. spin valve) are better suited for multidomain simulations to accurately evaluate mechanism such as the exchange interaction between the coupled ferromagnetic layers.
  - Accurate geometric representation of the real sensing components (MNPs or sensor elements due to their very small size is sometimes not possible to be represented on micromagnetic simulator. In these situations, geometric approximations of the structure are acceptable.
2. Simulations performed utilizing SimulMag, LLG Micromagnetics, and Object Oriented Micromagnetic Framework (OOMMF) software highlight the behaviour of sensors based on AMR, PHE and GMR effects for magnetic field measurement.
  - Multi-domain simulation performed for PHE sensors demonstrate the influence of geometry and magnetic anisotropy on the magnetic characteristics for cross-shaped, square-shaped and ring-shaped sensor structures.
  - The simulated GMR spin valve structure allows to obtain the magnetic field characteristics under the presence and absence of magnetic nanoparticles on the surface of the sensor.
  - It was determined that shape anisotropy and magnetization localization effects provide much more significant differences.
3. The study performed demonstrated that modeling and simulations with micromagnetic theory are an essential step in the design and optimization process and for evaluating the field performance of prospective magnetoresistive sensors structures. However, due to the inherent challenges of electromagnetic disturbances that can disturb sensor performance for specific applications, especially in the low field region, macroscopic evaluation of the electromagnetic field sources around the sensor area may be necessary. This can be achieved either by experimental or analytical investigations to improve sensor geometric selectivity of magnetic field sources or by intentional functional setup improvements for specific applications.

## 4. Macroscopic Analytical Methods and Electromagnetic Simulations for Different Conductor Types

Electromagnetic modelling of magnetic field sources can provide great insight in optimizing the sensor setup and operational environment for better sensitivity and even new applications. This step is essential for applications that require high sensitivity in the low field area such as non-contacting current sensors and to minimize the requirement of adding electromagnetic shielding in magnetic sensors measurement setups (to reduce size and cost).

### 4.1. Magnetic Field Created by Current Flowing in Different Conductors

The analysis in this subchapter is based on general electromagnetic field theory and on reliable literature sources from books and courses [195, 196, 197, 198].

#### 4.1.2. Case of Rectilinear Circular-Cross Section Conductor

The analysis is made for the case of the infinite length conductor through which a current  $I$  passes. This case is detailed in Figure 4.4.

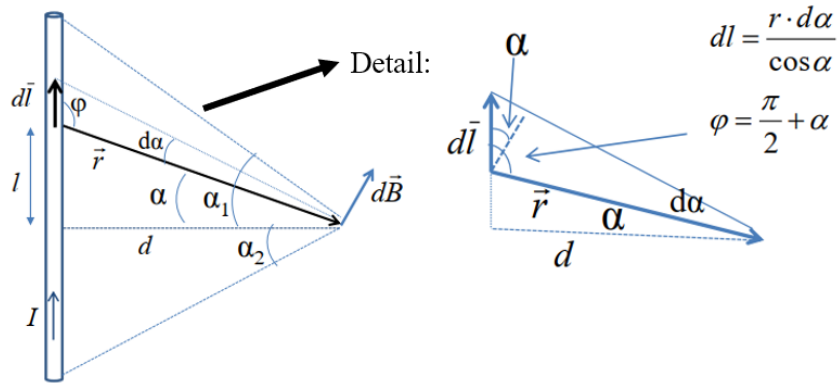


Figure 4.4. The magnetic flux density of the field created by a circular conductor traversed by a rectilinear current  $I$  in cartesian coordinates.

To calculate the magnetic flux density of the field created by the current  $I$ , eq. 4.12 is applied. In modulus, the elementary magnetic flux density is:

$$dB = \frac{\mu_0 I dl \cdot r \cdot \sin \varphi}{4\pi \cdot r^3}, \quad r = \frac{d}{\cos \alpha} \quad (4.12)$$

where the element of length is:

$$dl = \frac{r \cdot d\alpha}{\cos \alpha} \quad (4.13)$$

By integrating eq. 4.12, for a conductor of finite length, it results:

$$B = \frac{\mu_0 I}{4\pi \cdot d} \int_{-\alpha_1}^{\alpha_2} \cos \alpha \cdot d\alpha = \frac{\mu_0 I}{4\pi \cdot d} (\sin \alpha_2 + \sin \alpha_1) \quad (4.14)$$

For a conductor of infinite length, ( $\alpha_{1,2} \rightarrow \pi/2$ ), the field outside the conductor can be expressed as (in cartesian coordinates):

$$B = \frac{\mu_0 I}{2\pi d} \quad (4.15)$$

## 4.2. Magnetic Field Created by Current Flowing through Rectilinear Single and Multiple Traces

### 4.2.1. Analytical Method

Often, for modern electronics, the issue of detecting low current values accurately and reliable with low-cost solutions can prove critical. This section describes the analytical method authored and implemented firstly in [20] and further improved in [184] and [36]. As the analytical method followed an iterative improvement with single trace determinations in [20], multi-trace determinations in [184] and thickness and length corrections in [36]. Only the final version of the analytical method will be presented in this section, which was published in [36].

This study consists in developing a practical method of improving the sensitivity and accuracy of the response of a GMR-based current sensor. The novelty of the approach consists in utilizing a multiple trace current detection setup on a custom prototype PCB. In essence this would constitute a planar coil that will increase the usable field detected by the MR sensor. In support of these claims, an analytical model was developed for calculating the magnetic field in the MR sensing area. In terms of prospects, these methods of improving the sensitivity of MR sensors can be useful for several applications requiring low field detection.

If a current  $I$  passes through a conductive wire, the magnetic flux density  $B$  created by the current will produce a change in the output voltage of the nearby MR sensor. By properly designing the circuit that generates the magnetic field to be measured, the primary idea of the suggested setup is to increase the intensity of the magnetic field in the non-contacting current sensor area and, therefore, the accuracy and sensitivity. The MR sensors in the current measuring setup are magnetometers, therefore when a current  $I$  flows through a wire, the magnetic field  $B$  will cause the MR sensor's output to change. Figure 4.10 shows the structure and operation principle of the non-contacting current measurement setup with a current single and multi-traces.

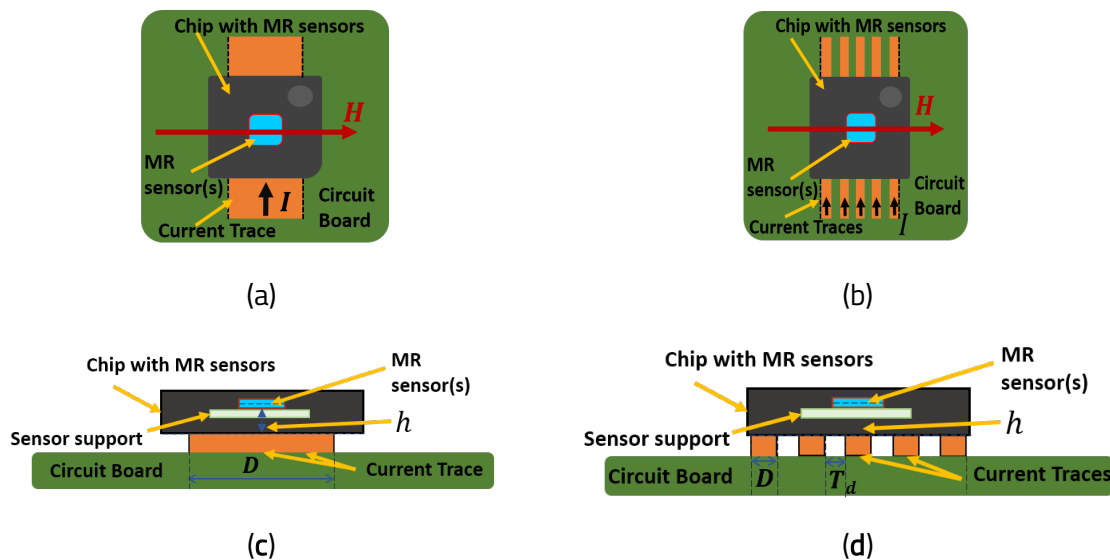


Figure 4.10. Working principle of the non-contacting current measurement setup utilizing current traces and a GMR based chip: (a) single plane section; (b) multi-trace plane section; (c) single trace cross section; (d) multi-trace cross section.

The magnetic field will be calculated in a point which corresponds to the center of the MR sensor centered above the trace. By utilizing multiple trace through which the same current to be detected passes, this will essentially constitute a planar coil. Figure 4.11.

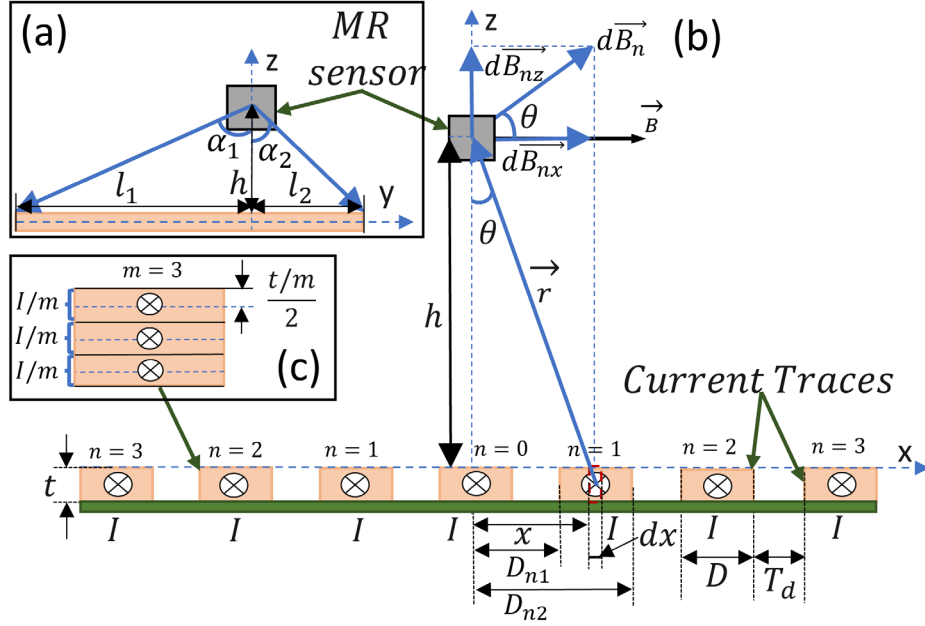


Figure 4.11. Analytical model to compute the magnetic field present in the sensor area: (a) Length correction of the magnetic field in the sensor area based on the distance from the linear trace ends; (b) Magnetic field components generated by the current through the trace and dimensional parameters; (c) Layered trace thickness parameters.

An analytical model considered in this case is based on Biot-Savart law, which assumes that the sensor is centered above the multiple trace at distance  $h$ . The thickness of each trace is divided by an  $m$  number of layers, consequently,  $h$ , changes for each individual layer (from the center of the layer).

For the finite length correction, the sum of the sine functions of the angles between the sensor area (above central trace) and for each end of the linear current trace is introduced (Figure 4.11). Some geometric corrections can still be introduced, especially for a large number of adjacent traces or nonlinear trace configurations.

By assuming a very long conductive trace, the elementary current  $dI$  distributed in the trace can be expressed by:

$$dI = \frac{I}{D} dx, \quad (4.38)$$

$$dB_n = \mu_0 \frac{dI}{2\pi r} = \mu_0 \frac{I dx}{D} \cdot \frac{1}{2\pi \sqrt{h^2 + x^2}} \quad (4.39)$$

$$dB_{nx} = dB_n \cdot \cos \theta = \mu_0 \frac{I dx}{2\pi D} \cdot \frac{1}{\sqrt{h^2 + x^2}} \cdot \frac{h}{\sqrt{h^2 + x^2}} \quad (4.40)$$

After some simplification, eq. 4.40 becomes:

$$dB_{nx} = dB_n \cdot \cos \theta = \mu_0 \frac{Ih}{2\pi D} \cdot \frac{dx}{h^2 + x^2} \quad (4.41)$$

After integration, eq. 4.41 becomes:

$$B_{nx} = \mu_0 \frac{Ih}{2\pi D} \int_{D_{n1}}^{D_{n2}} \frac{dx}{h^2 + x^2} \quad (4.42)$$

where  $\mu_0 = 4\pi \times 10^{-7}$  H/m is the vacuum magnetic permeability,  $D$  is the trace width,  $t$  is the trace thickness,  $h$  is the height on which the sensing element is placed above the trace, and  $\theta$  is the angle used to estimate the  $B_x$  component of the magnetic field.

By assuming a uniform linear current density,  $I/D$ , and integrating eq.4.42 from  $D_{n1}$  to  $D_{n2}$  we find:

$$B_{nx} = \frac{\mu_0 I h}{2\pi D} \cdot \frac{1}{h} \arctan \frac{x}{h} \Bigg|_{D_{n1}}^{D_{n2}} \quad (4.43)$$

By evaluating the integral, the  $x$  component of field generated by a trace  $n=1, 2, 3, \dots$ , in the sensor area is:

$$B_{nx} = \frac{\mu_0 I}{2\pi D} \left[ \arctan \left( \frac{D_{n2}}{h} \right) - \arctan \left( \frac{D_{n1}}{h} \right) \right] \quad (4.44)$$

If now, the length of the trace is taken into account, divide the thickness of the trace in  $m$  layers, and assume current distribution uniformity in the layers we get eq. 4.45. For the central trace, the result is shown in eq. 4.46:

$$B_{nx} = \sum_{i=0}^m \left( \frac{\mu_0 I}{2\pi D} \left[ \arctan \left( \frac{D_{n2}}{h_i} \right) - \arctan \left( \frac{D_{n1}}{h_i} \right) \right] \cdot (\sin \alpha_1 + \sin \alpha_2) \right) \quad (4.45)$$

$$B_{0x} = \sum_{i=0}^m \left( \frac{\mu_0 I}{\pi D} \left[ \arctan \left( \frac{D}{2h_i} \right) \right] \cdot (\sin \alpha_1 + \sin \alpha_2) \right), \quad (4.46)$$

where  $h_i$  is the specific distance from the sensor corresponding to each layer and can be expressed by eq. (4.47):

$$h_i = h + \left[ \left( \frac{t/m}{2} \right) + (m-1) \cdot \frac{t}{m} \right] \quad (4.47)$$

Parameters  $D_{n1}, D_{n2}$  can be computed in function of the number of traces,  $n$ , (Figure 4.11):

$$D_{n1} = \frac{D}{2} + (n-1)D + nT_d, \quad (4.48)$$

$$D_{n2} = \frac{D}{2} + nD + nT_d \quad (4.49)$$

Taking into account the problem symmetry, the  $z$  component of the magnetic field in the sensor will be cancelled by the fields from the left and right-side stripes, i.e.,  $B_{nz} = 0$ . Such that, the total field generated in the sensor area can be expressed as:

$$B = B_0 + 2B_1 + 2B_2 + \dots + 2B_n \quad (4.50)$$

An example calculation for eq. 4.44 and eq. 4.50 by utilizing specific parameters for a multitrace structure with up to 11 traces ( $n=5$ ) and without length and thickness correction is made in Annex 2.

In order to validate the results that can be obtained with the analytical method, a study based on four possible cases for this analytical method was performed:

Case I- Infinite trace length, with a single layer (trace thickness neglected);

Case II- Infinite trace length, with  $m = 35$  layers (1  $\mu\text{m}$  each layer);

Case III- finite trace length, with a single layer (trace thickness neglected);

Case IV- finite trace length, with  $m = 35$  layers (1  $\mu\text{m}$  each layer).

For Case II and Case IV, layered trace thickness means that the thickness of each trace is divided on a number of layers through which we assume a constant current,  $I/m$  is flowing (where  $m$  is the number of layers).

Some of the results in this study were published in the authored work in [36].

#### 4.2.2. U-shaped Trace and Planar Coil Simulations and Experimental Validation

Two cases were investigated utilizing finite elements approach simulations to perform a comparative examination of the outcomes achieved with the analytical method. Firstly, a U-shaped current trace (Figure 4.12a) was modelled to mimic the behavior of two MR sensors in a double differential setup. This follows the single trace analytical method. The capacity to integrate extremely sensitive and tiny magneto-resistive sensors, in a double differential configuration in a very compact package, is the basis for the precise dimensions of the U-shaped trace. Secondly, a comparison is made between the findings of the experiment and the situation of a multi-trace planar coil, Figure 4.12b.

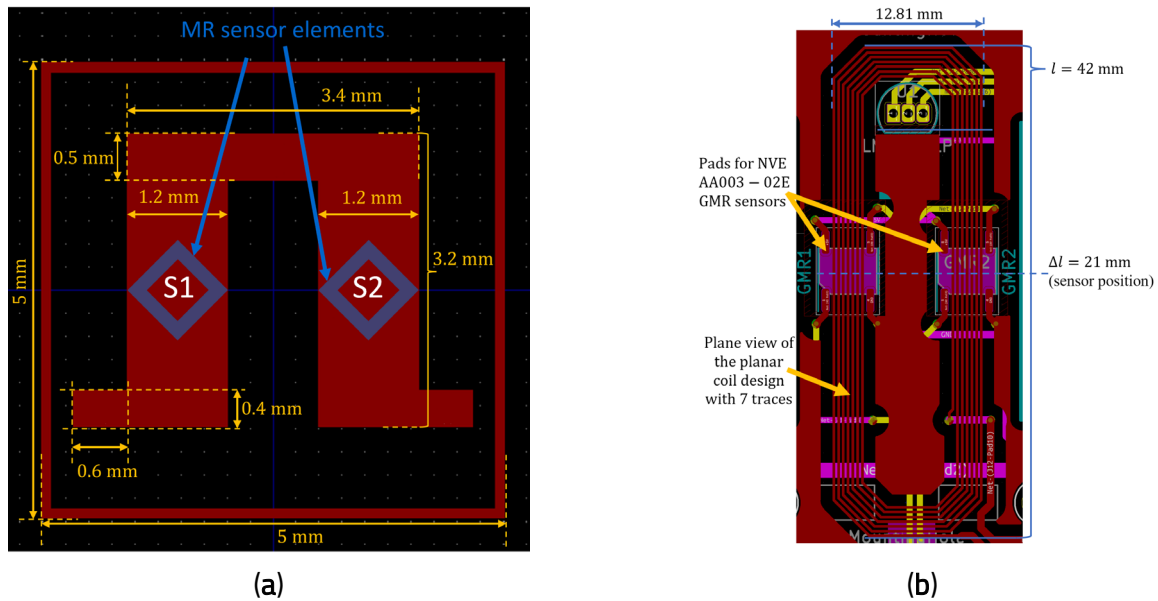


Figure 4.12. Design and experimental implementation of (a) Geometry and parameters for the U-shaped trace; (b) View of the planar coil with seven traces.

The U-shaped trace's precise measurements are determined by how well it can combine miniaturized, highly sensitive magneto-resistive sensors, like the ones in [199]. Table 4.1 displays the specific parameters used for the analytical model and the FEM simulation.

COMSOL Multiphysics® software was used to perform the modeling [200]. It should be noted that the planar coil was modeled with Cu material values and had a resistivity of  $1.72 \times 10^{-8} \Omega\text{m}$  in COMSOL, while the U-shaped trace was modeled using Ag material properties and had a lowered resistivity of  $1.36 \times 10^{-7} \Omega\text{m}$  to match the experimental measurement (the U-shaped trace was printed with a silver-based ink). The experimental setups used for experimental validation are presented in Chapter 6. Table 4.1 shows specific parameters utilized for the analytical model and FEM simulation.

Table 4.1. Parameters utilized for the analytical model and COMSOL simulation of U-shaped trace and planar coil.

Symbol	Parameter Name	Quantity	
$D$	Trace width	Planar coil with 7 traces: 0.22 mm	
		U-shaped trace: 1.2 mm	
$T_d$	Distance between traces	Planar coil with 7 traces: 0.19 mm	
		U-shaped trace: N/A	
$I$	Current through trace	0.1 A	
$h$	Distance between Sensor and trace	Planar coil with 7 traces: 0.045 [mm] to 3.58 [mm]	
		U-shaped trace: 0.045 mm to 2.08 mm	
$t$	Trace thickness	35 $\mu\text{m}$	
$m$	Number of layers in which $t$ is divided	35 (1 $\mu\text{m}$ each layer)	
$L$	Trace length	Planar coil with 7 traces: 42 mm	
		U-shaped trace: 3.2 mm	
$\Delta l$	Sensor position on trace length <sup>1</sup>	Planar coil with 7 traces: 21 mm	
		U-shaped trace: 1.6 mm	
$V_s$	Sensor input voltage	U-shaped trace setup: 4.399 V	
		Planar coil setup: 4.096 V	
$S$	Sensor sensitivity	U-shaped trace sensor setup:	$S_1$ : 159 $\mu\text{V}/(\text{V} \times \text{A}/\text{m})$ (0.01268 mV/V-Oe)
			$S_2$ : 188.54 $\mu\text{V}/(\text{V} \times \text{A}/\text{m})$ (0.0150034 mV/V-Oe)
			$S_{\text{differential}}$ : 347.94 $\mu\text{V}/(\text{V} \times \text{A}/\text{m})$ (0.0277 mV/V-Oe)
		Planar coil sensor setup:	$S_{\text{differential}}$ : 32.67 $\mu\text{V}/(\text{V} \times \text{A}/\text{m})$

<sup>1</sup> The sensor position on the trace length is given by:  $\Delta l/L \cdot 100$  [%].

The magnetic field intensity distribution along the  $x$ -axis from the COMSOL simulations is displayed in Figure 4.13a for the U-shaped trace while Figure 4.13b displays the planar coil. Data were extracted for locations of interest at height  $h$  above the sensor (notice the insets in Figures 4.14-4.16) along longitudinal lines, and transverse lines, Figures 4.14a and Figure 4.14b for the U-shaped trace, and Figure 4.14 and Figure 4.15 for the multi-trace planar coil.

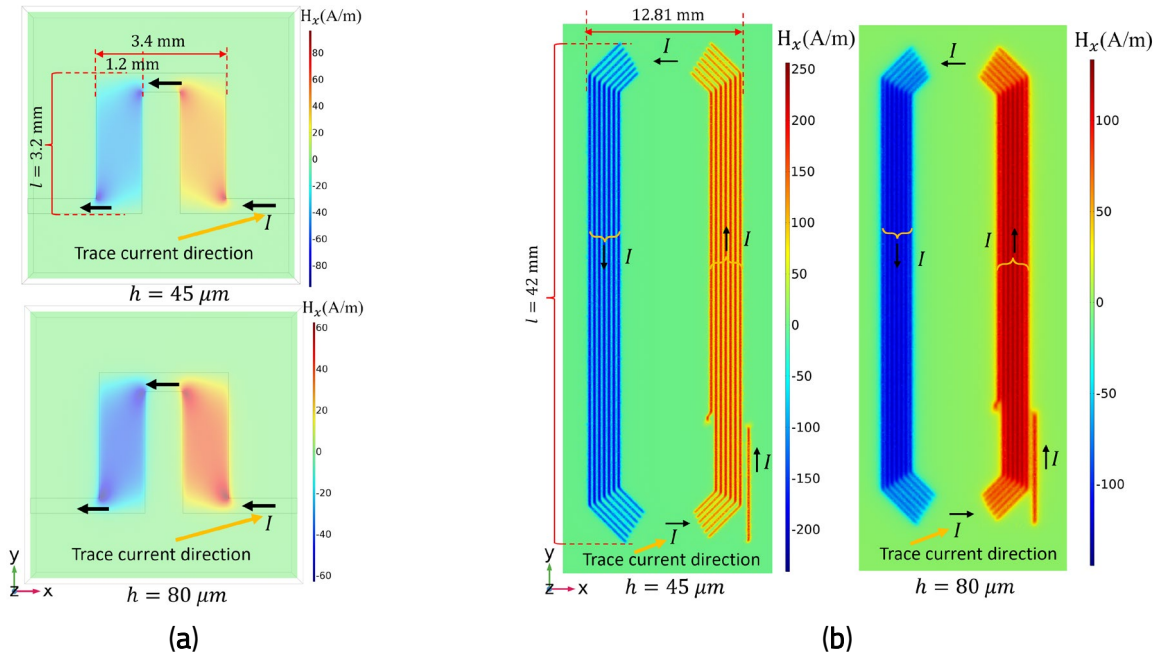


Figure 4.13. Magnetic field distribution on the  $x$ -axis for the U-shaped trace and planar coil for a 100 mA current according to COMSOL simulations: (a) U-shaped current trace:  $H_x$  field distribution at height  $h = 45 \mu\text{m}$  ( $H_{x\_sensor} = 40.630 \text{ A/m}$ ) and  $h = 80 \mu\text{m}$  ( $H_{x\_sensor} = 39.056 \text{ A/m}$ ) from the current trace; (b) Multitrace (7 traces):  $H_x$  field distribution at height  $h = 45 \mu\text{m}$  ( $H_{x\_sensor} = 126.67 \text{ A/m}$ ) and  $h = 80 \mu\text{m}$  ( $H_{x\_sensor} = 121.94 \text{ A/m}$ ) from the current trace.

Figures 4.14-4.15 show that there is a minimum magnetic field intensity between the traces and that the magnetic field intensity is greatest near the trace's centre. In Figure 4.15, any nonlinearities in the graph are not due to the field actual distribution, but from the mesh distribution of the object for the simulation, since at the same height from the trace and relative positioning, the field is constant.

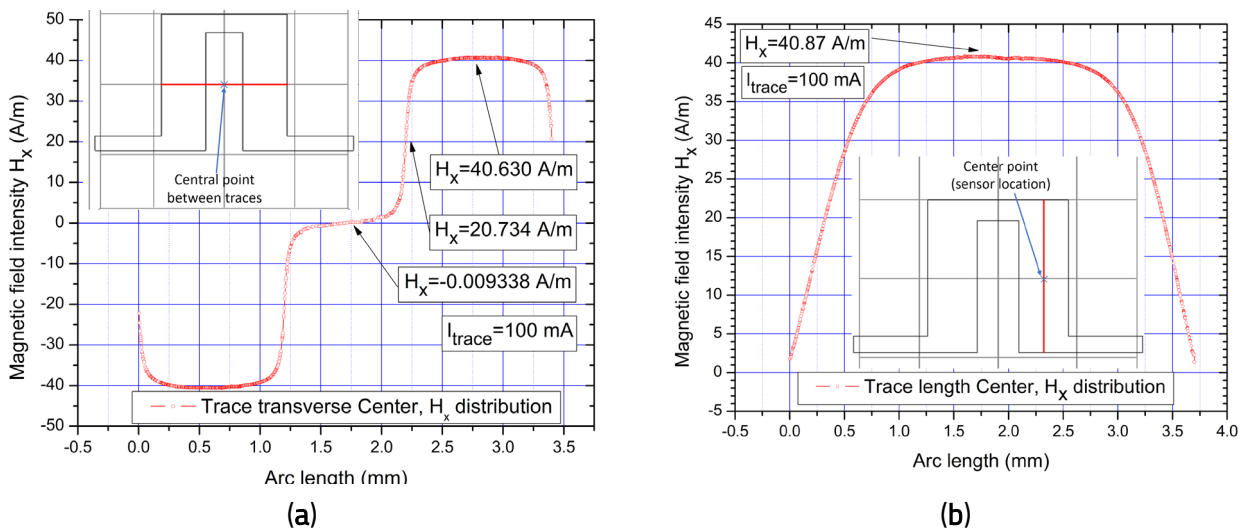


Figure 4.14. Magnetic field intensity along the  $x$ -axis direction, variation for the U-shaped trace at height  $h = 45 \mu\text{m}$  according to results from COMSOL simulation (note the insets): (a) transverse center line (b) longitudinal center line.

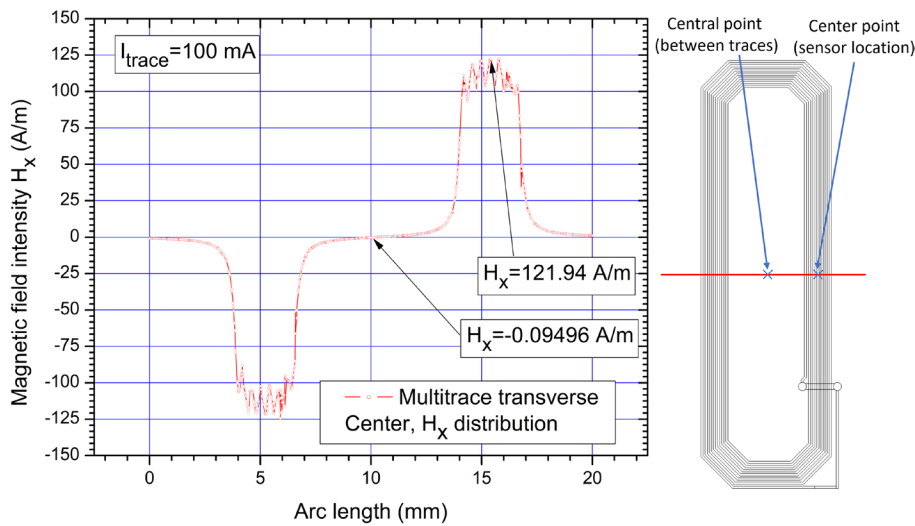


Figure 4.15. Transverse center line (note the inset) magnetic field intensity on the  $x$  direction, variation for the Multitrace planar coil with 7 traces at height  $h = 80 \mu\text{m}$  from the trace according to results from COMSOL simulation.

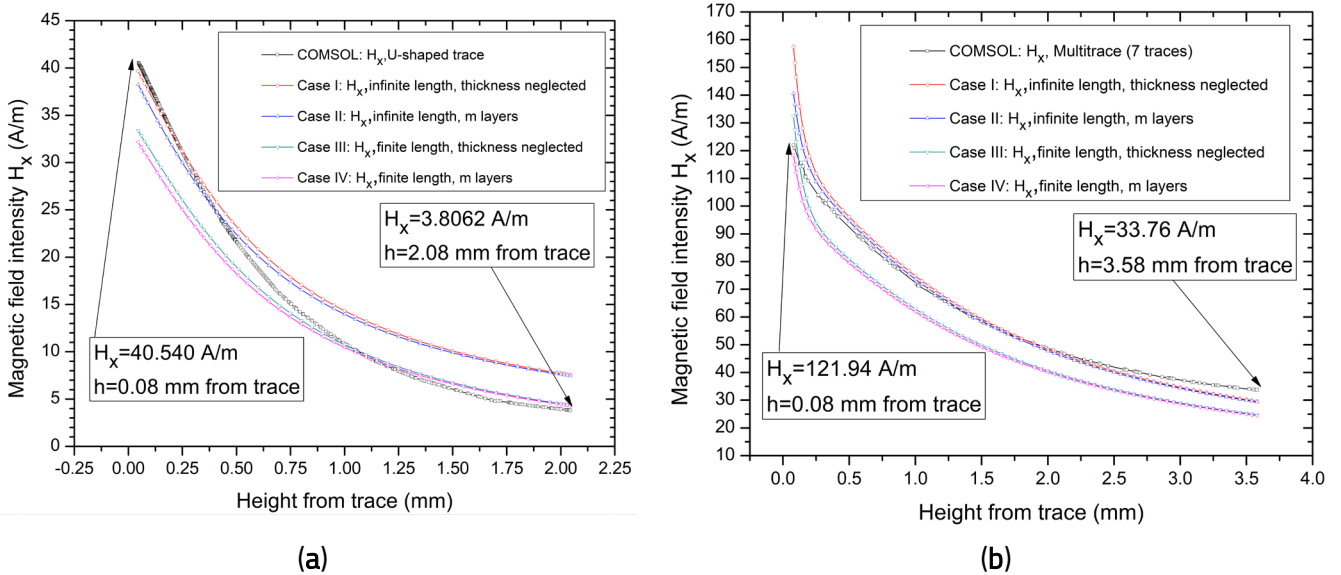


Figure 4.18. Magnetic field intensity  $H_x$ , variation for different  $h$  according to COMSOL simulation and from the analytical model: (a) for the "U-shaped current trace with  $h$  from 0.08 mm to 2.08 mm: (b) for the "Planar coil with 7 traces" with  $h$  from 0.08 mm to 3.58 mm. The current through the trace was 100 mA.

The results presented in Figure 4.18a demonstrate how the analytical model converges to the COMSOL simulation results in the following manner (for the U-shaped trace): for higher field values and correspondingly closer distances from the trace, the cases where a very long conductive trace is assumed (Case I and Case II) are closer to the COMSOL results, while results for the finite model (Cases III and IV) more closely converge to the COMSOL results at larger distances from the trace. Furthermore, in the case of the planar coil arrangement (Figure 4.18b), Case I and Case II yield findings that are comparable to the simulation at closer distances from the coil, whereas Case III and IV exhibit the opposite behavior as in the case of a single trace: they converge more closely at farther distances.

The methodology of analysis for the seven traces planar coil is compared with experimental results from [184], and Table 2 presents validation data for the central point (notice inset from Figure 18a) between the COMSOL simulation results and the analytical method. The findings displayed in Table 4.2 were obtained using the parameters listed in Table 4.1. It should be noted that the field values are computed for the following distances from the conductive trace: 0.8 mm or 0.08 mm, since the planar coil experimental setup used the AA003-02 encapsulated sensors [201], and 45  $\mu\text{m}$  (the thickness of the Kapton tape on which the trace is printed) and 80  $\mu\text{m}$  distance between the sensor and the trace for the *U*-shaped trace.

Table 4.2. Comparative analysis between COMSOL simulation, analytical model, and experimental data.

Trace type	Validation case		$h^1$ (mm)	$H_x$ (A/m)	$V_{out}^2$ (mV)	$V_{\text{differential}}^2$ (mV)	
U-shaped trace <sup>3</sup> (Figure 4.12a) $I_{\text{trace}} = 100 \text{ mA}$ $V_s = 4.399 \text{ V}$	COMSOL simulations		0.08	39.056	–	–	
			0.045	40.630	–	–	
	Analytical method	Case I: Infinite length, $t$ neglected	0.08	38.150	$S_1: 0.02675$ $S_2: 0.03164$	0.05839	
			0.045	39.680	$S_1: 0.02782$ $S_2: 0.03291$	0.06073	
		Case II: Infinite length, $m = 35$ layers (1 $\mu\text{m}$ each layer)	0.08	36.7321	$S_1: 0.02575$ $S_2: 0.03046$	0.05622	
			0.045	38.2408	$S_1: 0.02681$ $S_2: 0.03171$	0.05853	
		Case III: Finite length, $t$ neglected	0.08	32.0769	$S_1: 0.02249$ $S_2: 0.0266$	0.04910	
			0.045	33.3818	$S_1: 0.02341$ $S_2: 0.02768$	0.05109	
		Case IV: Finite length, $m = 35$ layers (1 $\mu\text{m}$ each layer)	0.08	30.8842	$S_1: 0.02165$ $S_2: 0.02561$	0.04727	
			0.045	32.1704	$S_1: 0.02255$ $S_2: 0.02668$	0.04924	
	Experimental results		0.045	31.7423	$S_1: 0.0198$ $S_2: 0.022$	0.042	
	Planar coil with 7 traces <sup>3</sup> (Figure 4.12b) $I_{\text{trace}} = 100 \text{ mA}$ $V_s = 4.399 \text{ V}$	COMSOL simulation		0.8	79.780	–	–
				0.08	121.94	–	–
		Analytical method	Case I: Infinite length, $t$ neglected	0.8	82.5885	11.8702	23.7404
0.08				157.422	22.6257	45.2514	
Case II: Infinite length, $m = 35$ layers (1 $\mu\text{m}$ each layer)			0.8	81.2428	11.6768	23.3536	
			0.08	140.624	20.2115	40.423	
Case III: Finite length, $t$ neglected			0.8	67.9498	9.9838	19.9676	
			0.08	132.465	19.0388	38.0776	

	Case IV: Finite length, m = 35 layers (1 $\mu\text{m}$ each layer)	0.8	66.8427	9.821	19.642
		0.08	118.331	17.0073	34.0146
	Experimental results	0.8	–	10.716	21.432

<sup>1</sup> Distance between the sensing element and the current trace. Note that 0.045 mm is the distance between the sensors and the *U*-shaped trace in the experimental setup and 0.8 mm is the distance between the sensing element and the current trace in the experimental setup for the planar coil with the AA003-02 sensors [201].

<sup>2</sup> Output voltage for a single sensor ( $V_{out}$ ) and for the two sensors in differential configuration ( $V_{differential}$ ).

<sup>3</sup> Sensors supply voltage in differential configuration.

### 4.3. Conclusions

1. The analytical models and macroscopic electromagnetic simulations are advantageous methods for optimizing and improving the geometric selectivity of magnetoresistive sensors, applied especially for non-contacting current measurement applications, in which trace shape, length and structure design can radically affect the magnetic field generated by the measurement current in the sensor area. In this case, optimization of the current trace design means purpose-made geometric characteristics of the current trace applied to specific sensor designs.

2. By utilizing electromagnetic theory, several specific analytical models and simulation are developed to estimate with a very good degree of accuracy the magnetic field intensity generated in the magnetoresistive sensor area.

- The models for single, rectangular, and toroidal conductors in which DC current flows have been developed and the magnetic field intensity in different points are calculated, for establishing the optimal approach for implementing a conductor type for a non-contacting magnetoresistive current sensor.
- Coil type conductors provide good field uniformity and magnetic field intensity for a given current, but due to their inherent size, coil type conductors are difficult to be implemented in miniaturized applications.
- The model for rectilinear single and multiple traces is developed and the expression of magnetic field intensity created by current flowing through the traces is obtained.

3. For a U-shape trace and planar coil the study performed considers different parameters for trace material and geometries of traces.

- The analytical method included four study cases: neglecting the thickness of the trace, dividing the thickness of the trace in several layers, finite or very long conductive trace, and several adjacent traces in the sensor area.
- The comparison with experimental study shows that the case of the analytical model when the trace is finite in length and the thickness of the trace is taken into account and divided in an appropriate number of layers is the most accurate. However, for longer trace lengths, models which neglect the length of the trace can prove more accurate and are closer to the COMSOL FEM model.
- The analytical method was validated using finite elements method COMSOL simulations and experimental results.

These results can prove very useful for designing and optimizing applications that contain current traces such as non-contacting current sensors and also for magnetic nanoparticles detection as some measurement methods involve polarizing the magnetic nanoparticles with a biasing field that can be produced either by a coil or a current trace.

## **5. Magnetic Nanoparticles Detection with Magnetoresistive Sensors**

### **5.1. Magnetic Method Applied for Magnetic Nanoparticles Detection**

The intrinsic characteristics of magnetic field sensors (high scalability, sensitivity and integrability with semiconductor integrated circuits) make them a great choice for detecting magnetic nanoparticles (MNPs).

### **5.2. Experimental Studies for Magnetic Nanoparticles Detection with GMR sensors**

The focus of this study is to develop two experimental setups and several methods for improving the performance and characteristics of GMR sensors systems for MNPs detection. The first method relies on analysis of the derivative of the output signal of the sensor to determine the presence and concentration of MNPs. The work presented in this section can be found in the authored work [235]. The second method involves a custom-built printed circuit board to optimize geometric selectivity and overall efficiency of the detection setup. Through the second method, DC testing and AC magnetorelaxometry experiments were performed for detecting MNPs. Finally, integration with microfluidics setups is demonstrated through three different approaches: microfluidic chamber, two microfluidic channels and a single microfluidic channel.

The potential utility in biosensing and LOC applications is demonstrated by this study, which proved the capacity to detect magnetic nanoparticles using a sensor based on the giant magnetoresistance (GMR) effect. Experimental measurements provided proof of the working concept.

#### **5.2.1. Detection with Analysis of the Derivative of the Output Signal**

High sensitivity magnetic field sensors based on the GMR effect can be patterned at microtechnology research labs [10] or found as commercial goods [13, 95]. The GMR sensor employed in this investigation, comes in a flip-chip package from Sensitec GmbH in Germany [13]. Four GMR components are connected in a Wheatstone bridge configuration to form the sensor (Figure 5.7a, b, c). While the other two GMR structures are covered by flux concentrators and serve as reference elements to complete the Wheatstone bridge, two structures are positioned within the gap of a magnetic flux concentrator (MC). As a result, the sensor output voltage has very high thermal stability, ranging from around  $-0.35\%/K$  to  $13\text{ mV/V/Oe}$  in the linear range of  $-10$  to  $10\text{ Oe}$  [13].

The GF708 chip was wire bounded and mounted on a platform which was connected to the measurement system composed from a Keithley 6221A current source and a Keithley 2182A nanovoltmeter to read the output voltage from sensor. The platform with the chip was mounted inside of a system composed from a dual Helmholtz coils setup that can provide a very uniform magnetic field. The coils were connected to a programable power supply source Kepco BOP100-10MG. All these devices, presented in Figure 5.7d, were computer interfaced.

The horizontal coils (Figure 5.7d) are used to apply a magnetic field perpendicular to the sensors in order to study the possible influence of this perpendicular field,  $H_p$  component on the sensor's response. Figure 5.8 presents the field characteristics of the sensor without MNPs over his surface for the perpendicular field,  $H_p = 0$  and 25 Oe.

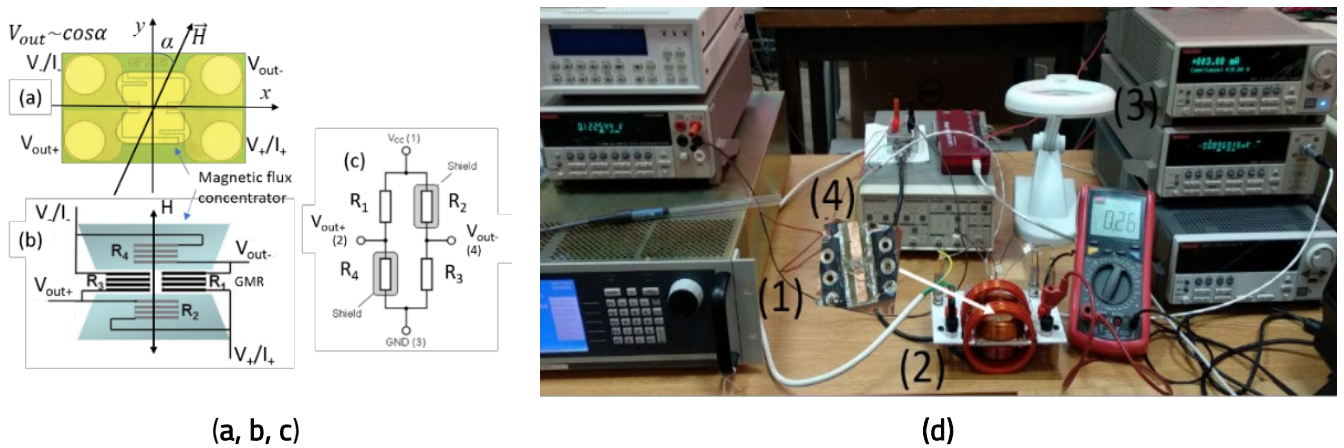


Figure 5.7. Overview of the GF708 sensor and experimental setup: (a) GF708 view from the bump-side, (b) and (c) simplified schematic of the sensor with active GMR structures ( $R_1$ ,  $R_3$ ) and screened structures ( $R_2$ ,  $R_4$ ); the maximum sensitivity is obtained when  $H_{appl}$  is directed over  $y$ -axis; (d) The experimental setup for characterizing the GF708 sensor: (1) Kepco BP 100-10MG, (2) the dual Helmholtz coil setup, (3) the Keithley 6221A current source and 2182A nanovoltmeter and (4) the platform with the GMR chip.

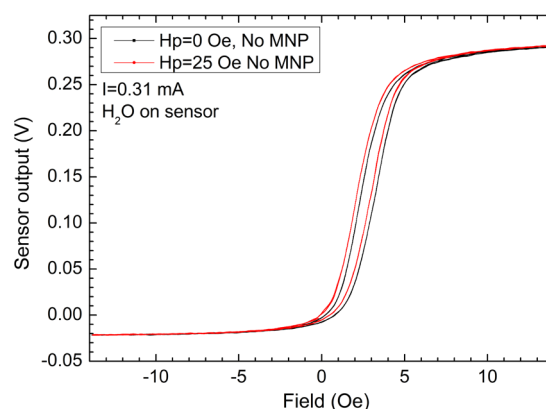


Figure 5.8. GF708 Field characteristic in the presence and absence of a perpendicularly applied magnetic field.

A drop of  $1 \mu\text{l}$  of water was placed above the chip surface to have a similar thermal equilibrium state like when the solution with magnetic nanoparticles (MNPs) is placed above the sensor. During experiments, the sensor's current was set at 0.31 mA. From Figure 5.7a it can be

observed that the sensor is insensitive to perpendicular applied fields. This behaviour is due to the fact that the demagnetizing coefficient over the direction perpendicular to the film surface is close to  $-1$  ( $N_{\perp} \approx -1$ ), which forces the magnetization to stay in the film plane. The small displacement observed is due to a very weak in plane component of  $H_p$ .

The calculated derivatives of the output signal (Figure 5.9) give two peaks that correspond to the switching fields in the sensing layer (free layer) whose magnetization rotates under the applied field. Figure 5.9a and Figure 5.9b show that the width of the hysteresis curve,  $\Delta H_C = 1.2$  Oe, is the same both for  $H_p = 0$  and  $H_p = 25$  Oe. Only a small displacement, of about 0.3 to 0.4 Oe, is observed due to the in-plane component of  $H_p$ . However, it is expected to observe a change of the switching fields when MNPs will be placed above the sensor's surface, as is depicted in Figure 5.10.

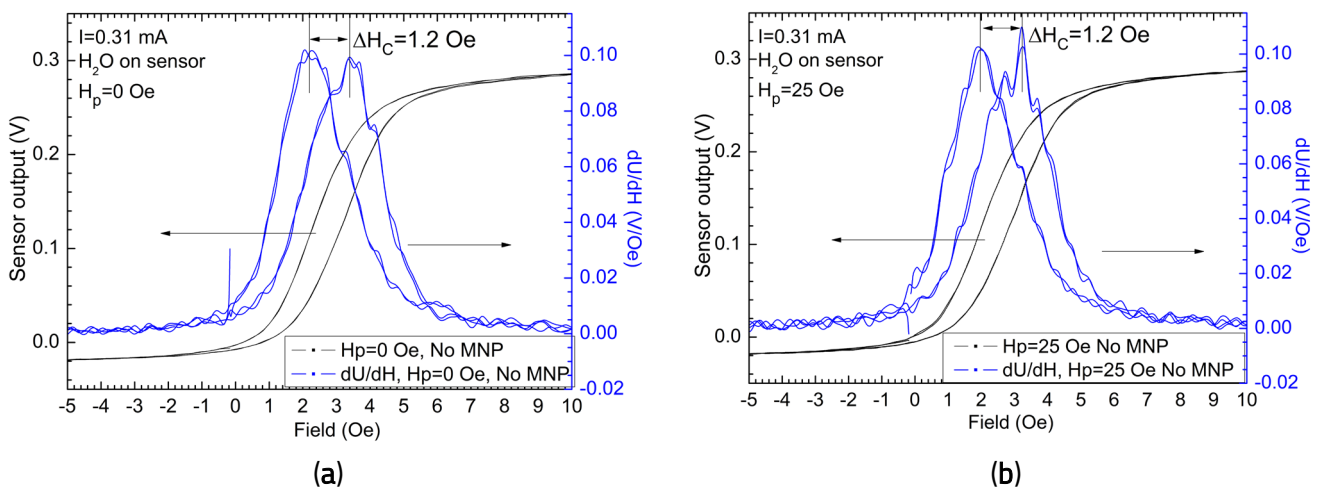


Figure 5.9. The magnetization curves and derivatives of the GF708 GMR output signal for (a)  $H_p = 0$  and (b)  $H_p = 25$  Oe without MNPs on the sensor surface.

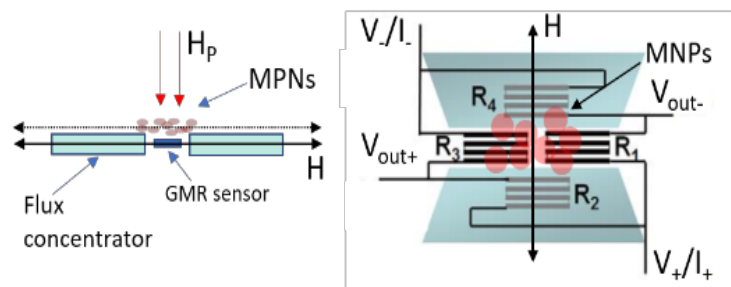


Figure 5.10. Working principle of the GMR sensor with MNPs placed on its surface: cross section and plane view schematic representation.

Utilizing the configuration showcased in Figure 5.7, and adhering to the previously delineated measurement protocol, varying quantities of MNP-containing solution were applied over the sensor surface. The MNPs are made up of 10 nm-diameter Maghemite ( $Fe_2O_3$ ) nanoparticles functionalized with Polyethylene glycol 6000 (PEG 6000) and suspended in water. Different antibodies can be added to these functionalized MNPs in order to employ them for biodetection of particular antigens. Finally, the number of distinct antibody-antigen binding processes can be approximated based on the magnetic material present above the sensor's surface. In this work, the detection capabilities of the GMR-based system with Maghemite MNPs previously mentioned for these MNPs was

demonstrated. A continuous magnetic field,  $H_p=25$  Oe, perpendicular to the sensor surface was applied in order to improve the magnetic field created by the MNPs and, consequently, the detection sensitivity. This field will magnetize the MNPs but will not significantly affect the behavior of the sensor.

Figure 5.11a presents the field dependences of the output voltage when a drop of  $1.25 \mu\text{l}$  of solution with maghemite nanoparticles functionalized with PEG 6000 was placed above the chip surface. For comparison, the output signal when only a drop of water was placed above the chip surface is also plotted, Figure 5.11a. It should be emphasized that the response curve deforms at higher fields as expected by the basic micromagnetic simulations. A stronger field is needed to switch the magnetization in the sensing layer and achieve saturation because the MNPs placed over the sensor surface act like shunting layers. By analysing the output signal through its derivative and expressing  $dU/dH = f(H)$  as in Figure 5.9, this behavior can be more accurately described.

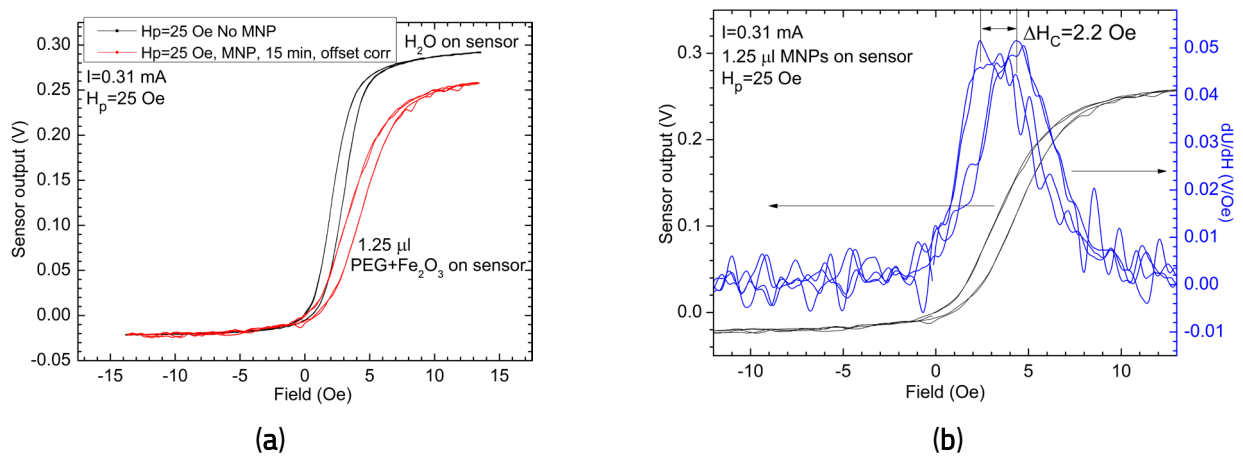


Figure 5.11. (a) The field dependences of the output signal with and without MNPs over the sensor surface and (b) The calculated derivative of the output signal in the presence of MNPs.

This technique allows for the accurate determination of the switching fields, which serve as a marker for the presence of MNPs above the sensor surface. When comparing the response curve with the scenario without MNPs above the sensor, a shift of 0.8 Oe is discovered, and the hysteresis curve's width is now  $\Delta H_C=2.2$  Oe.

By using the procedure outlined in [22] and [184], the mass of MNPs found in these experiments can be determined. As a result, it was deduced that  $1.25 \mu\text{l}$  of solution contained  $16.7 \mu\text{g}$  of powder made of 10 nm-diameter maghemite nanoparticles functionalized with PEG 6000. This translates to roughly  $1.20 \mu\text{g}$  of pure maghemite cores, with PEG 6000 molecules making up the rest bulk. Using data from the magnetization curves of the PEG6000 functionalized MNPs it was estimated that the experimental system determined a magnetic moment of about  $9.098 \cdot 10^{-5}$  emu for a signal fluctuation of 0.035 V (i.e., a detection sensitivity of approximately 75.81 emu/g).

### 5.3. Conclusions

1. The surface detection method of MNPs with magnetoresistive sensors is the most sensitive and implies simpler electronics, but it requires a complex process of washing the surface after each measurement. Also, the lack of electrodes gives endurance to multiple washing processes. Other specific aspects for the detection of MNP by thin-film MR sensors are:
  - MNPs from  $\text{Fe}_2\text{O}_3$  or  $\text{Fe}_3\text{O}_4$  present a superparamagnetic behavior at room temperature;
  - The sensors are very susceptible to in-plane magnetic fields, and low susceptibility to magnetic fields applied perpendicular to the surface;
  - MR sensors saturate at fields not greater than 0.01 T and the detection process is highly influenced by the magnetostatic interaction between the sensor surface and MNPs. In this case, the superparamagnetic behavior of the MNPs is necessary to eliminate both the false positive detection signals and clustering processes in the liquid volume and on the surface of the sensor.
2. When it comes to using magnetoresistive sensors for biomedical applications, the same design rules and optimizations can be applied as for other MR sensor applications. However, most of the time the design requires modifications for biosensor use as integration of MR biosensors into lab-on-a-chip devices has several requirements.
3. A complex experimental study with GMR sensor was performed for optimizing the detection of MNPs with exchange-biased spin valve structures for improving the performance and characteristics of GMR sensors systems for MNPs detection. The first method relies on analysis of the derivative of the output signal of the sensor to determine the presence and concentration of MNPs. The experimental system determined a magnetic moment of about  $9.098 \cdot 10^{-5}$  emu for a signal fluctuation of 0.035 V (i.e., a detection sensitivity of approximately 75.81 emu/g). The second method involved a custom-built PCB to optimize geometric selectivity and overall efficiency of the detection setup. DC testing and AC magnetorelaxometry experiments were performed for detecting MNPs. DC tests showed reasonable performance while magnetorelaxometry showed the usefulness of FFT spectral analysis for high frequency AC fields for analysing the presence of MNPs. Also, integration with microfluidics setups is demonstrated through three different approaches: microfluidic chamber, two microfluidic channels and a single microfluidic channel.
4. The research described in this chapter demonstrated the MNPs detection application possibilities of developed magnetoresistive sensors systems. The obtained method and results can be further improved and applied to develop very sensitive and integrated magnetoresistive biosensor setups, with an end goal for Lab-on-a-chip implementation of highly specialized biological measurements, which will significantly reduce analysis costs and improve accessibility of personalized healthcare.

## 6. Development of Non-Contacting Current Measurement Devices based on Magnetoresistive Sensors

In this chapter the author contributions in the design and construction of non-contacting current measurement devices with the AMR, GMR and TMR sensors are described. The developed experimental installations and proposed magnetoresistive sensors are detailed. Through experimental measurements the performance of current measurement devices is validated for non-contacting measurement applications.

### 6.1. Design, Construction and Characterization of an AMR Bridge Sensor

The result of this research is part of the published authored work in [36].

#### 6.1.1. Design and Operation of the AMR Bridge Sensor

The working principle of the AMR Bridge sensor is shown in Figure 6.1 while the design that operates as the demonstrator chip's layout is displayed in Figure 6.2. In order to minimize the impacts of temperature changes and interference from external magnetic fields, this implementation, which consists of two identical sensors, aims to define magnetoresistive structures tailored to the magnetic field produced by electric currents. Since every AMR bridge is a differential sensor, the two sensors chip displays a double differential measurement system. Note that the structure is within a square of  $4 \times 4 \text{ mm}^2$  and was realized on a  $5 \times 5 \text{ mm}^2$  chip. The margins are 0.5 mm while the arm of the bridge has a length  $L = 1 \text{ mm}$  and a width of either 0.1 or 0.2 mm. The contacting pads size can be reduced such that the chip can fit inside a  $3 \times 3 \text{ mm}^2$  footprint.

A U-shaped silver trace was designed and fabricated and placed on top of the sensor. Using a Voltera V-One prototype machine, the U-shaped trace was printed on top of a  $45 \text{ }\mu\text{m}$  thick Kapton band [240]. The sensors were positioned above this band.

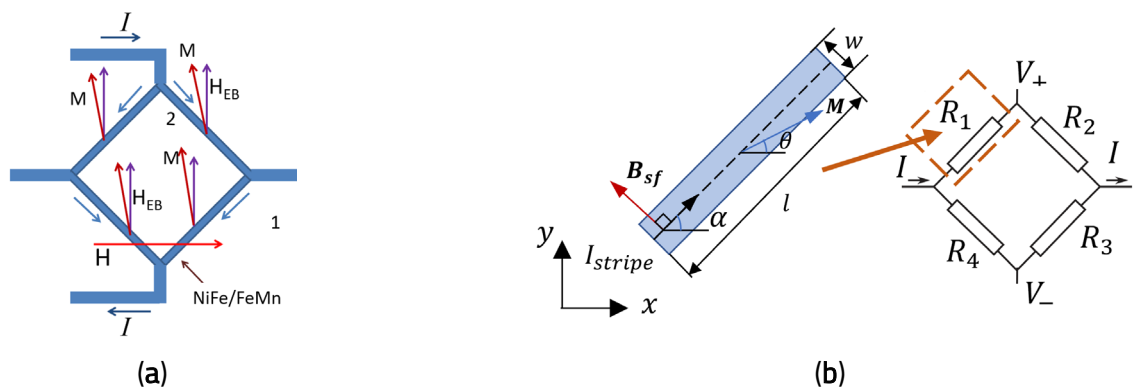


Figure 6.1. Working principle of the AMR bridge sensor: (a) AMR element stripe configuration; (b) Equivalent circuit of a single AMR bridge sensor and magnetic field parameters through a stripe.

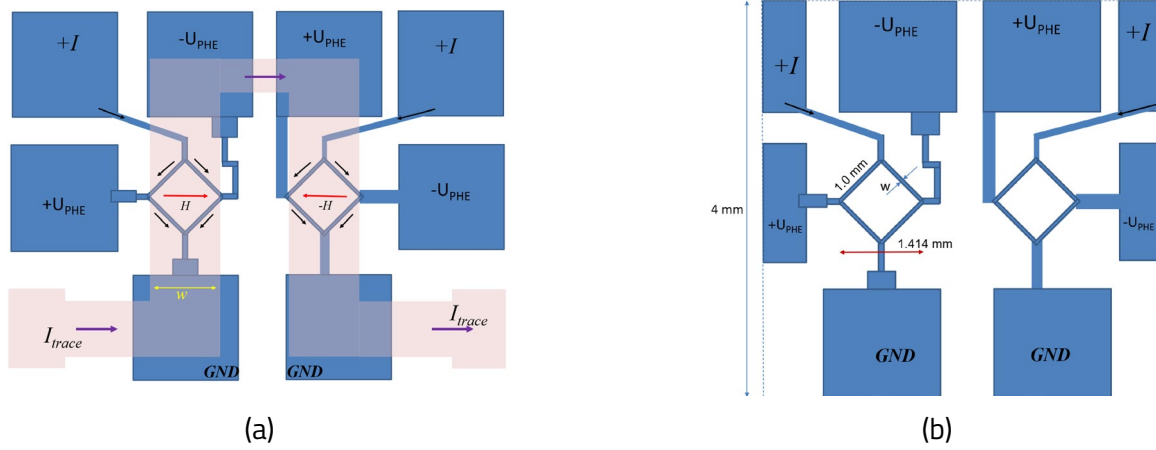


Figure 6.2. Layout of the exchange biased AMR bridge sensor chip: (a) Chip layout with over imposed U-shaped current trace on top of the AMR bridges; (b) Dimensions of the chip.

Based on the equivalent circuit for one AMR bridge sensor (Figure 6.2), it can be noted that the four AMR chip elements are in a Wheatstone bridge configuration (arms of the bridge  $R_1$ – $R_4$ ). Each resistor arm of the bridge can be constituted from multiple stripes for specific configurations. Thus, the resistance of each arm is dependent on the number of stripes. If there is a positive applied current through the resistor, the output voltage (potential increase in the  $y$ -direction) from the bridge is:

$$V = I \frac{R_2 R_4 - R_1 R_3}{R_1 + R_2 + R_3 + R_4} \quad (6.1)$$

where the result of the expression is valid when  $R_1 + R_2 \approx R_3 + R_4$ , thus when  $I_{stripe} = I/2$ .

### 6.1.2. Fabrication of AMR bridge Sensor Demonstrator

The proposed AMR bridge sensors use spintronic structures of the type  $Ni_{80}Fe_{20}$ (10 nm)/FeMn (1 nm) and were deposited at ICPE-CA Bucharest through magnetron sputtering on an oxidized silicon substrate and microfabricated through the liftoff method. Given the particularities of the deposition method, the structures are amorphous and have a very low electrical conductivity. Additionally, the deposited structures do not show an established magnetocrystalline anisotropy axis or an exchange bias field,  $H_{ex}$ , between the antiferromagnetic layer (FeMn) and the permalloy ( $Ni_{80}Fe_{20}$ ) magnetic layer. Finally,  $5 \times 5 \text{ mm}^2$  chips were cut. A single mask was used for the chip, thus reducing complexity of the microfabrication process significantly. A scanning electron microscope image of the chip can be seen in Figure 6.6a. Several chips were thermally treated, Figure 6.6b, with the purpose of enhancing the crystalline structures of the deposited layers and thus the electric conductivity.

The thermal treatment, made in an argon (Ar, 99.99%) atmosphere, 2 mbar pressure at a temperature of 450 °C for two hours was applied in a proposed magnetic annealing setup [36].

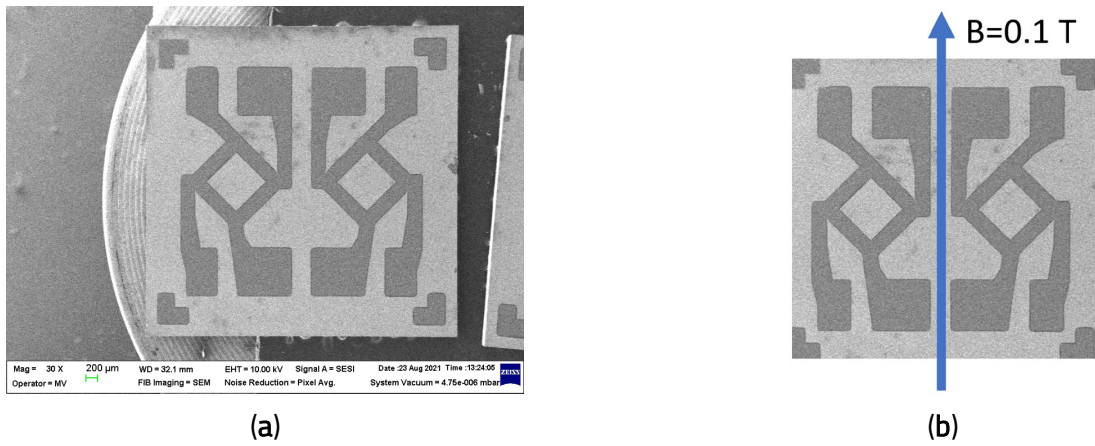


Figure 6.6. (a) SEM image of the AMR bridge sensor; (b) Direction and value of magnetic induction of the applied field,  $B$  over the structure during the magnetic annealing process.

### 6.1.3. Characterization of the AMR Bridge Sensor

#### a. Experimental Setup

The functional block diagram of the setup (Figure 6.9) was designed for increasing the performance of the AMR sensor to detect low magnetic fields, under 1 Oe ( $10^{-4}$  T in air).

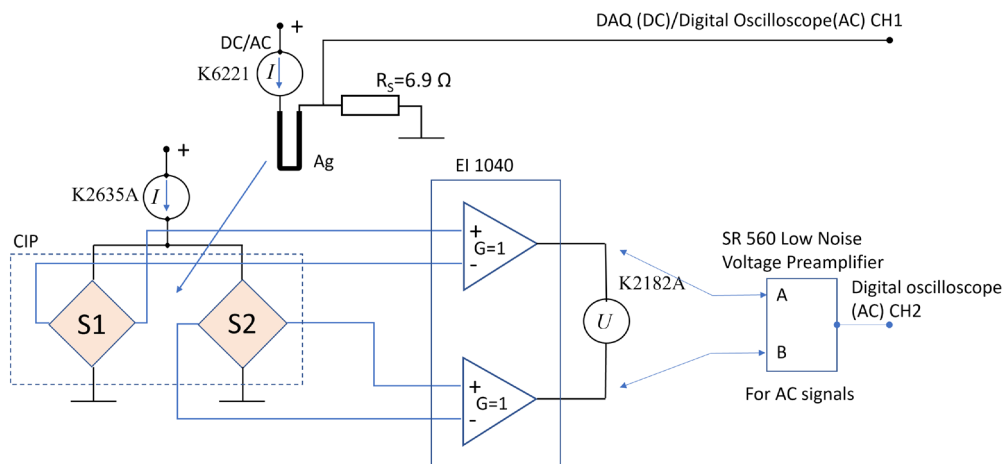


Figure 6.9. Functional block diagram of the experimental setup for the AMR bridge sensor demonstrator chip.

The chip was contacted with silver plated Cu wires. The wire-bonding was done with Ag paste from Sigma-Aldrich with a 24 h curing time at room temperature. The contacted chip was placed on a connecting PCB board, S08, MSOP8 which allows placement in a DIP PIN 8 socket with gold plated pins, Figure 6.11a. Over the chip, the printed U-shaped trace was placed. Thus, a compact structure was obtained, which can be considered a hybrid integrated circuit that can be manipulated and characterized to allow great versatility.

A second U-shaped trace was placed beneath the sensor to show the setup implementation for higher currents testing. Since the response of the sensor for low field values is of interest, a small size Helmholtz coil system was placed next to the chip, Figure 6.11b.

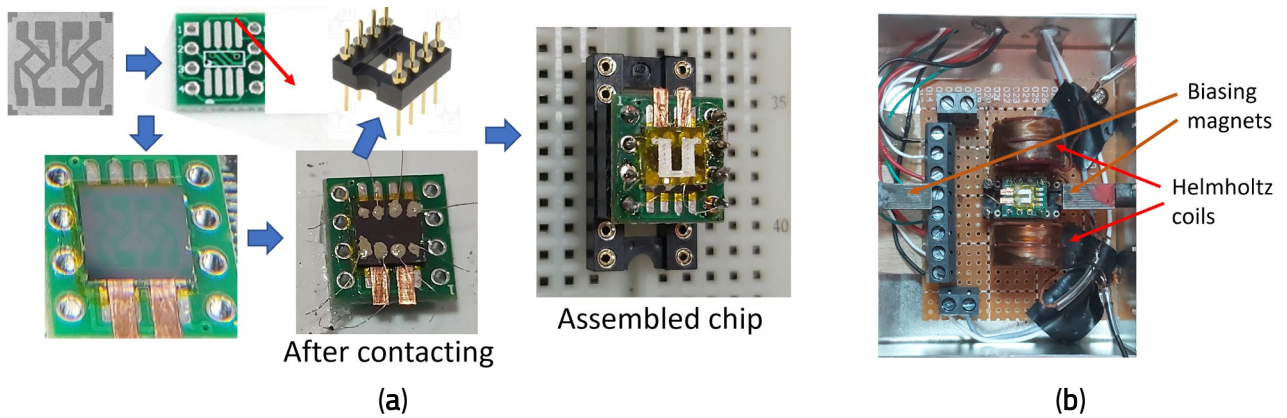


Figure 6.11. Demonstrator setup: (a) Steps for assembling the demonstrator chip; (b) The sensor mounted in the shielded box, as implemented for characterization and testing.

The entire setup is placed in a ferromagnetic enclosure for magnetic shielding. The chip was introduced in a DIP PIN 16 socket where necessary connections were made to the connection grid while remaining pins was used to connect the current traces. An additional two ferrite permanent magnets were used to compensate the effect of the exchange bias field,  $H_{bias}$ , Figure 6.11b.

### b. Characterization of the Demonstrator Chip—After Thermal and Magnetic Annealing

The field characteristics for a chip with only thermal treatment applied and for a chip that went through the magnetic annealing process are shown in Figure 6.12.

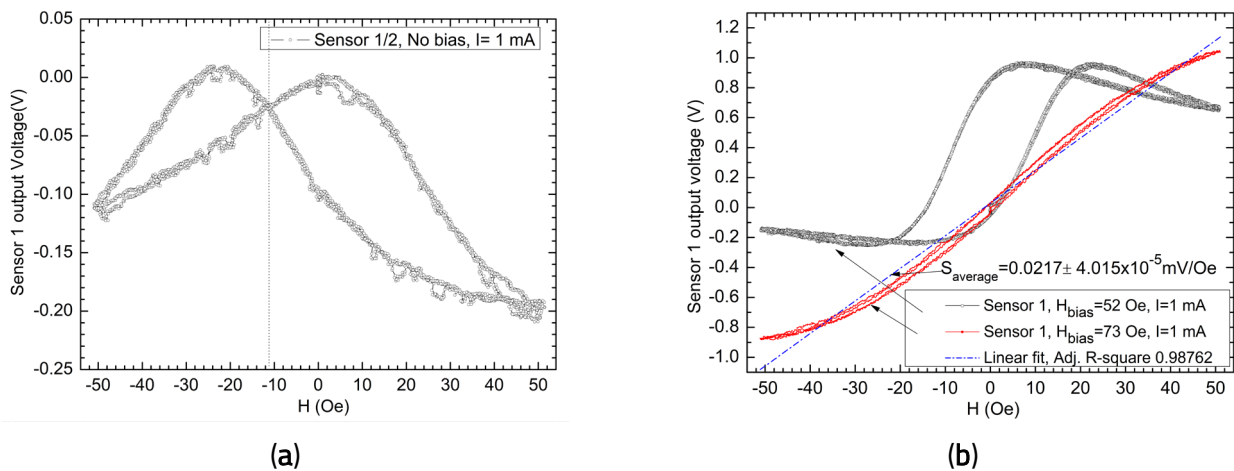


Figure 6.12. Thermally annealed AMR bridge sensor, field characteristics: (a) No applied biasing field; (b) Field characteristics for different  $H_{bias}$  values.

For the chip with both the thermal treatment and magnetic annealing, the results can be seen in Figure 6.12b for sensor "1", and Figure 6.13b for sensor "2".

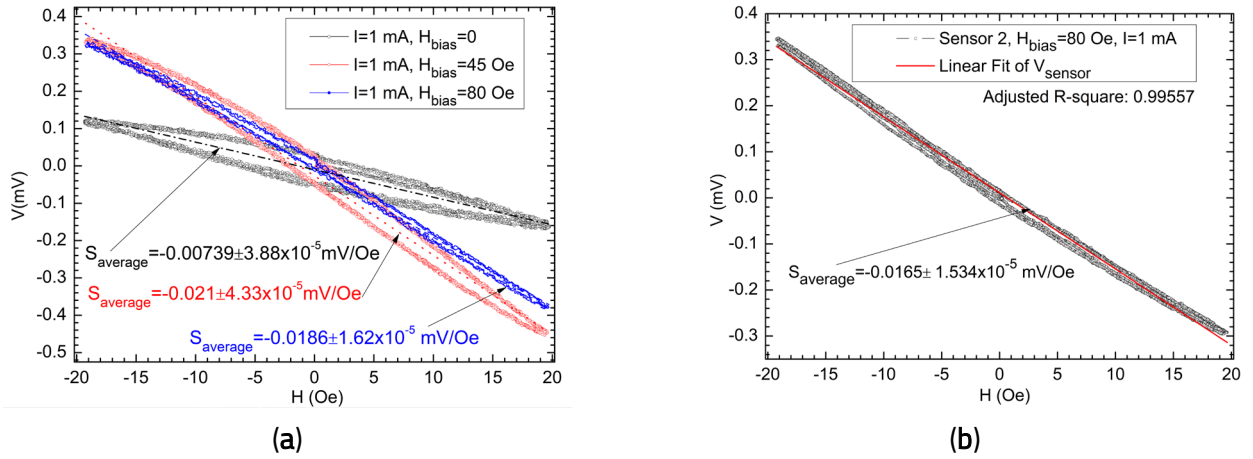


Figure 6.13. Thermally and magnetically cured AMR bridge sensor, field characteristics at different biasing levels ( $H_{bias} = 0, 45, 80$  Oe): (a) Field characteristics for sensor "1"; (b) Field characteristics for sensor "2"  $H_{bias} = 80$  Oe bias level.

In order to reduce hysteretic behavior and nonlinearity, two permanent magnets were placed on the wall of the metallic shielded box. Note that the two sensors have a 1 mm gap between them. The light asymmetries between the response of the sensors will be compensated in the differential measurement system. By taking into account the distribution of the current through the U-shaped band and the magnetic field orientation created by the sensors, the output voltage will be of type:

$$V_{diff} = V_{sensor1} - V_{sensor2}.$$

#### 6.2.4. Experimental Results for the Current Measurement Demonstrator Chip

Given that the two sensors (Figure 6.9) have very similar resistances, the option to supply the sensors with a constant current source was chosen. The K2635A current source was set to 6 mA. The current was evenly distributed between the two sensors as confirmed by the offset voltages measured for each sensor, which are very close to those when the sensors were separately supplied at 3 mA. In the conditions described above, the following data is established:

- The voltage at the terminals of the bridge: 4.399 V;
- The total resistance of the bridge: 0.734 k $\Omega$ ;
- The power dissipated by the bridge: 13.1 mW.

The response characteristic of the AMR sensor in differential mode as a function of current flowing through the printed Ag band is depicted in Figure 6.15. A good linearity of the system with a sensitivity between  $4-4.67 \cdot 10^{-4}$  mV/mA was obtained.

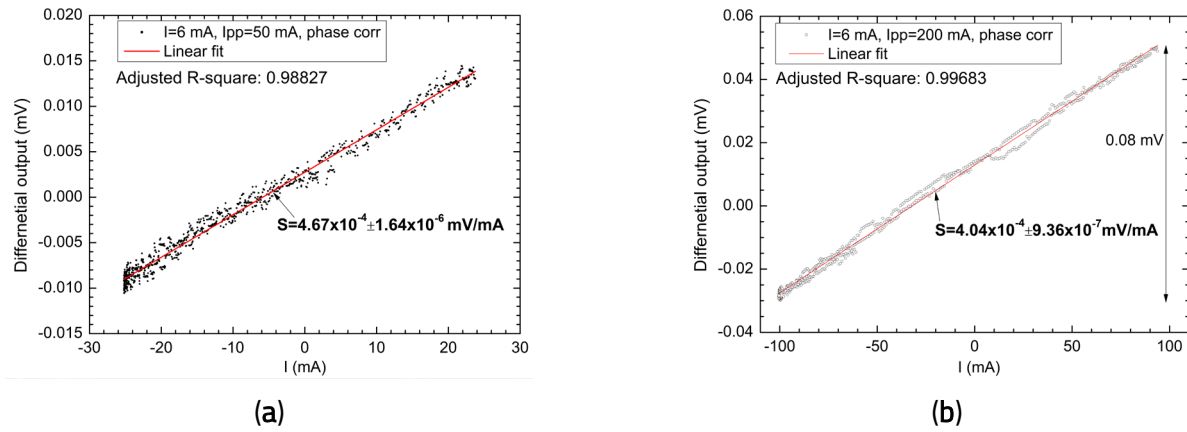


Figure 6.15. Response characteristics of the differential sensor, depending on the value of the current through the printed Ag trace for: (a) Low currents up to 25 mA; (b) Currents up to 100 mA.

The detection limit of the setup is around 2 mA (both DC and AC). The linearity error was determined from Figure 6.15b by determining a 0.006 mV error for a signal variation of 0.078 mV, which constitutes around a 7.5% linearity error. The sensor was tested between a range of 0–100 mA to avoid any significant thermal effects on the conductive band which can influence the signal stability. The setup aims to serve as a proof of concept and cannot be compared directly with commercial solutions but is now subject to new developments, especially concerning the multilayer structure used to deposit the sensors.

More complex structures based on the GMR or TMR effect, with cross-axis anisotropy, can lead to much improved results and significantly increased performance of this kind of sensor. The results of this work may also be used to detect magnetic nanoparticles instead of U-shaped stripes on PHR sensor branches. They may be viewed as extra sources of the magnetic field that could cause the bridge to become unbalanced. Subsequent research endeavours may concentrate on intricate sensor configurations.

## 6.2. Development of a Single Trace GMR Based Device for Non-Contacting DC/AC Current Measurement

### 6.2.1. Characterization of the GMR-based Current Sensor

In this study, a practical method that will significantly increase the sensitivity and accuracy of a GMR sensor by proper design of the circuit that produces the magnetic field is presented. The work in this subchapter is part of the published authored work [20]. The novelty of this setup consists in a double differential measurement setup with adjustable permanent magnet biasing field. The current  $I$  from the conducting traces generates a magnetic field, whose component  $B_x$  will be detected by the GMR sensor.

The AA003-02 sensor [95], which contains two active GMR elements and two shielded ones, connected in a Wheatstone bridge, has a GMR ratio between 13%–16% [95]. Figure 6.21 presents the output characteristics obtained when the sensor is unbiased.

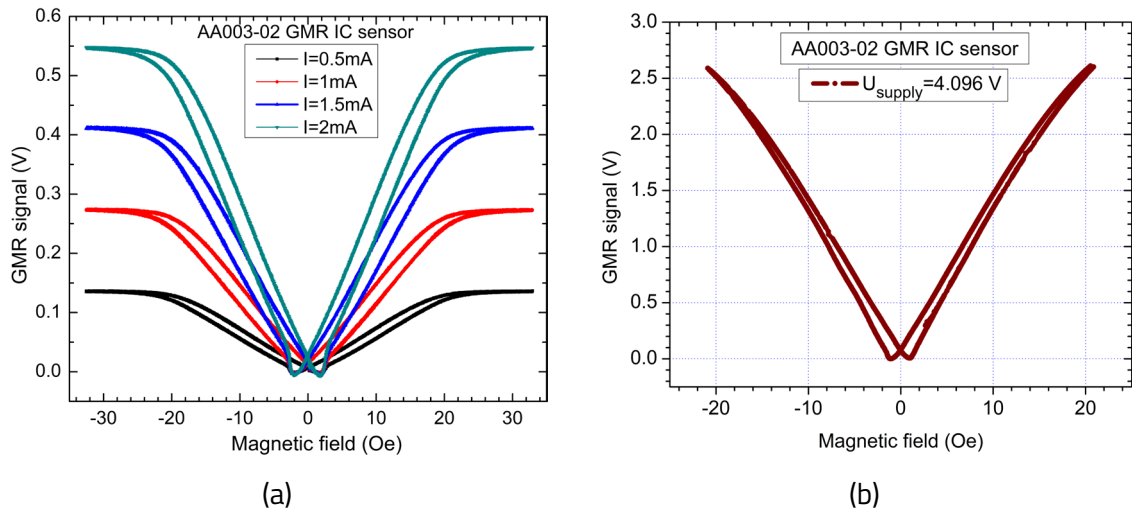


Figure 6.21. Typical measured field dependencies of the output signal for AA003-02 GMR sensor for: (a) different driving currents; (b) supplied with 4.096 V.

### 6.2.2 Design, Construction and Characterization of the Single Trace GMR-based Device

Figure 6.25 shows the PCB of the customized current measurement system. The current  $I$  passes through the U-shaped conductive band (Figure 6.25a) and GMR sensors are arranged to function in a differential arrangement, meaning that the output voltage increases for one sensor and lowers for the other.

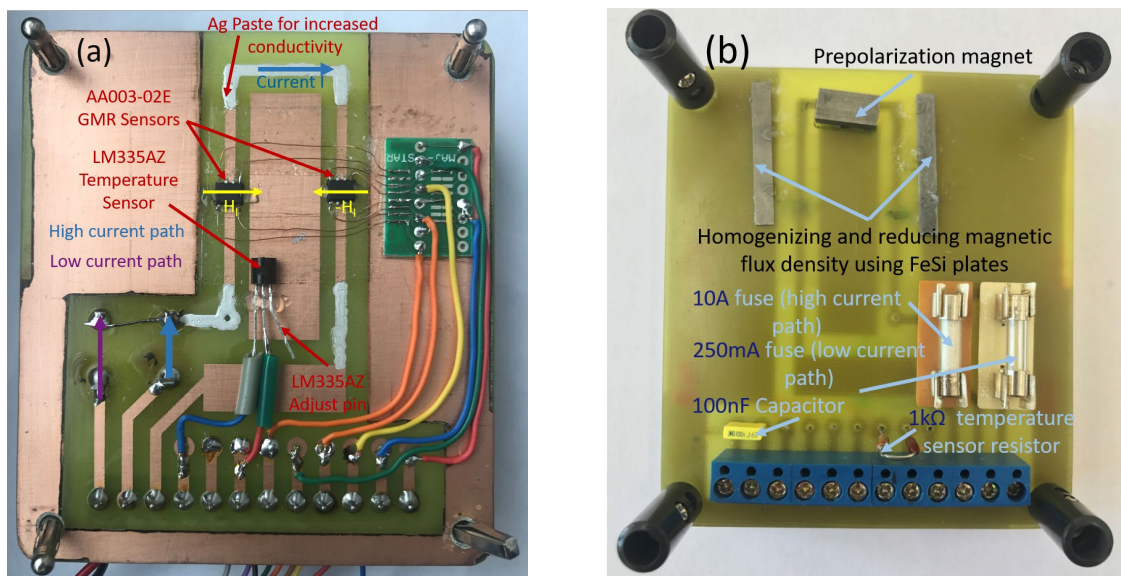


Figure 6.25. Custom PCB for current measurement using GMR sensors: (a) backside; (b) frontside. The Ag paste is used to increase the cross section (and consequently, electrical conductivity) in the contacting areas, thus reducing the overall electrical resistance of the “U” shaped current trace.

A moveable permanent magnet and two FeSi plates comprise an adjustable biasing system that reduces and homogenizes the effective magnetic flux density (Figure 6.25b). Regarding design decisions, 8 Oe was selected for the biasing field. The mode of operation is as follows: the GMR

sensor passes to a linear operation regime when the permanent magnet creates a magnetic field directed toward the sensitive axis of the sensors.

The conductive band has a width of 4 mm. This configuration simultaneously cancels off undesired external interference magnetic fields. Because there is galvanic isolation between the sensors and the current trace, this method of operation prevents the sensor from being impacted by overcurrent. Because of the manufacturing technology, where an AF (antiferromagnetic) layer or a synthetic AF layer is used to bias the pinned layer, even if the current produces a fairly large magnetic field, this will not affect the sensor's functionality. In other words, the magnetization of the pinned layer is unaffected, and the magnetization of the free layer will return to its initial orientation. This implies that, unlike many AMR sensors, there is no requirement for an external magnetic field to reset the sensors.

The functional block diagram of the current measurement differential system using GMR sensors is shown in Figure 6.26. The output signals from the sensors are amplified in this instance using a LabJack EI1040 Dual Instrumentation amplifier [244], with a gain of 10 adjusted for each channel. An additional LabJack EI1040 amplifier, with a gain of 10 for low current measurements and 1 for high current measurements, amplifies the resultant signal further.

The AA003-02 GMR sensors were supplied with a 4.096 V constant voltage, generated by a thermally compensated source, from the EI 1040 Dual Instrumentation amplifier. For this voltage, the current through each sensor was about 0.8 mA (the internal resistance for each sensor is 5 k $\Omega$ ).

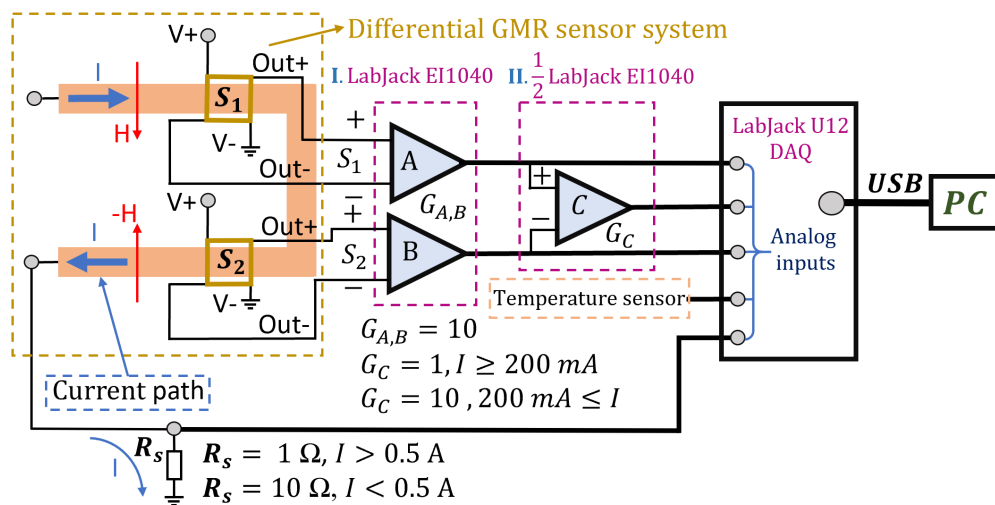
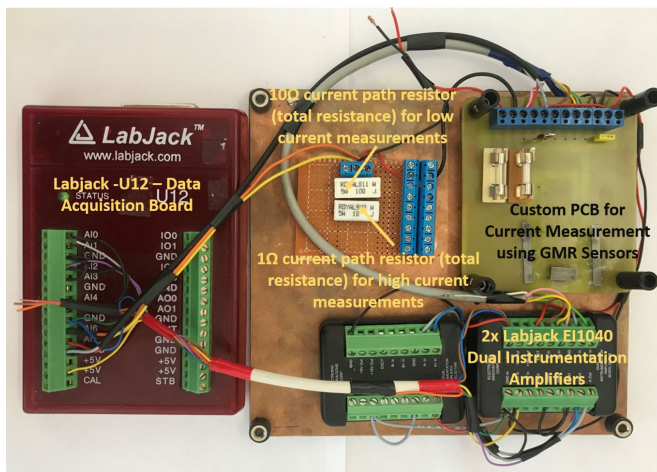


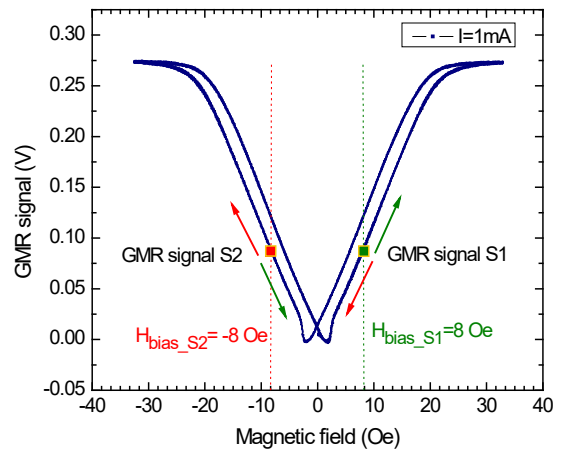
Figure 6.26. Functional block diagram of current measurement differential system using GMR sensors.

The use of two almost identical AA003-02E sensors led to a double differential measurement system, which further increased the advantages and precision above a single differential measurement arrangement.

The differential current measuring system's operation is shown in Figure 6.27. Both of the sensors had a biasing field of 8 Oe applied through the permanent magnet. For  $H_{bias} = -8 \text{ Oe}$ , the voltage on sensor S1 decreases whereas the voltage on sensor S2 increases when the same current  $I$  is applied.



(a)



(b)

Figure 6.27. Differential measurement system: (a) experimental setup; (b) mode of operation illustration for  $H_{bias} = 8$  Oe: when a current  $I$  is applied through the U-shaped band, the voltage on sensor 1 increases (green arrow) whereas the voltage on sensor 2 decreases (red arrow).

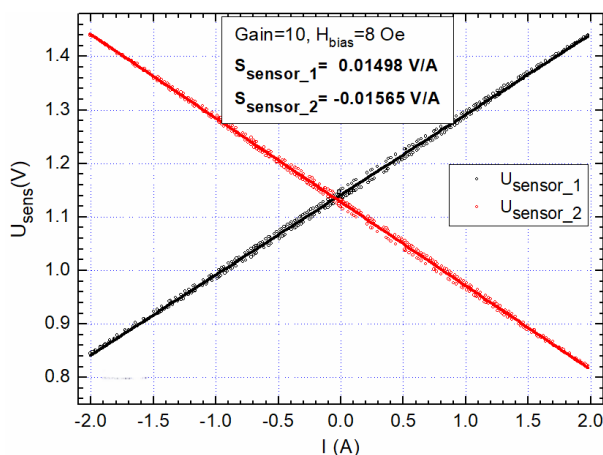
By considering that  $S_1 \approx S_2$  (for the same type of sensors), i.e., the system is thermally balanced, and the differences between the sensors output variation created by external fields are negligible, the output signal will be:

$$\Delta U = (K_{S1} + K_{S2}) \cdot H_I = (K_{S1} + K_{S2}) \cdot C \cdot I = S \cdot I \quad (6.8)$$

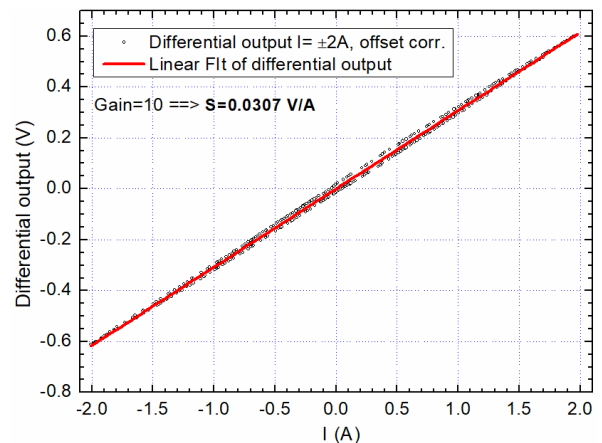
where  $S$  (V/A) is the sensitivity of the differential measurement system.

### Direct Current Measurements

With 8 Oe biased sensors, the output will be linearized for both sensors. Figure 6.29 shows the system's output when a varied DC current between -2 A and 2 A is measured.  $S = 0.0307$  V/A is the differential output sensitivity.



(a)



(b)

Figure 6.29. Differential output of sensors polarized at 8 Oe, DC  $\pm 2$  A: (a) individual sensors response; (b) differential output.

### 6.3. Development of a Multi-Trace GMR Based Device for Non-Contacting DC/AC Current Measurement

This work, published in [184], includes designing and implementing an ultra-sensitive GMR current sensor that can detect DC and AC currents from 2 to 300 mA, with a setup sensitivity ranging from 15.62 to 23.19 mV/mA. Between 10 Hz and 50 kHz, the detection limit is 100  $\mu$ A in DC and 100 to 300  $\mu$ A in AC. The basic approach for these improvements is to use a multi-turn planar coil and a double differential GMR based detection system, along with a mixed DC/AC biasing system utilizing both permanent magnets and a Helmholtz coil setup.

#### 6.3.1. Multi-Trace GMR Based Device Development and Mode of Operation

For this setup, two AA003-02E sensors were used in differential configuration [95]. A GMR-based current measuring setup was created using the analytical method's results. Figure 6.37 shows the PCB setup. The current trace setup is the same as the one described in Section 4.2.1, Table 4.1.

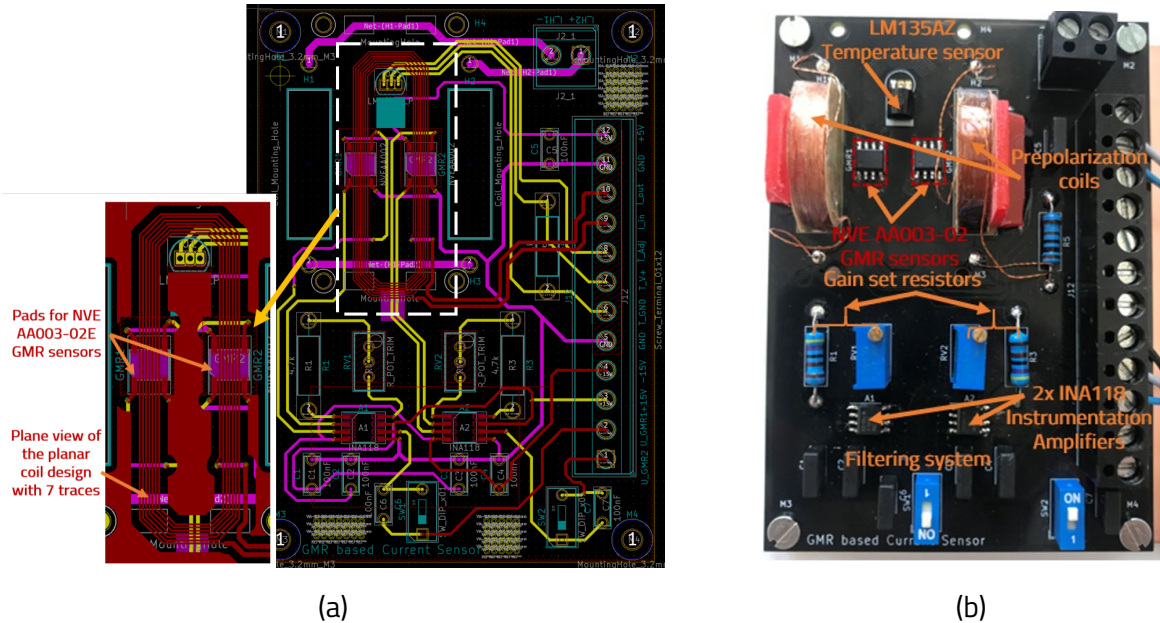


Figure 6.37. GMR Testboard (custom PCB) optimized for low field detection (current measurement) using GMR sensors: (a) PCB layout and detail; (b) experimental board.

#### 6.3.2. Experimental Results for Non-Contacting DC/AC Current Measurement

##### a. DC Experimental Results

The results focus on demonstrating the low currents sensing capabilities of the proposed setup (Figure 6.40). For all results, the real sensor sensitivity is shown (with no amplification). The main challenge is low currents measurements, since higher currents can be easily detected with the setup, for example by integrating a copper bar in the PCB backside.

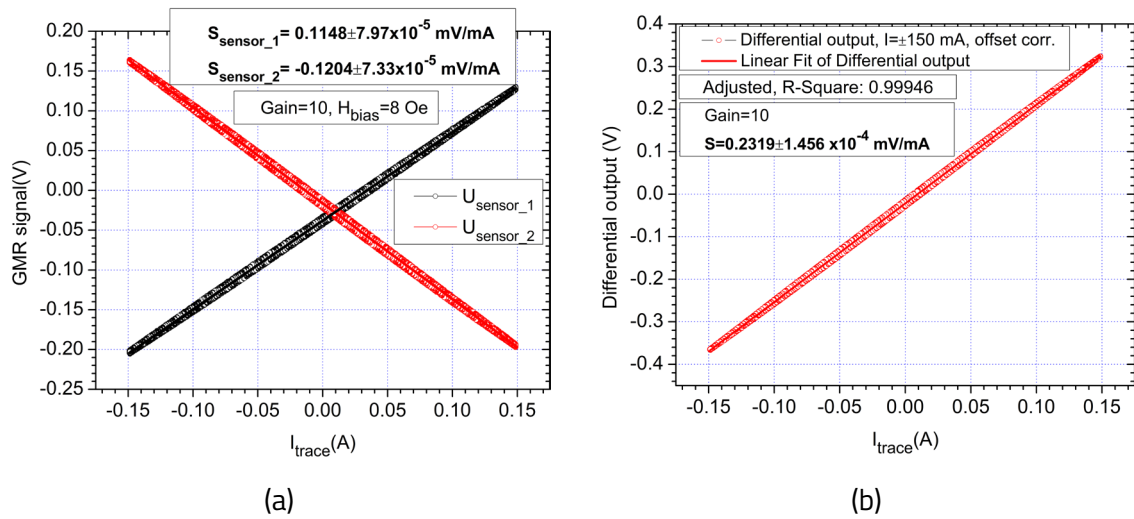


Figure 6.40. Response of the system for a  $\pm 150$  mA, DC current,  $H_{bias}$  was set to 8 Oe: (a) individual sensors response; (b) differential output.

The sensitivities obtained (Figure 6.40) are higher than the results presented in [20], for the NVE AG003-01E sensor evaluation kit (which utilizes the same model of sensors), measured on a single trace with a similar width 0.254 mm (the obtained sensitivity is  $S_{measured} = 0.0179$  mV/mA), while for the differential system in [10] with a trace thickness of 4 mm, for the same 150 mA test, the obtained sensitivity ( $S_{D=4\text{ mm}} = 0.028$  mV/mA) is approximately 8.3 times lower. In this structure, an improvement in sensitivity of about 13 times over the sensor evaluation kit and 8.3 times over the previously optimized differential configuration [20] was attained using the multi-trace arrangement.

### b. Low Current Capabilities

It is possible to accurately detect lower current values because of the notable improvements in sensor sensitivity.

Figure 6.46 shows the AC calibration curve for the device within the 0–100 mA range when measuring a 100 Hz sinewave. We used the adjusted  $R$ -squared term to show how well data is aligned over the fitting line. The adjusted  $R$ -square is 0.99992. The sensitivity of the entire setup  $S$ , in the 0-100 mA range is 15.62 mV/mA. Note that there is a very good correlation between the measured current and the response of the system.

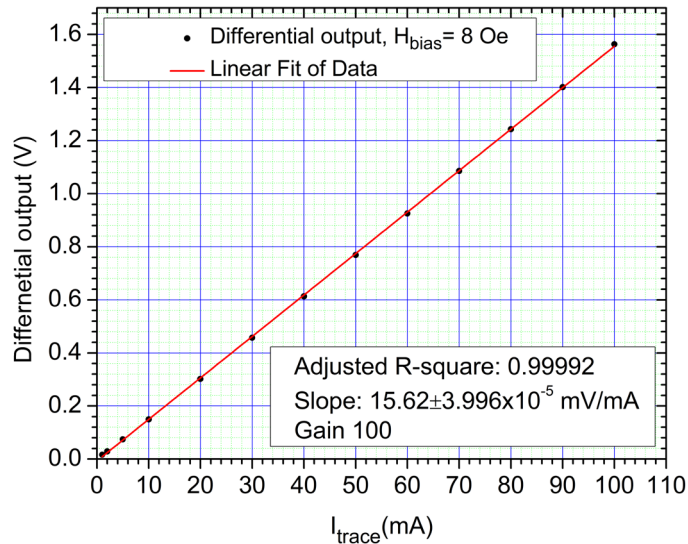


Figure 6.46. AC calibration curve in the 0–100 mA range for a 100 Hz sinewave. The minimum trace current represented on the calibration curve is 1 mA.

## 6.5. Conclusions

### a. AMR Bridge Device

1. The research is dedicated to the design, construction and characterization of a demonstrator based on an AMR bridge sensor for non-contacting current measurement. This includes two identical AMR sensors connected in a bridge configuration, which can be used individually or in differential setup to minimize the impact of temperature variation and magnetic field interferences. The physical dimension of the chip and current trace is established, and the functionality of the demonstrator chip is verified through simulations.
2. The AMR bridge chip, with a  $\text{Ni}_{80}\text{Fe}_{20}$ (10 nm)/FeMn structure was microfabricated at ICPE-CA Bucharest. The current trace and magnetic annealing of the sensors was performed at the Transilvania University of Brasov, research centre of the Electrical Engineering and Applied Physics Department – The Applied Physics research laboratory.
3. Experimental determinations were performed for both AMR sensors and then in differential setup. For this, the author builds an experimental setup that includes the demonstrator chip, measurement current source and sensor supply current, magnetic field sources (Helmholtz coils and permanent magnets), electronic amplifier blocks and measurement systems (currents, voltages, magnetic field etc.).
4. The performed analysis certifies the possibility of measuring with AMR bridge sensors in differential configuration or currents of the order 0-100 mA. AC tests at a frequency and with varying current amplitudes (5 mA, 25 mA, 50 mA) indicate linear output (around 7.5% linearity error) and stability of the measurements with no perceived disturbances. The detection limit was  $\pm 2$  mA both in DC and AC.

### **b. Single Trace GMR based Device**

1. The research involved the implementation of a high sensitivity non-contacting current measurement experimental setup based on giant magnetoresistance (GMR) sensors. In order to enhance and exploit the sensitivity of the GMR sensors, the author proposes utilizing the GMR sensors in a double differential connection setup with an adjustable biasing system.
2. The current measurement setup was based on a PCB made by the author, which contains the two GMR sensors, U-shaped current trace temperature sensor and permanent magnetic biasing system. The biasing system is made by a rectangular ferrite magnet with the possibility of rotation and two FeSi sheets to concentrate the magnetic flux around the sensor area for the desired biasing field.
3. A Giant magnetoresistance (GMR) sensor-based high sensitivity non-contacting current measuring experimental setup was put into practice. The detector setup's sensitivity ranges from 0.0272 to 0.0307 mV/mA, and its hysteretic effects are minimal (40 mA). The field dependences of the sensors were linearized by means of a biasing magnetic field. Furthermore, the differential GMR system that has been put into place is versatile, since it can measure both DC and AC currents. It was demonstrated that the current measuring device could measure in both DC (75 mA to about 4 A) and AC (150 mA to 4 A) with high accuracy and long duration.
4. These results were obtained without EMF shielding or filtering systems. The custom PCB for the system was designed to measure currents up to 10 A (by considering the copper trace width). On the other hand, it has been noted that prolonged measurement of currents greater than 4 A results in appreciable heating.

### **c. Multi-Trace GMR based Device**

1. This research includes improvements performed by the author for the non-contacting current measurement system with GMR sensors, consisting in: utilizing multiple current traces in a planar coil configuration, double differential measurement method, a mixt DC/AC biasing system which utilizes permanent magnets and a special configuration of the Helmholtz coil.
2. The measurement setup has higher performance compared to the one that utilizes a single current measurement trace.
3. A specially designed PCB with GMR sensors served as the foundation for an extremely sensitive non-contacting current measuring system that was suited for low field applications. Two commercial GMR sensors are utilized (AA003-02E) in a double differential configuration. A spiral planar coil ensures, through the 7 rectilinear traces, a concentration of the magnetic field which is measured by the sensors. The dimensioning and validation of the current trace structure is shown in Chapter 4 (Table 4.1, Figures 4.13-4.16). The biasing magnetic field, for linearizing the GMR sensors response is made up of two biasing coils placed in a symmetrical quasi-Helmholtz configuration on the PCB with an optimal distance from each GMR sensor. The calibration of the coils is realized through measurements in the PCB assembly stage ( $R_{coil} = 38 \Omega$ , for  $I = 57.55 \text{ mA}$ ,  $H_{bias} = 8 \text{ Oe}$ ).

4. The experimental determination performed by the author served to demonstrate the capability of the method and the performance of implemented setup for non-contacting low currents measurement in DC and AC operation.

Compared with the sensitivity values from specialty literature, this data certifies the improvement of the measurement performance by the proposed differential setup with GMR sensors with a planar coil with 7 current traces:

1. The developed measurement system allows DC and AC currents detection between 2 and 300 mA with a high sensitivity between 15.62 to 23.19 mV/mA. The setup has a detection limit of 100  $\mu$ A in DC and for frequencies between 10 Hz and 50 kHz, a 100 to 300  $\mu$ A detection limit. Higher frequency determinations were limited by the limitations of the processing electronics since the sensors function with frequencies up to 1 MHz.
2. For periodic signal of different waveforms, the measurements certified the integrity of the measured signals: the voltage output waveform ( $V_{out}$ ) closely follows waveform of the measured current.

The experimental setup presented in Subchapter 6.3 has greatly improved the operational range of the sensor for low current values compared with the study in Subchapter 6.2 and commercial solutions. This approach was not seen in other works [112, 152, 153, 158], or in commercial sensor solutions based on AMR [13,19], Hall [250], microfluxgate [145, 146] or TMR [147].

## **7. Final Conclusions, Original Contributions, Valorisation of Research Results and New Research Directions**

### **7.1. Final Conclusions**

This doctoral research has as task to identify and to development the appropriate solutions for optimizing magnetoresistive sensors performance for two specific applications: magnetic nanoparticles detection, and non-contacting current measurement. The activities developed and the results obtained are described in a structured manner for each specific objective of thesis.

*01. Development of a knowledge base through documentation and comparative analysis of the magnetoresistive effects to be applied in the design and conceptualization of magnetic field sensor applications.*

This research objective was taken into account in all developed activities, but the main results are described in Chapter 2 of the thesis: *Magnetoresistive Effects in the Microfabrication of Magnetic Sensors*. The knowledge regarding the magnetoresistive effects which serve as the basis microfabrication of magnetoresistive sensors is systematized.

*02. Modeling, simulations and experimental validation for the processes that take place in magnetoresistive sensors and electrical current measurement structures.*

This research objective was accomplished through the activities described in Chapter 3 and Chapter 4 of the thesis.

#### **a. Micromagnetic Simulations of Magnetoresistive Sensors Behavior**

The micromagnetic theory is an essential tool for determining the behavior of magnetoresistive sensors structures. Micromagnetic simulation can be a fast and efficient way to validate a particular design, but results should always be validated through experimental determinations since not all microscopic phenomena that affect magnetic thin films are considered by the micromagnetic theory.

- The micromagnetic approach is useful in the design process of sensors, for the precise determination of geometric parameters and their shape and the choice of material. But, beside the advantages of micromagnetic method as well as the inaccuracies that may occur, the experimental research is necessary to validate the results. The experimental research is introduced to validate the simulation results.
- Simulations performed utilizing SimulMag, LLG Micromagnetics, and Object Oriented Micromagnetic Framework (OOMMF) software highlight the behavior of sensors based on AMR, PHE and GMR effects for magnetic field measurement.
- The simulated GMR spin valve structure allows to obtain the magnetic field characteristics under the presence and absence of magnetic nanoparticles on the surface of the sensor. Presence of

magnetic nanoparticles on the surface of the spin valve GMR sensor influences the magnetization in sense that there is an increased resemblance of the magnetization to that of a single magnetic nanoparticle as MNPs concentration increases.

The study performed demonstrates that modeling and simulations with micromagnetic theory are an essential step in the design and optimization process and for evaluating the field performance of prospective magnetoresistive sensors structures. However, due to the inherent challenges of electromagnetic disturbances that can disturb sensor performance for specific applications, especially in the low field region, macroscopic evaluation of the electromagnetic field sources around the sensor area may be necessary. This can be achieved either by experimental or analytical investigations to improve sensor geometric selectivity of magnetic field sources or by intentional functional setup improvements for specific applications.

### **b. Macroscopic Analytical Methods and Electromagnetic Simulations for Different Conductor Types**

Due to the inherent challenges of electromagnetic disturbances that can disturb sensor performance for specific applications, especially in the low magnetic field domain, the macroscopic evaluation of the electromagnetic field sources around the sensor area are required. The analytical models and macroscopic electromagnetic simulations are advantageous tools for optimizing and improving the geometric selectivity of magnetoresistive sensors. These findings can be applied especially for non-contacting current measurement applications, in which current trace shape, length and design of measurement structure can radically affect the magnetic field in the sensor area. By utilizing electromagnetic theory, several specific analytical models and simulation are developed to estimate with a very good degree of accuracy the magnetic field intensity generated in the magnetoresistive sensor area.

- The models for single, rectangular, and toroidal conductors in which DC current flows have been developed and the magnetic field intensity in different point are calculated, for establish a best approach for implementing a conductor type for a non-contacting magnetoresistive current sensor.
- The model for coil type conductors provides good field uniformity and intensity for a given current, but, for miniaturized applications it is difficult to be implement regular coils
- The model for rectilinear single and multiple traces is developed and the expression of magnetic field intensity in different points created by current flowing through the traces is obtained. For the U-shape trace and planar coil the study performed considers different parameters for trace material and geometries of traces. The analytical method included four study cases: neglecting the thickness of the trace, dividing the thickness of the trace in several layers, finite or very long conductive trace, and several adjacent traces in the sensor area.
- The comparison with experimental study shows that the case of the analytical model when the trace is finite in length and the thickness of the trace is considered and divided in an appropriate number of layers is the most accurate. However, for longer trace lengths, models which neglect the length of the trace can prove more accurate and are closer to the COMSOL FEM model.

- The analytical method was validated using finite elements method COMSOL simulation and experimental results.

These results are useful for designing and optimizing applications that contain current traces such as non-contacting current sensors and for magnetic nanoparticles detection as some measurement methods involve polarizing the magnetic nanoparticles with a biasing field that can be produced either by a coil or a current trace.

### **03. *Development of methods and experimental setups for magnetic nanoparticles detection with magnetoresistive sensors.***

This research objective was accomplished mainly through the activities described in Chapter 5 of the thesis.

#### **b. Experimental Setup**

The focus of this study is to conceive two experimental setups and several methods for improving the performance and characteristics of GMR sensors systems for MNPs detection.

- The first method relies on analysis of the derivative of the output signal of the sensor to determine the presence and concentration of MNPs. It was estimated that the experimental system determined a magnetic moment of about  $9.098 \cdot 10^{-5}$  emu for a signal fluctuation of 0.035 V (i.e., a detection sensitivity of approximately 75.81 emu/g).
- The second method involves a custom-built printed circuit board to optimize geometric selectivity and overall efficiency of the detection setup. Through the second method, DC testing and AC magnetorelaxometry experiments were performed for detecting MNPs.

The research in this field demonstrated the possibility of the MNPs detection by using the magnetoresistive sensors systems. Several approaches were analysed for optimizing the setup for MNPs detection.

The obtained method and results can be further improved and applied to develop very sensitive and integrated magnetoresistive biosensor setups, with an end goal for Lab-on-a-chip implementation of highly specialized biological measurements which will significantly reduce analysis costs and improve accessibility of personalized healthcare.

### **04. *Development of non-contacting current measurement devices based on magnetoresistive sensors.***

This research objective was accomplished mainly through the activities described in Chapter 6 of the thesis.

The main author contributions are designing and construction of magnetoresistive sensors based on AMR, GMR and TMR effects. The experimental setups designed and realized, and the results of the experimental determinations performed for the characterization of the sensors and measuring devices and for their validation in the non-contact measurements of electric currents and magnetic field detection are described.

### **a. AMR Bridge Device**

The design, construct and characterize a demonstrator based on AMR bridge sensor for non-contacting current measurement is proposed. This includes two identical AMR sensors connected in a bridge configuration, which can be used individually or in differential setup in order to minimize the impact of temperature variation and magnetic field interferences. The physical dimension of the chip and current trace is established, and the functionality of the demonstrator chip is verified through simulations.

The AMR bridge chip, with a  $\text{Ni}_{80}\text{Fe}_{20}$ (10 nm)/FeMn structure was microfabricated at ICPE-CA Bucharest. The current trace and magnetic annealing of the sensors was performed at the research centre of the Electrical Engineering and Applied Physics Department – The applied physics research laboratory.

Experimental determinations were performed for both AMR sensors and then in differential setup. For this, the author constructed an experimental setup that includes the demonstrator chip, measurement current source and sensor supply current, magnetic field sources (Helmholtz coils and permanent magnets), electronic amplifier blocks and measurement systems (currents, voltages, magnetic field etc.).

The sensor characteristics are performed after signal stabilization and magnetic annealing, in the presence and absence of the measured current which passes through the U-shaped trace of the demonstrator. The performed analysis certifies the possibility of measuring with AMR bridge sensors in differential configuration or currents, in DC and AC, assuring the linearity and stability of the measurements. The detection limit was  $\pm 2$  mA both in DC and AC.

Results can be significantly improved by utilizing more complex structures based on the GMR or TMR effect, with cross-axis anisotropy, which can lead to significantly enhanced performance of this type of sensor.

### **b. Single Trace GMR based Device**

The design and implementation of a high sensitivity non-contacting current measurement experimental setup based on GMR sensors are realized. In order to enhance and exploit the sensitivity of the GMR sensors, the author proposes utilizing the GMR sensors in a double differential connection setup with an adjustable biasing system.

A Giant magnetoresistance (GMR) sensor-based high sensitivity non-contacting current measuring experimental setup was put into practice. The detector setup's sensitivity ranges from 0.0272 to 0.0307 V/A, and its hysteretic effects are minimal (40 mA). The field dependences of the sensors were linearized by means of a biasing magnetic field. Furthermore, the differential GMR system that has been put into place is incredibly flexible, since it can measure both DC and AC currents. It was demonstrated that the current measuring device could measure in both DC (75 mA to about 4 A) and AC (150 mA to 4 A) with high accuracy and long duration. These results were obtained without EMF shielding or filtering systems. The custom PCB for the system was designed to measure currents up to 10 A (by taking into account the copper trace width). On the other hand, it has been noted that prolonged measurement of currents greater than 4 A results in appreciable heating.

### **c. Multi-Trace GMR based Device**

A specially designed PCB with GMR sensors is proposed for an extremely sensitive non-contacting current measuring system that was suited for low field applications. Two commercial GMR sensors are utilized (AA003-02E) in a double differential configuration. A spiral planar coil, ensures, through the 7 rectilinear traces, a concentration of the magnetic field which is measured by the sensors. The biasing magnetic field, for linearizing the GMR sensors response is made up of two biasing coils placed in a symmetrical quasi-Helmholtz configuration on the PCB with an optimal distance from each GMR sensor. The calibration of the coils is realized through measurements in the PCB assembly stage. The other parts of the measurement system are described: preamplifier, amplifier, data acquisition system, measurement and calibration devices.

The experimental determination performed by the author served as purpose to demonstrate the capability of the method and proposed setup for non-contacting low currents measurement in DC and AC. The experimental setup has greatly improved the operational range of the sensor for low current values.

### **d. Tunnelling Magnetoresistive Probe**

A research activity was performed for developing an adjustable current probe designed for non-contacting current measurement on printed circuit boards with utilizing TMR sensors. TMR sensors are adequate for these types of applications, allowing setup flexibility, high sensitivity and low current measurement.

Experimental determinations included measurements in AC at the frequency of 1 kHz, and the following values of the sensitivities are obtained:  $S_{\pm 0.4A} = 0.3231 \text{ mV/mA}$  and  $S_{\pm 0.02A} = 0.1696 \text{ mV/mA}$  were obtained.

The current TMR probe configuration, although offers very good sensitivity, shows nonlinearity effects especially at low field values. The results are very promising to serve as basis for an automatic non-contacting current probing application or for 2D/3D magnetic mapping applications.

## **7.2. Original Contributions**

Based on extensive literature critical analysis, the elements which constitute original contributions to the PhD thesis are in the field of knowledge systematization and critical review, modeling and simulations methods, procedures and measurement techniques, and new device conception.

### **A. Knowledge systematization and critical review**

1. Systematizing knowledge regarding the theoretical background of magnetoresistive effects (AMR, GMR, TMR).
2. Critical review of magnetoresistive sensor technologies, performance and material implementation.

3. Systematic review of electromagnetic theory for calculating the magnetic field for different conductor types.
4. Systematic review regarding magnetoresistive biosensors and the use of magnetic nanoparticle (MNPs) in magnetic immunoassay and magnetophoresis.

### **B. Modeling and simulations methods**

1. Micromagnetic simulations of planar Hall sensors with different geometries and for simulating reversed nucleation caused by magnetic nanoparticles local effects.
2. Micromagnetic simulations of GMR spin-valve sensors with and without MNPs on the sensor surface.
3. Model and procedure for determining the magnetic field intensity produced by current flowing in a single or multiple parallel rectilinear current traces.
4. Comparative electromagnetic simulation study between single and planar coil current trace configurations.
5. Comparative electromagnetic simulation study between different trace geometries: magnetic field dependency on trace shape, width, length.

### **C. Procedures and measurement techniques**

1. Experimental study utilizing the vibrating sample magnetometer method for evaluating the properties of functionalized maghemite nanoparticles.
2. Optimization of the method of applying perpendicular magnetic fields and analyzing the derivative of the output signal for improving the performance of GMR sensors for magnetic nanoparticles detection.
3. Optimization of the method of applying magnetorelaxometry for detecting magnetic nanoparticles using GMR sensors.

### **D. New device conception**

1. Developing a GMR-based MNPs detection setup with optimized geometric selectivity, reduced sized and integrated microfluidics. The focus of the setup was placed on the specific challenges of integrating microfluidic with highly miniaturized MR sensors designs. The setup demonstrated both MNPs DC detection and AC magnetorelaxometry capabilities.
2. Design, development, microfabrication and experimental validation of an AMR bridge sensor and associated setup with integrated current traces for increased low current performance. The sensor setup used a single mask method during fabrication.
3. Design, development and experimental validation of a GMR-based non-contacting current measurement setup based on a single U-shaped trace design and adjustable permanent magnet biasing.
4. Design, development and experimental validation of a tunnelling magnetoresistive probe for non-contacting current measurement on printed circuit boards.

### 7.3. Valorisation of Research Results

Research results were valued by publishing scientific articles in ISI journals, BDI journals, and volumes of some national and international conferences, together with communications held during Doctoral School and several National funded research projects where the author was involved as a project member. The innovative results by the author are confirmed by publication of a patent request and a high number of citations for the published articles.

#### A. Papers published in ISI rated journals

1. **Muşuroi C.**, Oproiu M., Volmer M., Firastrau, I. (2020). High Sensitivity Differential Giant Magnetoresistance (GMR) Based Sensor for Non-Contacting DC/AC Current Measurement. *Sensors*, 20(1), 323. <https://doi.org/10.3390/s20010323>.  
WOS:000510493100323  
IF: 3.576/3.735 (2020/5 year), AIS: 1.254 (2020)
2. Oproiu M., **Muşuroi C.**, Volmer M., "Low cost and integrable healthcare services using VoIP for remote patient monitoring", 2020 International Conference on e-Health and Bioengineering (EHB). <https://doi.org/10.1109/EHB50910.2020.9280206>  
WOS:000646194100078
3. **Muşuroi C.**, Oproiu, M., Volmer, M., Neamtu, J., Avram, M., Helerea, E. (2021). Low Field Optimization of a Non-Contacting High-Sensitivity GMR-Based DC/AC Current Sensor. *Sensors*, 21(7), 2564. <https://doi.org/10.3390/s21072564>-  
WOS:00063885500000  
IF: 3.847/4.050 (2021/5 year), AIS: 1.309 (2021)
4. **Muşuroi, C.**, Volmer, M., Oproiu, M., Neamtu, J., & Helerea, E. (2022). Designing a Spintronic Based Magnetoresistive Bridge Sensor for Current Measurement and Low Field Sensing. *Electronics*, 11(23), 3888. <https://doi.org/10.3390/electronics11233888>  
WOS:000897337500001  
IF: 2.9/2.9 (2022/5 year), AIS: 0.758 (2022)
5. Helerea, E., Calin, M. D., & **Musuroi, C.** (2023). Water Energy Nexus and Energy Transition—A Review. *Energies*, 16(4), 1879. <https://doi.org/10.3390/en16041879>  
WOS:000944949200001  
IF: 3/3 (2023/5 year), AIS: 0.576 (2023)
6. Bakhtiaridoost, S., **Musuroi, C.**, Volmer, M., & Florescu, M. (2024). Optoelectronic microfluidic device for point-of-care blood plasma viscosity measurement. *Lab on a Chip*. <https://doi.org/10.1039/d4lc00211c>  
WOS:001245052700001  
IF: 6.1/6.82 (2023/5 year), AIS: 2.868 (2023)

Cumulated Impact Factor (IF): 19.423/20.505 (publication year/5 years); Cumulated Article Influence Score (AIS): 6.765

## B. Papers published in BDI journals

1. **Mușuroi C. L.**, & Volmer M. (2018). OOMMF Modelling of Magnetization Dynamics in Micrometer Sized Structures for Sensing Applications. Bulletin of the Transilvania University of Brasov. Series I: Engineering Sciences, 47-54.
2. **Mușuroi C.**, Volmer M., Oproiu M. "*Optimizing a Non-Contacting High-Sensitivity GMR-based Current Sensor Design for Low Field Applications.*" In Sensors and Electronic Instrumentation Advances, Proceedings of 6th International Conference on Sensors Engineering and Electronics Instrumentation Advances (SEIA' 2020), pag. 127-131, ISBN: 978-84-09-23483-7, oral presentation, Edited by Sergey Y. Yurish.
3. Volmer M., Avram M., Oproiu M., **Mușuroi C.**, Firastrau I., Bezerghceanu A., "*Planar Hall Effect Sensors for Low Field Detection and Lab on a Chip Applications*", in Sensors and Electronic Instrumentation Advances, Proceedings of 6th International Conference on Sensors Engineering and Electronics Instrumentation Advances (SEIA' 2020), pag. 132-137, ISBN: 978-84-09-23483-7, Edited by Sergey Y. Yurish.
4. Oproiu M., Neagu A., Cotfas P. A., Cotfas D. T., **Mușuroi C.**, Volmer M. (2021). "*LoRa Wide-Area Network and Live Objects Used in Renewable Energy Monitoring.*" In 2021 International Aegean Conference on Electrical Machines and Power Electronics (ACEMP) & 2021 International Conference on Optimization of Electrical and Electronic Equipment (OPTIM) (pp. 505-512). IEEE. <https://doi.org/10.1109/OPTIM-ACEMP50812.2021.9590023>
5. Volmer M., **Mușuroi C.**, Oproiu M., Avram A., Avram, M., Helerea, E. (2021). "*On Detection of Magnetic Nanoparticles Using a Commercial GMR Sensor*". In 2021 International Aegean Conference on Electrical Machines and Power Electronics (ACEMP) & 2021 International Conference on Optimization of Electrical and Electronic Equipment (OPTIM) (pp. 1-6). IEEE. <https://doi.org/10.1109/OPTIM-ACEMP50812.2021.9590055>
6. Rekeraho, A., Balan, T., Cotfas, D. T., Cotfas, P. A., Acheampong, R., & **Musuroi, C.** (2022, November). "*Sandbox Integrated Gateway for the Discovery of Cybersecurity Vulnerabilities*". In 2022 International Symposium on Electronics and Telecommunications (ISETC) (pp. 1-4). IEEE.
7. Helerea, E., Călin M. D., & **Mușuroi, C.** (2023). Identificarea și vizualizarea tendințelor emergente în cercetarea științifică folosind metode bibliometrice. Buletinul AGIR, 28(1).

## C. Patent request

1. EN:  
Marius Volmer, Melinda David, Monica Florescu, Adrian Bezerghceanu, **Cristian Mușuroi**, **Method for controlling magnetic anisotropy in soft magnetic thin films**, Romania, application number A/00305, 10.06.2024.

RO:

Marius Volmer, Melinda David, Monica Florescu, Adrian Bezerghceanu, **Cristian Muşuroi**,  
**Procedeu pentru controlul anizotropiei magnetice în straturi subțiri feromagnetice moi**,  
 cod depunere A/00305 din 10.06.2024.

#### D. Research projects (member)

Table 7.1. Contributing research projects (author served as a member) during the Ph.D thesis period.

No.	Project	Role	Implementation Period
1	Complex consortium projects CDI (PCCDI) - „Microfluidic platform for the detection of circulating tumor cells (CTC) concentrated by dielectrophoresis-magnetophoresis and analyzed by dielectric and electrochemical impedance spectroscopy - uCellDetect”, code CNCSIS ID_3PCCDI/2018, Project director: Prof. Dr. Ing. Marius Andrei Olariu, Transilvania University of Brasov coordinator: Conf. Dr. Phys. Marius Volmer	Research assistant Transilvania Univ. of Brasov	01-03-2018 – 31-12-2020
2	PED - „Advanced spin-valve sensors for precise non-contact measurements of DC/AC currents DC/AC (SpinCurrentSense)”, code CNCSIS ID_PN-III-P2-2.1-PED-2019-1804, 315PED/2020, Director proiect: Dr. Phys. Jenica NEAMTU, Transilvania University of Brasov coordinator: Conf. Dr. Phys. Marius Volmer.	Research assistant Transilvania Univ. of Brasov	03-08-2020 – 29-07-2022
3	PED - Magnetoresistive Sensors Optimized for On-Chip Magnetic Nanoparticles Detection - MagSensOnChip”, cod CNCSIS ID_PN-III-P2-2.1-PED-2019-3514, 510PED/2020, Project Director: Conf. Dr. Phys. Marius Volmer	Research assistant Transilvania Univ. of Brasov	23-10-2020 – 21-10-2022
4	PED – Graphene based spintronic structures for sensing applications and signal processing - GrapheneS”, code CNCSIS ID_PN-III-P2-2.1-PED-2021-3112, 597PED/2022, Project director: Conf. Dr. Phys. Marius Volmer	Research assistant Transilvania Univ. of Brasov	21-07-2022 – 21-6-2024

#### E. National and International Conference Communications

1. Firastrau, I., Volmer, M., **Musuroi, C.**, “*Micromagnetic study on reversal nucleation of magnetization induced by magnetic nanoparticles.*” Joint European Magnetic Symposia, JEMS 2019, August 26-30 2019, Uppsala, Sweden.

2. **Muşuroi C**, Volmer M., Oproiu M, "*Optimizing a Non-Contacting High-Sensitivity GMR-based Current Sensor Design for Low Field Applications*", in Sensors and Electronic Instrumentation Advances, Proceedings of 6th International Conference on Sensors Engineering and Electronics Instrumentation Advances (SEIA' 2020),, pag. 127-131, ISBN: 978-84-09-23483-7, Edited by Sergey Y. Yurish.
3. Volmer M., Avram M, Oproiu M, **Muşuroi C.L.**, Firastrau I., Bezergheanu A., "*Planar Hall Effect Sensors for Low Field Detection and Lab on a Chip Applications*", in Sensors and Electronic Instrumentation Advances, Proceedings of 6th International Conference on Sensors Engineering and Electronics Instrumentation Advances (SEIA' 2020), pag. 132-137, ISBN: 978-84-09-23483-7, Edited by Sergey Y. Yurish.
4. **Muşuroi C**, Helerea E., Volmer M., "*A Review on using Magnetoresistive Biosensors for Magnetic Nanoparticles Detection*", 17th MIKLÓS IVÁNYI INTERNATIONAL PHD & DLA SYMPOSIUM, UNIVERSITY OF PÉCS, Hungary, Section Information Technology 3, article code P-123, 25 Oct. 2020. Program: <https://phdsymp.mik.pte.hu/program>
5. Volmer M., Bezergheanu A., Prejbeanu L., **Muşuroi C.** and Oproiu M, *Exchange biased structures used for magnetic nanoparticles detection*, TIM 20-21 Physics Conference, November 11th - 13th 2021, Timisoara, Romania, Section Applied Physics and Interdisciplinarity (API), Invited (API-103), Friday 12th of November 2021, Final Program, Page 6, [https://timconference.uvt.ro/API\\_submissions.php](https://timconference.uvt.ro/API_submissions.php)
6. Bezergheanu A., Cizmaş C.B., Volmer M., Oproiu M., **Muşuroi C.**, "*Magnetic and electric properties of printable perovskite type structures of  $(La_{1-x}Pr_x)_2/3Ba_{1/3}MnO_3$  manganites*", 12th International Conference on Materials Science and Engineering – BraMat 2022, Braşov, România, 9-12 Martie 2022, <https://www.bramat.ro/program.html>, [https://www.bramat.ro/uploads/7/7/4/0/77408170/1\\_program\\_bramat2022.pdf](https://www.bramat.ro/uploads/7/7/4/0/77408170/1_program_bramat2022.pdf)
7. **Muşuroi C.**, Volmer M., Helerea E., "*Electromagnetic Field Modelling of Conductive Traces for a High-Precision Non-contacting GMR Current Sensor*", , European Magnetic Sensors and Actuators Conference (EMSA) 5-8 Iulie 2022, Madrid, Spain. Program: <https://www.emsa2022.com/index.php/programa/scientific-program>  
Abstract book: <https://www.emsa2022.com/images/site/Abstracts-Book-EMSA-2022.pdf>, pag. 31.
8. Volmer M., Oproiu M., **Muşuroi C.**, "*Micromagnetic Simulations and Experimental Results on Magnetic Nanoparticles Detection with Exchange Biased Structures*", , European Magnetic Sensors and Actuators Conference (EMSA) 5-8 Iulie 2022, Madrid, Spania.  
Program: <https://www.emsa2022.com/index.php/programa/scientific-program>  
Abstract book: <https://www.emsa2022.com/images/site/Abstracts-Book-EMSA-2022.pdf>, page 80.

9. **Muşuroi C.**, Volmer M., Helerea E., Oproiu M, *An analytical approach for magnetoresistive sensor performance on magnetic nanoparticles detection for biosensing systems*", 6th edition of International Conference on Analytical and Nanoanalytical Methods for Biomedical and Environmental Sciences 8-10 Iunie 2022, Brasov, Romania.  
Program: <https://icanmbes2020.sciforum.net/#custom1150>  
Abstract book: [https://icanmbes.unitbv.ro/abstracts\\_book.html](https://icanmbes.unitbv.ro/abstracts_book.html), pag. 65, P2.5.
10. Volmer M, , David M., Avram M., Florescu M., Bezerghceanu A., **Muşuroi C.**, Oproiu M., " *Using Magnetic Nanofibers to Control the Magnetic Anisotropy of a Thin Permalloy Film*", 13th Joint European Magnetic Symposia (JEMS 2023), Madrid, Spania, 27 August – 1 September 2023. Book of Abstracts, Page 337: [https://www.jems2023.es/images/site/JEMS2023-BOOK\\_OF\\_ABSTRACTS.pdf](https://www.jems2023.es/images/site/JEMS2023-BOOK_OF_ABSTRACTS.pdf)

#### 7.4. New Research Directions

The subject of each approached research in the frame of doctoral thesis constitutes the basis of new research directions and further development. Thus, the following research directions are taken into account:

- Developing new analytical models for describing the magnetic field in the sensor area for more complex geometries.
- Research regarding extending the usability of micromagnetic theory for simulating more exotic magnetic sensor designs, such as graphene-based sensors.
- Introducing hybrid simulation setups for magnetic nanoparticles MNPs detection in solution which will evaluate the sensor response according to the volume or surface concentration of MNPs.
- Development of magnetoresistive biosensors fully integrated in Lab-on-a-chip applications.
- Development of flexible magnetoresistive sensors for various applications. With proper device reliability, reproducibility and sensitivity, low-cost Lab-on-a-chip biosensors can be implemented for point-of-care testing applications.
- Development of highly integrated low current and high current magnetoresistive non-contacting current measurement devices and certifying reliability of the devices beyond laboratory use in industrial, automotive and precision scientific applications.
- Development of a non-contacting current sensor probe for automated testing of electronic boards.
- Development of 2D and 3D magnetic mapping systems with magnetoresistive sensors. The setups can be applied for electromagnetic field testing compliance of electronic boards or for complex magnetic field mapping of magnetic field sources.

## Bibliography (Selective)

- [1] Horizon Europe 2022-2027. Available online: [https://research-and-innovation.ec.europa.eu/funding/funding-opportunities/funding-programmes-and-open-calls/horizon-europe/cluster-4-digital-industry-and-space\\_en](https://research-and-innovation.ec.europa.eu/funding/funding-opportunities/funding-programmes-and-open-calls/horizon-europe/cluster-4-digital-industry-and-space_en)
- [2] Planul Național de Cercetare Dezvoltare Inovare 2022-2027, Available online: <https://www.mcid.gov.ro/transparenta-decizionala/planul-national-de-cercetare-dezvoltare-si-inovare-2022-2027/>.
- [3] Chen, C., & Song, M. (2019). Visualizing a field of research: A methodology of systematic scientometric reviews. *PloS one*, 14(10), e0223994.
- [4] Guide to Searching, Brown University Library. Available online: <https://libguides.brown.edu/searching/citation> (accessed on 30th June 2023).
- [5] Moher, D., Shamseer, L., Clarke, M., Ghersi, D., Liberati, A., Petticrew, M., ... & Stewart, L. A. (2015). Preferred reporting items for systematic review and meta-analysis protocols (PRISMA-P) 2015 statement. *Systematic reviews*, 4(1), 1-9.
- [6] Granell, P. N., Wang, G., Cañon Bermudez, G. S., Kosub, T., Golmar, F., Steren, L., ... & Makarov, D. (2019). Highly compliant planar Hall effect sensor with sub 200 nT sensitivity. *npj Flexible Electronics*, 3(1), 3, <https://doi.org/10.1038/s41528-018-0046-9>.
- [9] Nalwa, H. S. (Ed.). (2001). *Handbook of thin films*, Five-volume set. Academic Press. Vol. 5, Chapter Nanomaterials and Magnetic Thin Films, Academic Press, 2002, ISBN 0125129084. [2].
- [10] Weiss, R., Mattheis, R., & Reiss, G. (2013). Advanced giant magnetoresistance technology for measurement applications. *Measurement Science and Technology*, 24(8), 082001.
- [20] **Mușuroi, C.**, Oproiu, M., Volmer, M., & Firastrau, I. (2020). High sensitivity differential giant magnetoresistance (GMR) based sensor for non-contacting DC/AC current measurement. *Sensors*, 20(1), 323., <https://doi.org/10.3390/s20010323>.
- [25] Lenz, J., & Edelstein, S. (2006). Magnetic sensors and their applications. *IEEE Sensors journal*, 6(3), 631-649, <https://doi.org/10.1109/jsen.2006.874493>.
- [26] S. Tumanski, *Thin Film Magnetoresistive Sensors*. Bristol, U.K.: Inst. Phys., 2001.
- [29] Lenz, J. E. (1990). A review of magnetic sensors. *Proceedings of the IEEE*, 78(6), 973-989.
- [30] Caruso, M. J., Bratland, T., Smith, C. H., & Schneider, R. (1998). A new perspective on magnetic field sensing. *SENSORS-PETERBOROUGH-*, 15, 34-47.
- [31] Du, W. Y. (2014). *Resistive, capacitive, inductive, and magnetic sensor technologies*. CRC Press.
- [32] Thomson, W. (1857). XIX. On the electro-dynamic qualities of metals:—Effects of magnetization on the electric conductivity of nickel and of iron. *Proceedings of the Royal Society of London*, (8), 546-550.
- [33] McGuire, T., & Potter, R. L. (1975). Anisotropic magnetoresistance in ferromagnetic 3d alloys. *IEEE Transactions on magnetics*, 11(4), 1018-1038.
- [34] Damsgaard, C. D., Freitas, S. C., Freitas, P. P., & Hansen, M. F. (2008). Exchange-biased planar Hall effect sensor optimized for biosensor applications. *Journal of Applied Physics*, 103(7).
- [35] Elzwawy, A., Rasly, M., Morsy, M., Piskin, H., Volmer, M. (2024). *Magnetic Sensors: Principles, Methodologies, and Applications*. In: Ali, G.A.M., Chong, K.F., Makhlof, A.S.H. (eds) *Handbook of Nanosensors*. Springer, Cham: Springer Nature Switzerland.

- [36] **Muşuroi, C.**, Volmer, M., Oproiu, M., Neamtu, J., & Helerea, E. (2022). Designing a Spintronic Based Magnetoresistive Bridge Sensor for Current Measurement and Low Field Sensing. *Electronics*, 11(23), 3888.
- [39] Elzwawy, A., Pişkin, H., Akdoğan, N., Volmer, M., Reiss, G., Marnitz, L., ... & Schmalhorst, J. M. (2021). Current trends in planar Hall effect sensors: evolution, optimization, and applications. *Journal of Physics D: Applied Physics*, 54(35), 353002.
- [42] Samal, D., & Anil Kumar, P. S. (2008). Giant magnetoresistance: Nobel Prize in Physics 2007. *Resonance*, 13, 343-354.
- [43] Ullah, S. (2017). Optical control and detection of spin coherence in multilayer systems (Doctoral dissertation, Universidade de Sao Paulo).
- [44] Zhang, X., & Butler, W. (2016). Theory of Giant Magnetoresistance and Tunneling Magnetoresistance. *Handbook of Spintronics*, 3-69.
- [48] Reig, C., & Cubells-Beltrán, M. D. (2017). Giant (gmr) and tunnel (tmr) magnetoresistance sensors: From phenomena to applications. In *Magnetic Sensors and Devices* (pp. 35-64). CRC Press.
- [49] Gurney, R. W., & Condon, E. U. (1929). Quantum mechanics and radioactive disintegration. *Physical Review*, 33(2), 127.
- [50] Julliere, M. (1975). Tunneling between ferromagnetic films. *Physics letters A*, 54(3), 225-226.
- [51] Landauer, R. (1957). Spatial variation of currents and fields due to localized scatterers in metallic conduction. *IBM Journal of research and development*, 1(3), 223-231.
- [55] Zhang, X. G., Wang, Y., & Han, X. F. (2008). Theory of nonspecular tunneling through magnetic tunnel junctions. *Physical Review B*, 77(14), 144431.
- [56] Matsumoto, R., Fukushima, A., Nagahama, T., Suzuki, Y., Ando, K., & Yuasa, S. (2007). Oscillation of giant tunneling magnetoresistance with respect to tunneling barrier thickness in fully epitaxial Fe/MgO/Fe magnetic tunnel junctions. *Applied physics letters*, 90(25).
- [57] Fraden, J. (2016). *Handbook of Modern Sensors*. Springer International Publishing. Chapters Sensor Characteristics. (n.d.). 13–36. Book DOI: <https://doi.org/10.1007/978-3-319-19303-8>.
- [77] Díaz-Michelena, M. (2009). Small magnetic sensors for space applications. *Sensors*, 9(4), 2271-2288.
- [152] Poon, T. Y., Tse, N. C. F., & Lau, R. W. H. (2013). Extending the GMR current measurement range with a counteracting magnetic field. *Sensors*, 13(6), 8042-8059.
- [153] Li, Z., & Dixon, S. (2016). A closed-loop operation to improve GMR sensor accuracy. *IEEE Sensors Journal*, 16(15), 6003-6007.
- [155] García Vidal, E., Ramírez Muñoz, D., Ravelo Arias, S. I., Sánchez Moreno, J., Cardoso, S., Ferreira, R., & Freitas, P. (2017). Electronic energy meter based on a tunnel magnetoresistive effect (TMR) current sensor. *Materials*, 10(10), 1134.
- [163] Scheinfein, M. R., & Price, E. A. (2003). LLG User Manual v2. 50. Code of the LLG simulator can be found at <http://ligmicro.home.mindspring.com>. Availability: Software currently discontinued.
- [172] Volmer, M., Avram, M., Oproiu, M., **Muşuroi, C.**, Firastrau, I., & Bezerghceanu, A. (2020). Planar Hall Effect Sensors for Low Field Detection and Lab on a Chip Applications. *Sensors and Electronic Instrumentation Advances*, 132.

- [179] Volmer, M., & Avram, M. (2013). Signal dependence on magnetic nanoparticles position over a planar Hall effect biosensor. *Microelectronic engineering*, 108, 116-120.
- [180] Henriksen, A. D., Rizzi, G., & Hansen, M. F. (2015). Experimental comparison of ring and diamond shaped planar Hall effect bridge magnetic field sensors. *Journal of Applied Physics*, 118(10).
- [183] National Institute of Standards and Technology. OOMMF User's Guide, Version 1.0; Donahue, M.J., Porter, D.G., Eds.; Interagency Report NISTIR 6376; National Institute of Standards and Technology: Gaithersburg, MD, USA, 1999. Available online: <http://math.nist.gov/oommf/>
- [184] **Muşuroi, C.**, Oproiu, M., Volmer, M., Neamtu, J., Avram, M., & Helerea, E. (2021). Low field optimization of a non-contacting high-sensitivity GMR-based DC/AC current sensor. *Sensors*, 21(7), 2564.
- [186] Rapoport, E., Montana, D., & Beach, G. S. D. (2012). Integrated capture, transport, and magneto-mechanical resonant sensing of superparamagnetic microbeads using magnetic domain walls. *Lab on a Chip*, 12(21), 4433-4440.
- [188] M. Volmer and M. Avram, "Micromagnetic simulations on detection of magnetic labelled biomolecules using MR sensors," *Journal of Magnetism and Magnetic Materials*, vol. 321, no. 10, pp. 1683–1685, 2009.
- [189] **Muşuroi, C. L.**, & Volmer, M. (2018). OOMMF Modelling of Magnetization Dynamics in Micrometer Sized Structures for Sensing Applications. *Bulletin of the Transilvania University of Brasov. Series I-Engineering Sciences*, 47-54.
- [191] Nicolaide, A. *Electromagnetics. General Theory of the Electromagnetic Field. Classical and Relativistic Approaches*, 3rd ed.; Transilvania University Press: Braşov, Romania, 2012.
- [195] Cheng, D. Keun. (1993). *Fundamentals of engineering electromagnetics*. Reading (Mass.): Addison-Wesley.
- [196] Ling, S. J., Sanny, J., Moebis, W., Friedman, G., Druger, S. D., Kolakowska, A., ... & Wheelock, K. (2016). *University Physics Volume 2*.
- [197] Volmer, M. *Applied Physics for Engineering*, Editura Universităţii Transilvania din Braşov, 2007, ISBN 978-973-598-136-5.
- [198] Volmer, M. *Electromagnetic field theory. Lecture notes and applications*. Braşov: Editura Universităţii Transilvania, 2022, ISBN 978-606-19-1575-0.
- [199] NVE ALTxxx-10 TMR Sensors Catalogue. Available online: <https://www.nve.com/Downloads/ALTxxx-10.pdf>
- [200] COMSOL Multiphysics® v. 6.1. [www.comsol.com](http://www.comsol.com). COMSOL AB, Stockholm, Sweden.
- [201] NVE Sensors Catalogue. Available online: <https://www.nve.com/Downloads/catalog.pdf>
- [235] Volmer, M., Muşuroi, C., Oproiu, M., Avram, A., Avram, M., & Helerea, E. (2021, September). On detection of magnetic nanoparticles using a commercial GMR sensor. In *2021 International Aegean Conference on Electrical Machines and Power Electronics (ACEMP) & 2021 International Conference on Optimization of Electrical and Electronic Equipment (OPTIM)* (pp. 1-6). IEEE.
- [241] Hansen, M. F., & Rizzi, G. (2016). Exchange-biased AMR bridges for magnetic field sensing and biosensing. *IEEE Transactions on Magnetics*, 53(4), 1-11.
- [244] LabJack EI1040 Instrumentation Amplifier. Available online: <https://labjack.com/products/ei1040-dual-instrumentation-amplifier>